STUDIA UNIVERSITATIS
BABEŞ-BOLYAI

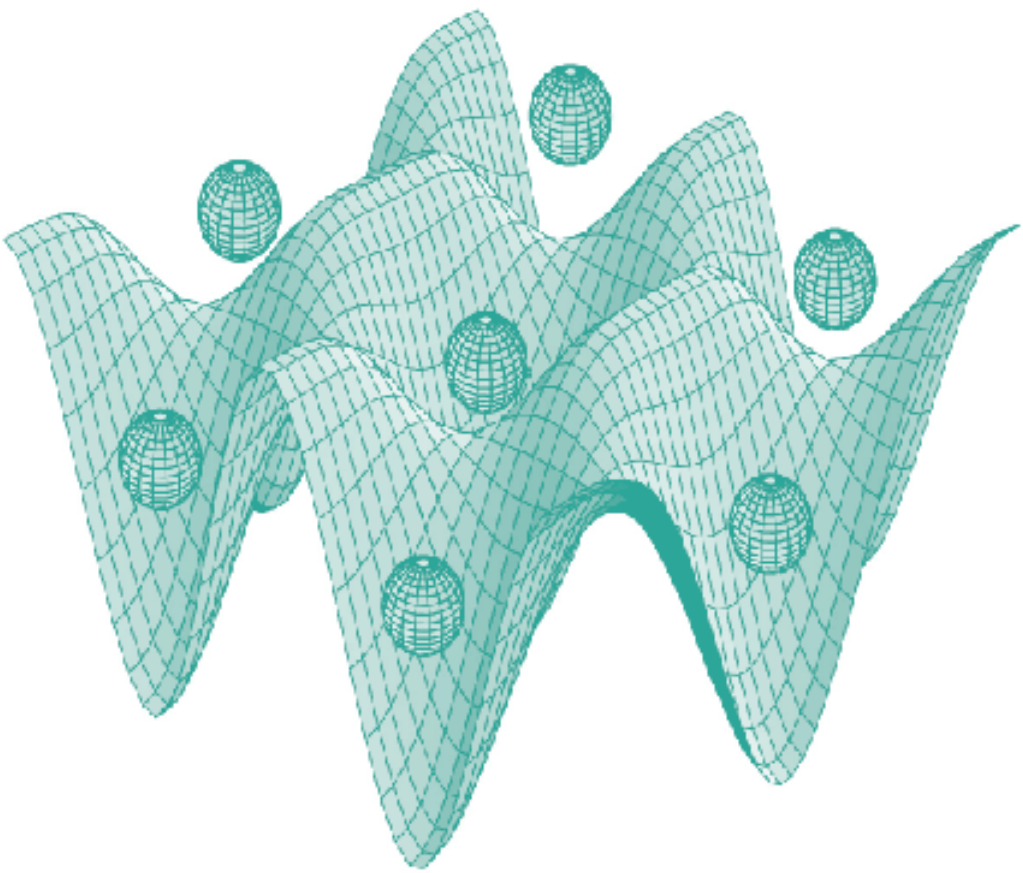

PHYSICA

1/2013

STUDIA
UNIVERSITATIS BABEŞ-BOLYAI
PHYSICA

1/2013

June

EDITORIAL OFFICE OF STUDIA UBB PYSICA:
1, M. Kogălniceanu St., Cluj-Napoca, ROMANIA, Phone: +40 264 405300
http://www.studia.ubbcluj.ro/serii/physica/index_en.html

YEAR **Volume 58 (LVIII) 2013**
MONTH **JUNE**
ISSUE **1**

S T U D I A
UNIVERSITATIS BABEŞ–BOLYAI

PHYSICA

1

Desktop Editing Office: 51st B.P. Hasdeu, Cluj-Napoca, Romania, Phone + 40 264-40.53.52

CUPRINS – CONTENT – SOMMAIRE – INHALT

STUDIA UBB PHYSICA, Vol. 58 (LVIII), 1, 2013, pp. 5-12
(RECOMMENDED CITATION)

MONITORING OF THERMAL NEUTRON FLUX OF ISOTOPIC SOURCES BY ACTIVATION METHOD

B. BIRÓ[a], L. DĂRĂBAN[a,*], V. SIMON[a]

ABSTRACT. Activation method was applied to determine the thermal and epithermal neutron fluxes delivered by ^{241}Am-^{9}Be &^{239}Pu-^{9}Be neutron double-source. Indium and gold metallic foils, as well as Sm_2O_3 and MnO_2 powders were exposed to this neutron source. In the irradiated samples^{116m}In,^{198}Au,^{56}Mn and^{153}Sm radioisotopes were activated to saturation. The data obtained from the analysis of gamma spectra recorded from the neutron activated radioisotopes were used to calculate the thermal and epithermal neutron emitted by^{241}Am-^{9}Be &^{239}Pu-^{9}Be double-source.

Keywords: *neutron flux; neutron activation; gamma-ray spectrometry.*

1. INTRODUCTION

In the last decades, the research works devoted to nuclear medicine was increasingly directed to radiotherapies by *in situ* irradiation. Boron Neutron Capture Therapy (BNCT) is a treatment method using external neutron beam[1, 2], but in last time BNCT is also considered with internal neutron irradiation, that actually combines boron neutron capture with neutron brachytherapy [3]. In order to improve thermal neutron distribution in deeper sites and to increase the therapeutic efficacy of BNCT, epithermal neutron beam was also considered [4].The BNCT principle is based on the nuclear reaction that occurs when the stable isotope ^{10}B is irradiated with low energy or thermal neutrons to yield highly energetic alpha particles and recoiling ^{7}Li ions.

A boron containing compound, usually sodiumborocaptate (BSH), or borofenilalanina (BPA), is introduced in the intended treatment. One of boron stable isotopes, ^{10}B (19.8% isotopic abundance) will produce a thermal neutron capture nuclear reaction, n_{th}(0.025 eV) + $^{10}_{5}B \rightarrow \alpha + {}^{7}_{3}Li$ + 2.79 MeV (6%) and n_{th}(0.025 eV) +

[a] Babeş-Bolyai University, Faculty of Physics, 1 Kogălniceanu Str., 400084 Cluj-Napoca, Romania
* Corresponding author: liviu.daraban@phys.ubbcluj.ro

$^{10}_{5}B \rightarrow \alpha + {}^{7}_{3}Li^{*}$ + 2.31 MeV (94%), ${}^{7}_{3}Li^{*} \rightarrow \gamma$ + 0.48 MeV, with a large cross sections σ = 3873 barns [5]. The boron neutron capture reaction (BNC) releases an average of 2.79 MeV per neutron capture. The resulting alpha particle and lithium ion carry away an average of 2.34 MeV. These heavy particles, i.e. ${}^{4}_{2}\alpha$ and ${}^{7}_{3}Li$, deposit their energy in a range of 5–9 μm which corresponds to the cell diameter and therefore, deliver nearly all their kinetic energy to the tumor cells where the boron resides [6] and leads to their destruction. BNCT is therefore a method that theoretically could make possible to kill tumour cells without affecting adjacent healthy cells, if ^{10}B atoms can be selectively accumulated in the interstitial space of tumour tissue and/or intracellular space of tumour cells [7].

Thermal neutron fluxes from ^{252}Cf sources used in brachytherapy with boron neutron capture, as reported in literature [6], were compared with the neutron fluxes determined by activation method. The metallic gold and indium foils and Sm_2O_3 and MnO_2 oxide powders we subjected to neutron activation were disposed in the irradiation block in sites considered proper for future BNCT tests on small animals.

This paper reports on methods used to determine thermal and epithermal neutron fluxes delivered by ^{241}Am-^{9}Be &^{239}Pu-^{9}Be double-source as preliminary study of further boron neutron capture studies.

2. EXPERIMENTAL

Two isotopic neutron sources (*i*) ^{241}Am-^{9}Be, with an activity of 5 Ci of ^{241}Am, with an emission of 1.1 10^7 n/s and (*ii*) ^{239}Pu-^{9}Be, with an activity of 33 Ci which emits 5.5 10^7 n/s, placed in its center of the irradiation block (Fig. 1) were used for activation of different samples containing gold, indium, manganese and samarium The two sources can be moved from the stocking position (borated paraffin block) up to the irradiation position. The paraffin block slows down the neutrons through the multiple collisions with hydrogen atoms.

The irradiation channels are placed at 3.5 cm from the central channel containing the two sources. The 3.5 cm thickness of paraffin is optimal for neutron moderation for point sources, established to test cadmium [8].

The measuring point was chosen outside the paraffin block where access was possible for several types of scintillation detectors. We tested different types of neutron detectors for B_2O_3 and ZnS (Ag), coupled to a single-channel analyzer RFT type 20026, in order to determine the most effective detector. Monitoring results are given in Table 1. The measurement time was 2 min and in each case we made 5 readings. The fraction of thermal neutrons with E_n< 0.4 eV was determined based the cadmium test (i.e., determining the difference between the total number of neutrons registered and the number of neutrons that pass through a Cd sheet of 1 mm thickness).

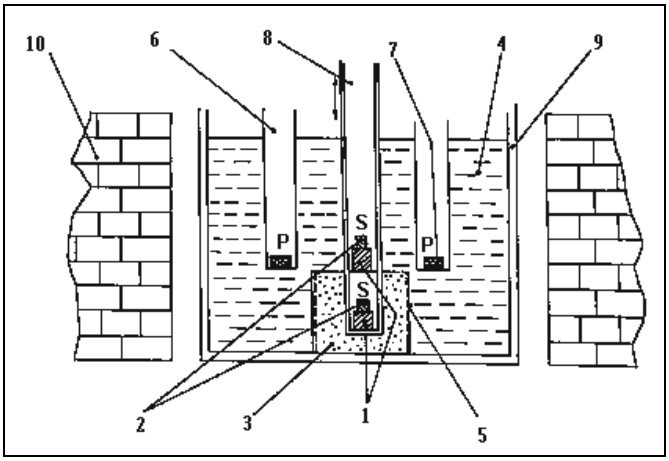

Fig. 1. The irradiation block containing the Am-Be and Pu-Be neutron sources. 1) Am-Be source, 2) Pu-Be source, 3) Borate paraffin, 4) Pure paraffin for the thermalisation, 5) Cd protection, 6) & 7) Irradiation channels, 8) Central channel for irradiation with fast neutron, 9) Fe-walls of paraffin ensemble, 10) Borated paraffine bricks for protection.

Detectors were tested in a high background level of gamma radiation emitted by a 2 μCi ^{137}Cs source. Apart from NE 451fast neutron detector, other types of detectors are not sensitive to γ radiation resulting by thermal neutrons capture from the nuclear reaction^{113}Cd (n, γ) ^{114}Cd with a σ ~ 4000 barns. The most efficient thermal neutron detector is the Tesla model SND 31/U 04/009.

Table 1. Sensitivity to thermal neutrons of various types of commercial detectors for neutrons

Crystal type	Total Counts				
	^{137}Cs source of gamma radiation	Background radiation	Total neutron	Fast neutron (Total neutron+Cd)	Thermal neutron
Tesla SND 31/ U 04/009 ZnS(Ag) +B_2O_3	251	166	47050	16857	30193
Tesla SND 31/ U 04/012 ZnS(Ag)+B_2O_3	92	43	12889	6280	6609
NE 451 Emmerich type fast neutron Plastic + ZnS(Ag)	77305	63	7441	9899	no data

Crystal type	Total Counts				
	^{137}Cs source of gamma radiation	Background radiation	Total neutron	Fast neutron (Total neutron+Cd)	Thermal neutron
Gamma /Budapest 3S/32/052 Ln-No 67012 ZnS(Ag)+B_2O_3	111	72	19344	7225	12119

The method used for neutron flux determination is based on the activation analysis, in which the absolute activity is determined by the capture reaction (n,γ) and the thermal neutron flux is calculated. The basic formula for the calculation is [9]:

$$\Lambda = \frac{N_A \cdot \sigma \cdot \theta \cdot m \cdot \Phi}{M_A} \cdot \left\{1 - e^{-\frac{t_{ir} \cdot ln2}{T_{1/2}}}\right\} \cdot e^{-\frac{t_r \cdot ln2}{T_{1/2}}} \quad (1)$$

where: Λ = the absolute activity, N_A = the Avogadro constant, σ = the cross-section, θ = the isotopic abundance, m = the mass of the sample, Φ = the neutron flux, M_A = the atomic mass, t_{ir} = the irradiation time and t_r = the cooling time.

The most productive reactions used in this study to determine the neutron flux by the activation method, are shown in Table 2. The samples were irradiated to saturation, meaning an irradiation time ≥ $5 \cdot T_{1/2}$.

Table 2. Nuclear reactions used as neutron detector

Nuclear reaction used as detector	Cross sections at thermal neutrons energy $\sigma(E_0)$ (barns)	Half- life $T_{1/2}$	E_γ (MeV)	The probabilitiy of γ-emission / desintegration
^{115}In(n,γ)^{116m}In	198 ± 3	54.12 min	0.417	0.36
^{197}Au(n,γ)^{198}Au	98.8 ± 0.3	2.696 d	0.412	0.95
^{55}Mn(n,γ)^{56}Mn	13.2 ± 0.2	2.58 h	0.847	0.99
^{152}Sm(n,γ)^{153}Sm	212 ± 12	47.1 h	0.103	0.28

The activity of the samples was determined by means of a high-resolution gamma spectrometer, equipped with a GC1519 Canbera type detector described in [10], the energy efficiency of the installation was determined according to the methodology described in the work of Lavi and Alfassi[11], by using a calibration source prepared in the laboratory,ThO_2in secular equilibrium with its daughter radionuclides, with an absolute activity of 1087.4 Bq. The ThO_2 standard source spectrum is shown in Fig. 2.

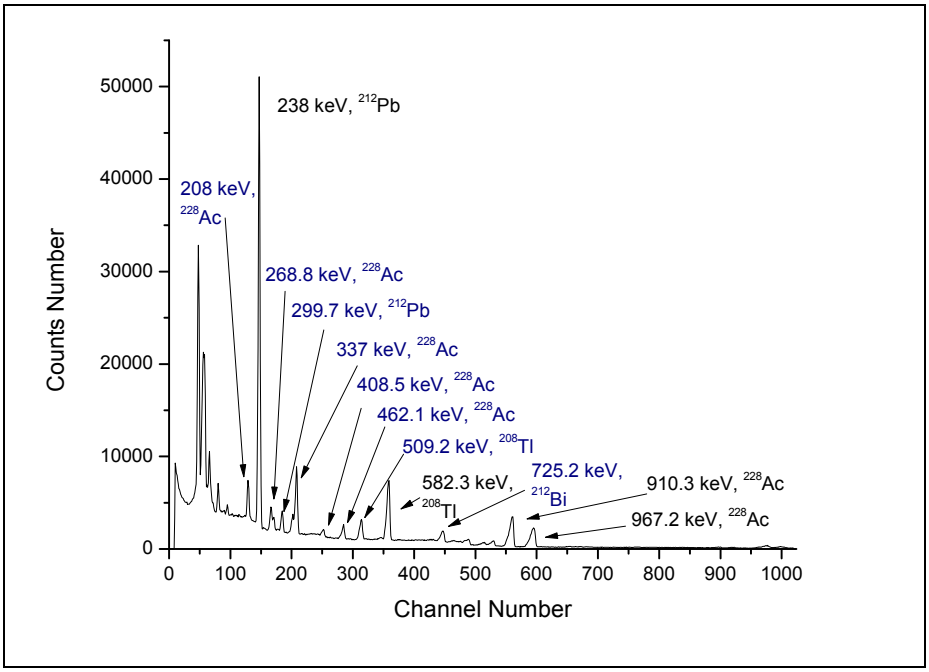

Fig. 2. Gamma spectrum of the ThO_2 calibration source (acquisition time 30 min.)

3. Results and discussion

The detector efficiency at different energies was calculated by using the formula:

$$\varepsilon = \frac{N}{\varepsilon_g \cdot t \cdot \Lambda \cdot p} \tag{2}$$

where N- is the peak area, t – is the acquisition time of the spectrum, Λ- is the activity of the calibration source and ε_g is the geometrical efficiency, and the probability, p, of decay of the ^{232}Th family from ref. [11]. The installation efficiency curve (Fig. 3) was obtained with ThO_2, for sources distance of 0 cm. With the values measured at different energies, the absolute activity of the samples and neutron flux were calculated.

The sample of In, Au, Mn and Sm are placed to activation until saturation, the γ spectrum in a predetermined measurement time (Fig. 4) is determined and in each case the thermal neutron flux in the sample channel system containing two isotopic neutron sources was calculated. The results of the neutron fluxes of these reactions are shown in Table 3.

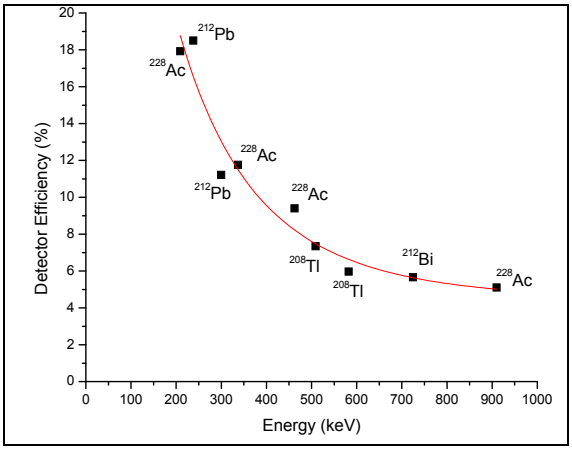

Fig. 3. Detector efficiency curve

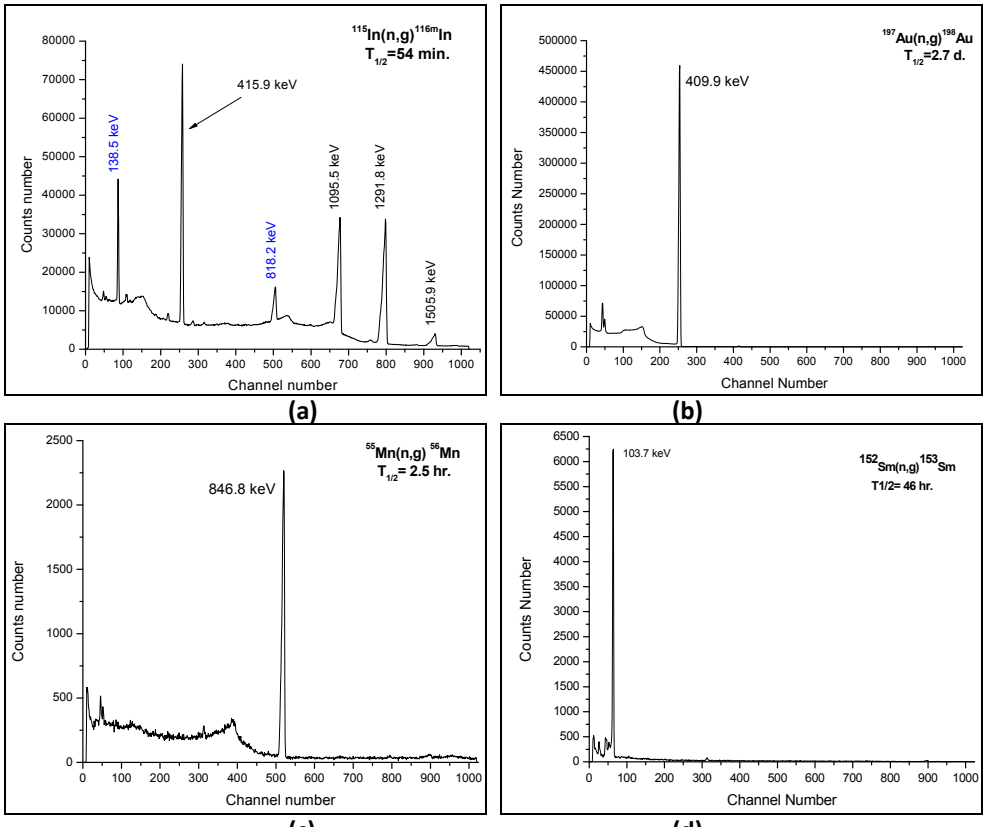

Fig. 4. The gamma spectra of activated samples used as neutron detector (**a -** ^{116m}In sample, **b -** ^{198}Au sample, **c -** ^{56}Mn sample, **d -** ^{153}Sm sample)

Table 3. Neutron flux determined by activation method

Nuclear reaction as detector	Neutron flux ($n/s \cdot cm^2$)	Resonance neutron energy (eV)	Resonance cross section (barns)
$^{115}In(n,\gamma)\ ^{116m}In$	$1.1 \cdot 10^4$	1.457	2700
$^{197}Au(n,\gamma)\ ^{198}Au$	$3.7 \cdot 10^4$	4.905	1150
$^{55}Mn(n,\gamma)\ ^{56}Mn$	$2 \cdot 10^3$	337	15.7
$^{152}Sm(n,\gamma)^{153}Sm$	$1.3 \cdot 10^3$	8.7	3050

Also, indium foils were placed at different distances relative to the ^{241}Am-^{9}Be &^{239}Pu-^{9}Be double-source. After analyzing the gamma spectrum of each foil, the thermal neutron flux distribution on the channel axis of the installation was calculated, resulting approximately a linear lowering (Fig.5).

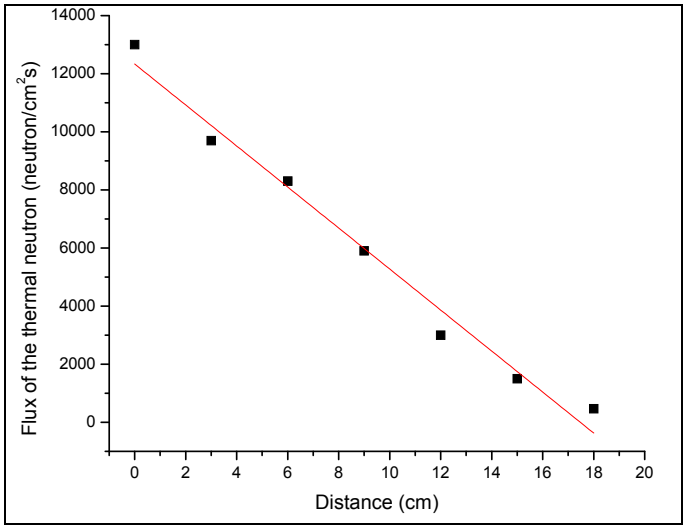

Fig. 5. The distribution of neutron flux in to channel of installation.

4. CONCLUSION

The activation method provides a good technique to measure the thermal neutron flux produced by isotopic neutron sources in the channels of paraffin block. The neutron fluxes determined by activation method, of 10^4 $n/s \cdot cm^2$, are comparable with that reported for sources used in boron neutron capture, that will be tested in a future work.

REFERENCES

[1] G. Brownell, R.G. Zamenhof, B.W. Murray, G.R. Wellum, *Boron Neutron Capture Therapy*, In: Therapy in Nuclear Medicine, R.P. Spencer (ed.), Grune and Stratton, Inc., New York (1978)

[2] R.F. Barth, A.H. Solloway, R.G. Fairchild, *Cancer. Res*. 50, 1061-1070 (1990)

[3] J. Ghassoun, D. Mostacci, V. Molinari, A. Jehouani, *Appl. Radiat. Isotopes*, 68, 265–270 (2010)

[4] T. Kageji, Y. Mizobuchi, S. Nagahiro, Y. Nakagawa, H. Kumada, *Appl. Radiat. Isotopes,* 69, 1823–1825 (2011)

[5] L. Yasui, T. Kroc, S. Gladden, C. Andorf, S. Bux, N. Hosmane, *Appl. Radiat. Isotopes,* 70, 6–12 (2012)

[6] J. Ghassoun, B. Chkillou, A. Jehouan, *Appl. Radiat. Isotopes,* 67, 560–564 (2009)

[7] S. Masunaga, Y. Sakurai, H. Tanaka, M. Suzuki, Y. Liu, N. Kondo, A. Maruhashi, Y. Kinashi, K. Ono, *Brit. J. Radiol*., 85, 249–258 (2012)

[8] T. Fiat, L. Dărăban, *Studia UBB Physica*, 74-77 (1976)

[9] J. Perdijon, *L'analyse par activation,* p.7. Ed. Masson et Cie, Paris (1987)

[10] R. Baritschi, L. Daraban*, Studia UBB Physica*, LVI, 2, p. 3-14 (2011)

[11] N. Lavi, Z.B. Alfassi, *Appl. Radiat. Isotopes* 61, 1437–1441 (2004)

STUDIA UBB PHYSICA, Vol. 58 (LVIII), 1, 2013, pp. 13-20
(RECOMMENDED CITATION)

PREPARATION BY HIGH ENERGY BALL MILLING AND MAGNETIC PROPERTIES OF NANOCRYSTALLINE $La_{1.4}Ca_{1.6}Mn_2O_7$ PEROVSKITE

B R. DUDRIC[a,*], M. SEVER[a], E. DOROLTI[a], R. TETEAN[a]

ABSTRACT. Nanocrystalline double layered $La_{1.4}Ca_{1.6}Mn_2O_7$ powders were synthesized by grinding the constituent oxides in air at room temperature, using a high-energy planetary mill. The reaction process, evaluated by analyzing the evolution of the crystalline structure in the XRD patterns, is completed after about 15 h. Energy dispersive x-ray microanalysis of the final sample revealed a good homogeneity of the powder with composition nearly identical to the nominal one. The grain morphology observed by Scanning Electron Microscopy shows the aggregation of the nanocrystals in fine particles. The magnetic measurements indicate that the perovskite nanoparticles with sizes smaller than 10 nm obtained by reacting milling have significant defects at the surface, leading to a serious decrease of the magnetic moments in comparison to the bulk material.

Keywords: *nanoparticles; double layered perovskite; high energy ball milling*

INTRODUCTION

The double-layered manganites belonging to the Ruddelsden-Popper series have attracted many researches in the last two decades due to their intriguing properties such as colossal magnetoresistance, charge ordering, anisotropic transport in charge carriers, and the possibility of a short-range magnetic ordering above the 3D ferromagnetic transition temperature [1-7]. The doped $R_{2-2x}A_{1+2x}Mn_2O_7$ perovskites (R is a trivalent rare earth ion and A is a divalent alkaline earth cation) consist of MnO_2 bilayers separated by insulating $(R,A)_2O_2$ rock-salt layers, stacked along the *c*-axis, leading to a quasi-two-dimensional structure. The physical properties of these materials are sensitive to small changes in composition and structure due to

[a] Babeş-Bolyai University, Faculty of Physics, 1 Kogălniceanu Str., 400084 Cluj-Napoca, Romania
* Corresponding author: roxana.pacurariu@phys.ubbcluj.ro

their layered structure [4]. The inherent anisotropy of the double layered manganites and its consequences for studying low-dimensional physics, as well as the remarkable range of physical properties have generated much interest. Among other intriguing properties $La_{2-2x}Ca_{1+2x}Mn_2O_7$ perovskites exhibit colossal magnetoresistance (CMR) effect at low temperatures [1,3,8] and large magnetic entropy change under a moderate magnetic field [9-11]. It is well known that the preparation conditions of these materials influence their physico-chemical properties, in particular the magnetic transition Curie temperature and the magnetic entropy change. Besides the standard ceramic reaction at high temperatures, sol-gel [9] and coprecipitation [12] chemical methods are successfully used to produce double layered manganites. The ceramic method is simple to use and requires cheap and easily available oxides as starting materials, but has the drawbacks of high reaction temperature, large particle size and limited chemical homogeneity. The chemical solution methods provide highly homogeneous particles with large specific surface area, but they are generally complicated and the agents used can be very expensive. A satisfactory method for obtaining fine and homogeneous double layered perovskite powders may be mechanochemical synthesis, which is a powerful method for the production of novel, high performance and low cost materials such as ferrites or intermetallics. High-energy milling was successfully used to obtain stoichiometric manganites powders with large specific area, by grinding constituent oxides at room temperature [13,14].

In this paper we report the single step synthesis of nanocrystalline $La_{1.4}Ca_{1.6}Mn_2O_7$ double layered manganite powders via high-energy milling of oxide precursors and the investigation of the magnetic properties.

EXPERIMENTAL

$La_{1.4}Ca_{1.6}Mn_2O_7$ nanoparticles were synthesized from 99.99% purity oxides of La_2O_3, CaO, MnO and MnO_2. The oxides were mixed in stoichiometric proportions and mechanically milled in air using a high-energy planetary mill (Fritsch Pulverisette 4) with 440C hardened steel balls and milling vial. The milling speed of the vial was 900 rpm and the ball-to-powder ratio of 10:1. The powder milling process was interrupted several times and small amounts of powder were taken out of the vial. In order to prevent the excessive overheating of the containers, the experiments were carried out by alternating 120 min of milling with 30 min of rest. For magnetic measurements the powders were pressed into pellets of 10 mm diameter under a pressure of 1 ton, heated in air to 500^{o}C for 12 h and slowly cooled to room temperature.

The crystallographic, morphological, and compositional properties of the samples were investigated by X-ray diffraction (XRD) and scanning electron microscopy with energy dispersive spectroscopy (SEM-EDS). X-ray powder diffraction data were

collected at room temperature by using a Bruker D8 Advance AXS diffractometer with Cu Kα radiation in the 2ϑ region 20°-65°. The crystallite-sizes were calculated using the Debye-Scherrer formula:

$$D = \frac{k\lambda}{\beta \cos\theta}$$

where β is the peak full width at half maximum (in radians) at the observed peak angle ϑ, k is the crystallite shape factor (was considered 0.94) and λ is the X-ray wavelength (0.154 nm). Scanning electron microscopy (SEM) and X-ray microanalysis studies were performed on a Jeol-JSM 5800LV microscope equipped with an EDX spectrometer.

Magnetic measurements were carried out using a 12 T VSM from Cryogenics in the temperature range 4.2 – 300 K and external magnetic field up to 12 T. Both zero-field-cooled (ZFC) and field-cooled (FC) measurements were performed.

RESULTS AND DISCUSSION

The XRD patterns of the powders milled for different periods of time (t_{mill} = 2 h, 5 h, 7 h, 9 h, 11 h, 13 h, 15 h) are shown in Fig 1.

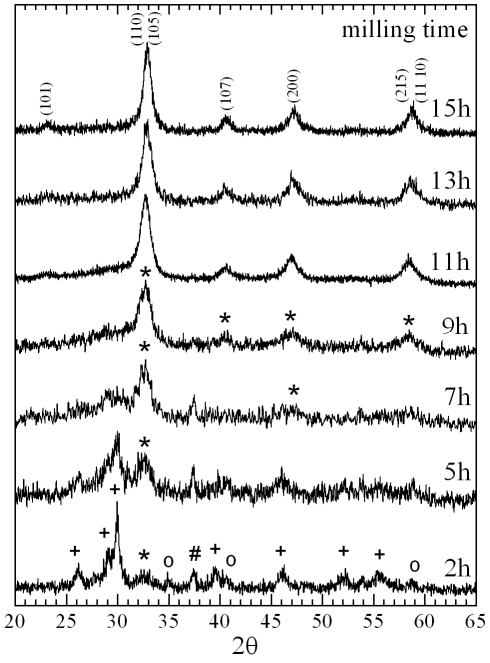

Fig. 1. XRD patterns of the mixture milled for different periods of time:
(+) La_2O_3, (o) CaO/MnO, (#) MnO_2, (*) $La_{1.4}Ca_{1.6}Mn_2O_7$

The reaction process was evaluated by analyzing the evolution of the crystalline structure of the milled powders using the PowderCell program [15]. After 2 h of milling the typical patterns of the starting oxides La_2O_3, CaO, MnO and MnO_2 can be observed, but for milling time higher than 5 h the perovskite phase is preponderant. Single phase $La_{1.4}Ca_{1.6}Mn_2O_7$ powders were obtained after 13 h milling time. Fig. 2 shows the change in the percentage of the $La_{1.4}Ca_{1.6}Mn_2O_7$ phase in the milled sample as function of milling time. The percentage increases rapidly with the milling time in the early stage of the operation and reaches values above 90% after 9 h of milling.

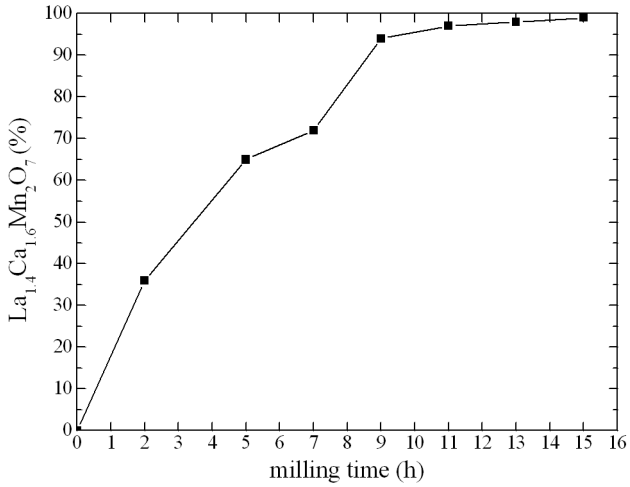

Fig. 2. The change in the percentage of the $La_{1.4}Ca_{1.6}Mn_2O_7$ phase with the milling time

The profiles of the diffraction peaks in Fig. 1 are broadened, suggesting that the synthesized powders are crystallites of nanoscale size. For milling time higher than 11 h, for which the percentage of the $La_{1.4}Ca_{1.6}Mn_2O_7$ phase is larger than 95 %, the lattice parameters, c/a ratios and crystallite-sizes (calculated using the Debye-Scherrer formula for the (200) diffraction maxima) were obtained from the XRD patterns and collected in Table 1. The values obtained for the *c* lattice parameter and *c/a* ratio are clearly smaller than the values obtained previously for $La_{1.4}Ca_{1.6}Mn_2O_7$ synthesized by standard ceramic reaction (*c* = 19.240 Å, *c/a* = 4.979) [11] or sol gel (*c* = 19.156 Å, *c/a* = 4.982) [16], suggesting that for small crystallite size (less than 10 nm) the lattice contracts preferably in the *c*-direction rather than in the *a*-direction.

Compositional analysis was performed by energy dispersive x-ray microanalysis (EDX) on the powder milled for 15 h. The analysis revealed a good homogeneity of the powder (Fig. 3) with composition nearly identical to the nominal one within the accuracy of EDX.

Table 1. Lattice parameters, c/a ratio and crystallite sizes estimated from XRD patterns

Milling time	$La_{1.4}Ca_{1.6}Mn_2O_7$ phase (%)	a (Å)	c (Å)	c/a	χ^2	Crystallite size (nm)
11 h	97	3.86(1)	19.04(9)	4.93(4)	1.41	7.2
13 h	98.5	3.84(7)	18.95(3)	4.92(7)	1.23	7.9
15 h	> 99	3.84(2)	19.00(9)	4.94(7)	1.31	9.8
Pressed pellet	> 99	3.84(2)	19.02(5)	4.95(2)	1.33	9.8

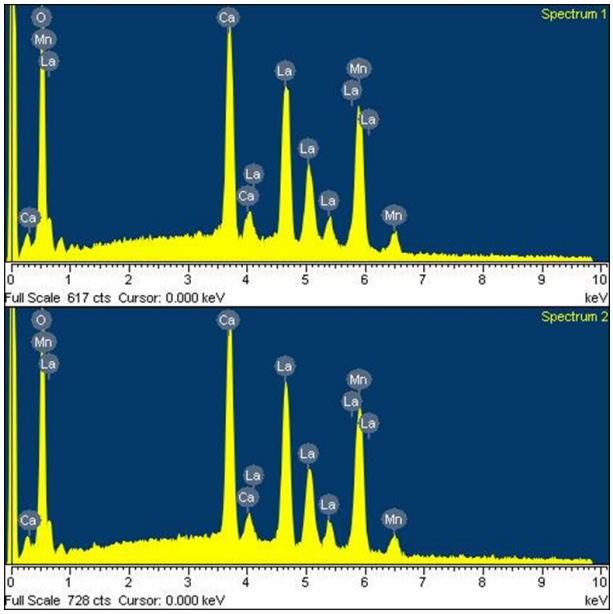

Fig. 3. EDX data for the powder milled for 15 h

The grain morphology was observed by Scanning Electron Microscopy. Fig. 4 shows the granular nature of $La_{1.4}Ca_{1.6}Mn_2O_7$ powder milled for 15 h and the aggregation of the nanocrystals in fine particles.

Fig. 5 shows the temperature dependence of the magnetization for the powder milled for 15 h and pressed into pellet, in zero field cooling (ZFC) and field cooling (FC) modes recorded under a magnetic field of 0.2 T. With decreasing temperature the ZFC and FC magnetizations show an increase in the temperature range of 50 – 200 K and a clear splitting at low temperatures with a maximum of the ZFC curve at about 30 K, indicating the formation of ferromagnetic particles and the collecting freezing of the moments of the magnetic clusters. The magnetic

order temperature, defined as the temperature corresponding to the minimum of d*M*/d*T* is about 60 K. The wide ferromagnetic transition in double layered manganites is due to the appearance of short range 2D-magnetic order at temperatures higher than the 3D-ferromagnetic transition temperature [1,17], which is also responsible for the non zero magnetization value at room temperature.

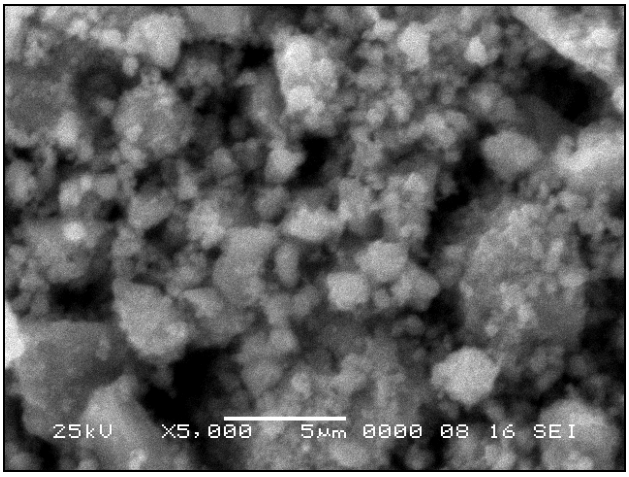

Fig. 4. SEM image of the final $La_{1.4}Ca_{1.6}Mn_2O_7$ powder

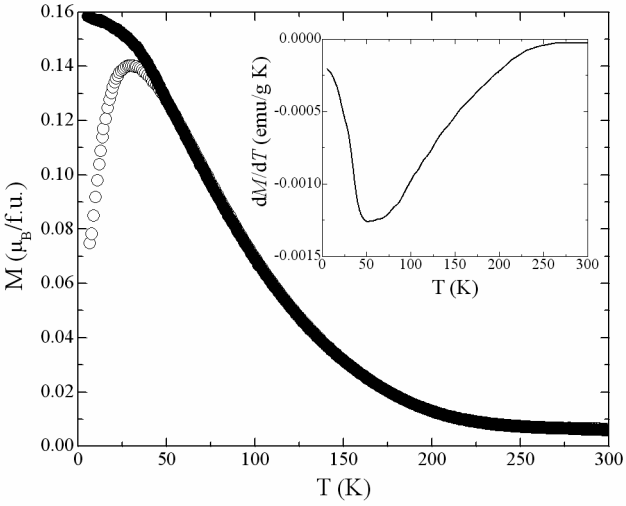

Fig. 5. Temperature dependence of ZFC (open symbols) and FC (filled symbols) magnetizations in 0.2 T

The difference between the FC and ZFC curves is possibly due to magnetic frustration induced by the surface driven spin frustration and disorder in nanoparticles. A model in which the nanoparticles consist of an inner part with properties similar to the bulk material and a magnetically disordered surface layer containing most of the oxygen and crystallographic defects, has been successfully used to explain the magnetic behavior of nanosized manganites [18-20]. As shown in Fig. 6 the magnetization of the investigated sample does not reach saturation even in magnetic fields of 12 T at 5 K. This may be an effect of the small particle sizes for which the surface contribution is large and therefore leads to the diminution of the total magnetization.

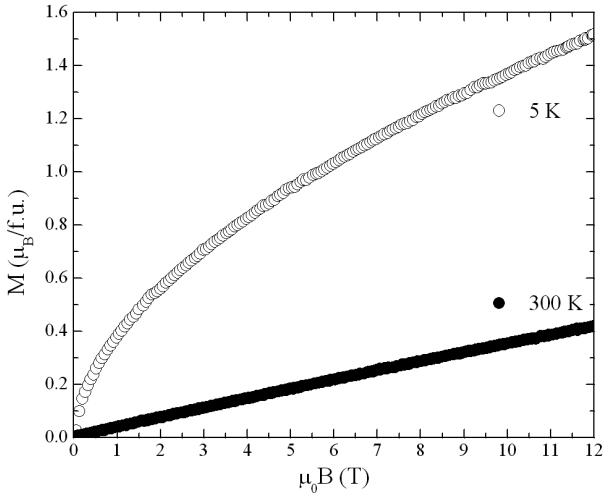

Fig. 6. *M(H)* curves at 5 K and 300 K in magnetic fields up to 12 T

CONCLUSIONS

We have shown that nanocrystalline $La_{1.4}Ca_{1.6}Mn_2O_7$ double layered manganite powders can be synthesized at room temperature by high-energy milling of oxide precursors in a the single step process. The reaction increases rapidly with the milling time and is completed after 15 h. The obtained powder consists of nanocrystals with sizes smaller than 10 nm, aggregated in fine particles. The magnetic measurements indicate that the perovskite nanoparticles obtained by reacting milling have significant defects at the surface, leading to a serious decrease of the magnetic moments in comparison to the bulk material. The results recommend high-energy milling as an effective method to prepare nanosized double layered manganites.

ACKNOWLEDGEMENTS

This work was possible with the financial support of the Sectoral Operational Programme for Human Resources Development 2007-2013, co-financed by the European Social Fund, under the project POSDRU 89/1.5/S/60189 - „Postdoctoral Programs for Sustainable Development in a Knowledge Based Society" and from the Romanian UEFISCDI Project No. PN-II-ID-PCE-2011-3-0583 (85/2011).

REFERENCES

[1] Y. Moritomo, A. Asamitsu, H. Kuwahara, Y. Tokura, *Nature,* 380, 141-144 (1996).

[2] H. Asano, J. Hayakawa, M. Matsui, *Phys. Rev.,* B 56, 5395 (1997).

[3] H. Asano, J. Hayakawa, M. Matsui, *Appl. Phys. Lett.,* 70, 2303 (1997).

[4] N.H. Hur, J.T. Kim, K.H. Yoo, Y.H. Park, J.C. Park, E.O. Chi, Y.U. Kwon, *Phys. Rev B*, 57, 10740 (1998).

[5] T. Kimura and Y. Tokura, Annu. *Rev. Mater. Sci.,* 30, 451 (2000).

[6] Sandip Chatterjee, P.H. Chou, C.F. Chang, I.P. Hong, and H.D. Yang, *Phys. Rev. B*, 61, 6106A (2000).

[7] C.D. Ling, J.E. Millburn, J.F. Mitchell, D.N. Argyriou, J. Linton, and H.N. Bordallo, *Phys. Rev. B,* 62, 15096 (2000).

[8] H. Asano, J. Hayakawa, and M. Matsui, *Appl. Phys.Lett.*, 68, 3638-3641(1996).

[9] Tie-Jun Zhou, Z. Yu, W. Zhong, X.N. Xu, H.H. Zhang, and Y.W. Du, *J. Appl. Phys.*, 85, 7975-7978 (1999).

[10] H. Zhu, H. Song, Y.H. Zhang, *Appl. Phys. Lett*., 81, 3416-3419 (2002).

[11] R. Tetean, C. Himcinschi, E. Burzo, *J. Optoelectron. Adv. Mater.,* 10, 849-852 (2008).

[12] J. Tanaka, K. Takahashi, Y. Yajima, M. Tsukioka, *Chemistry Letters,* 11, 1847 (1982).

[13] Q. Zhang, F. Saito, *J. Alloys Compd.,* 297, 99-103 (2000).

[14] Q. Zhang, T. Nakagawa, F. Saito, *J. Alloys Compd.*, 308, 121-125 (2000).

[15] W. Kraus, G. Nolze, *J. Appl. Cryst*., (1996). 29, pp. 301—303

[16] R. Dudric, F. Goga, M. Neumann, S. Mican, and R. Tetean, *J. Mater. Sci.*, 47, 3125-3130 (2012).

[17] T. Kimura, Y. Tomioka, H. Kuwahara, A. Asamitsu, M. Tamura, and Y. Tokura, *Science,* 274, 1698-1701 (1996).

[18] M.A. López-Quintela, L.E. Hueso, J. Rivas and F. Rivadulla, *Nanotechnology,* 14, 212-219 (2004).

[19] S. Roy, I. Dubenko, D.D. Edorh, and N. Ali, *J. Appl. Phys*., 96, 1202-1207 (2004).

[20] P. Dey and T.K. Nath, *Phys. Rev. B*, 73, 214425 (2006).

STUDIA UBB PHYSICA, Vol. 58 (LVIII), 1, 2013, pp. 21-25
(RECOMMENDED CITATION)

RADIOMETRIC DETERMINATION OF POTASSIUM-40 IN SOILS BY γ RADIATION MEASUREMENTS

A. HAPCA[a] AND L. DARABAN[b,*]

ABSTRACT. The paper presents a simple method for measuring K-40 from soil using a NaI(Tl) detector enclosed in lead shield. The lowered content of potassium points out on the soil degradation related to the invasive plants. Attention must be paid to the possible interference of gamma radiation emitted by K-40 with the gamma radiation emitted by 228Ac, a descendent of 232Th from soil.

Keywords: *K-40, γ- radioactivity, soil degradation*

1. INTRODUCTION

One of the light soluble elements in the soil is potassium, of which natural radioisotope ^{40}K spontaneously disintegrates 0.119 %, having a half-life of $T_{1/2} = 1.28 \cdot 10^9$ years, emits β radiation with a maximum energy of 1.33 MeV and also γ radiation with energy of 1.46 MeV, according to the disintegration scheme in Fig. 1. The specific activity of the K element is de $3 \cdot 10^5$ Bq/kg (8.3 μCi/kg). By its disintegration, 31 β^-/ gram particles per second are emitted through the transition $^{40}K \rightarrow ^{40}Ca$ and also, 3.4 quanta γ/gram per second are emitted through the transition $^{40}K \rightarrow ^{40}Ar$.

In fact, the disintegration scheme from Fig. 1 is more complex for the transition branch $^{40}K \rightarrow ^{40}Ar$, which takes place in 3 modes [1]: one is the main mode by the electronic capture C.E., by which an electron from the layer of the atom of potassium is captured in the nucleus producing the conversion of a neutron to a proton, the nucleus Ar is formed in an excited state, going fast into a fundamental state and emitting a γ radiation with an energy of 1.46 MeV.

[a] University of Agricultural Sciences and Veterinary Medicine, Cluj-Napoca, Romania
[b] Babeş-Bolyai University, Faculty of Physics, Cluj-Napoca, Romania
* Corresponding author: liviu.daraban@phys.ubbcluj.ro

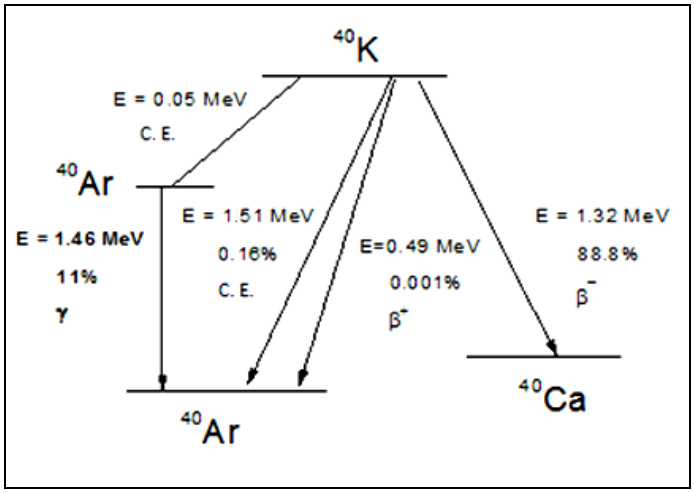

Fig. 1. The disintegration scheme of ^{40}K

There is also another process almost similar, which consists of the electronic capture without the emission of a γ quantum. This is not so often (with a probability of 0.16 %), and induces an error, especially on the disintegration constant and the measured activity of ^{40}K.

The third mechanism of the transformation of ^{40}K to ^{40}A consists in the emission of a positron (β^+ disintegration), which has as effect the transformation of a proton to neutron. This mode of disintegration is still not so clear as the second mechanism (with a probability of 0.001 %) and will not affect the determined concentration of K [1].

Due to the fact that the number of γ quanta emitted by the sample which contains K, is directly proportional to the number of atoms of K found in the sample, the quantitative measurement of the activity of the sample makes possible the determination of the concentration of potassium [2-4]. Therefore, the dosing of the potassium can be done by measuring it, but also by the determination of ^{40}Ar produced in a short interval of time, measured with a mass spectrometer [1].

In the last decades, the problems related on the environment were stressed out more and more. The migration of some species of plants and animals over the geographical barriers was not a problem anymore. In our days, the strongest biological threat on the biodiversity is caused by the apparition of some species in new habitats, which later became invasive. One of the first 100 invasive plants in Europe is *Reynoutria Japonica*. It came to Europe as an ornamental plant [5,6] and managed to pass the climatic barriers, becoming dangerous for the invaded ecosystems. *Reynoutria japonica* has the ability to form populations in any grassy vegetation,

shortly covering 100 %. The airy stems after being dried during the winter and autumn, the soil is slowly washed, leading to the grow of the soil erosion, especially on the rivers shores, [7], causes the alteration of the hydria regime and the quality of the rivers water and the physical properties of the soil [8]. The potassium level is an indication on the degradation of soil.

2. EXPERIMENTAL

The measurements of ^{40}K were made with the help of a monochannel analyser type RFT20160 coupled with a scintillation probe equipped with a NaI(Tl) crystal of 2"x 2" size, and a photomultiplier, a led tower with a thickness of 6 cm and a high 25 cm in order to shield the background. This equipment can successfully execute measurements of low activities up to 1 pCi, typical for environmental samples. The efficiency of the detector is about 8 % for a window in the range of 800-1500 keV after ThO_2 method calibration in efficiency [9].

The times of measurement was chosen to de t = 10^3 s, each measurement being repeated 3 times, which is sufficient since the equipment has a high counting efficiency. The calibration of the potassium activity was made with a dehydrated sample of K_2CO_3, with a mass of m = 114.66 g and the calculated absolute gamma activity of Λ = 220 Bq. The geometrical factor is included in this efficiency, the samples and the standard source having the same measurement geometry.

The absolute activity Λ of the ^{40}K in the sample is given by the formula [4]:

$$\Lambda = \frac{\overline{N}}{1000}\frac{1}{\varepsilon}f_a \tag{1}$$

where the self-shielding factor in the detection crystal of the gamma radiation is f_a = 1.2, ε is the efficiency of detector at the energy of ^{40}K of 1.46 MeV, $\overline{N}$ is the average value of the *n* counts.

The standard deviation gives an experimental counting error and was calculated with the formula:

$$\sigma_{\exp} = \sqrt{\frac{\sum_{i=1}^{n}(N_i - \overline{N})^2}{n-1}} \tag{2}$$

For *n* measurements, $\overline{N}$ is the average of the number of measured counts.

3. RESULTS AND DISCUSSION

The soil samples measurements is shown in Table 1.

Table 1. Total γ-counts and average values of K radioactivity measurement in soils samples from experimental sites with *Reynoutria japonica* plants

Nr.crt.	Background	K_2CO_3 calibration sample (114.66 g)	Soil sample 1 (140 g)	Soil sample 2 (119 g)	Soil sample 3 (145 g)
1	2149	3437	2201	2241	2222
2	2195	3447	2159	2228	2325
3	2185	3541	2231	2199	2267
Average value	**2166.3**	**3475**	**2197**	**2222.6**	**2271.3**
σ (%)	0.8	1.6	1.6	0.97	2.2

Table 2. The number of counts/1000 sec for samples with high content of K

Nr.crt.	Background	K_2CO_3 Calibration sample (114.66 g)	Wood Ash (46 g)	Salt soil from Pata village (115 g)
1	2128	3409	2258	2314
2	2194	3446	2351	2382
3	2175	3489	2291	2359
Average value	**2165.6**	**3448**	**2300**	**2351.6**
σ (%)	1.6	1.16	2.0	1.5

By taking into account the scheme factors S_γ and S_β (Fig. 1), the global activity $(\gamma + \beta)$ of the sample can be estimated, knowing also that ^{40}K represents 0.119 % of the total K. The potassium quantity in the sample can be therefore determined and correcting it with the mass of the sample, the potassium concentration in the soil can be estimated in gK/kg.

4. THE DISTRIBUTION OF ^{40}K CONCENTRATIONS IN SOIL

Table.3 The experimental results of K concentrations in soil samples

Sample	K concentration (g/kg)	^{40}K-Activity (Bq/kg)
Soil 1	7.5	2.2
Soil 2	19.7	5.9
Soil 3	32	9.6
Wood Ash	145	43
Salt Soil	81	24

Our K concentration is very low. Because the ^{40}K activity concentration in soil follows homogeneous distribution, its changes depend on the nature of soil and increases in agriculture areas as a result of fertilizers applications [3] or earth activity along a fracture zone [10]. The area where invasive plants or weeds are large consumers of potassium is less extended, these is indicated by soil from which we harvested our samples.

Observation: ^{40}K is measured through its 1460.8 keV gamma line. However, until now it has been ignored that this line is mixed with the 1459.2 keV line of ^{228}Ac from the chain of ^{232}Th. According to [3] the data from literature, it shows wrong data about the concentration of ^{40}K, although in many cases the error is large.

It should be emphasized that even if the correction in ^{40}K concentration is large, the correction of external dose is negligible due to the higher weighing factor for ^{232}Th than for ^{40}K (by at least a factor of 10).

5. CONCLUSION

We developed a radiometric method to determine the potassium from soil based on ^{40}K γ-radioactivity. The measurement accuracy was 97 %, demonstrating a smooth sensitivity of the measurement device. The determinations of K are showing soil erosion by invasive plants.

REFERENCES

[1] G. Vasaru, C. Cosma, Geocronologie nucleara, pp.78-80, Ed. Dacia, Cluj-Napoca, 1998.

[2] O. Baykara, M. Dogru, *Radiation Measurements*, 44,116–121, (2009).

[3] N. Lavi, F. Groppi, Z.B. Alfassi, *Radiation Measurements,* 38, 139 – 143 (2004).

[4] F.T. da Conceicao, D.M. Bonotto, J.R. Jimenez-Rueda, J.A. Frutuoso Roveda, *Appl. Radiat. Isotopes,* 67, 1114–1120 (2009)

[5] A.P. Conolly**,** *Watsonia,* 11,p. 291-311 (1977).

[6] M. Rejmanek, D.M. Richardson, *Ecology,* 77, p. 1655-1661 (1996).

[7] R. Wittenberg, An inventory of alien species and their thread to biodiversity and economy in Switzerland. *CABI Bioscience Switzerland Center report to the Swiss Agency for Environment, Forest and Landscape*, 416 pp. (2005).

[8] J.N. Barney, N. Tharayil, A. DiTommaso, P.C. Bhowmik, *Canadian J. Pl. Sci.*, 887-905 (2006).

[9] R. Baritschi, L. Daraban, *Studia UBB Phys*., LVI, 2, p.3-14 (2011)

[10] O. Baykara, M. Dogru, *Radiation Measurements,* 44 (2009) 116–121

STUDIA UBB PHYSICA, Vol. 58 (LVIII), 1, 2013, pp. 27-32
(RECOMMENDED CITATION)

MICROSTRUCTURAL PROPERTIES OF SOL-GEL DERIVED BIOGLASSES CONVENTIONALLY STABILIZED BY CALCINATION *VERSUS* REPEATED IMMERSION IN VOLATILE SOLVENT

I. RITI[a], A. VULPOI[a], A. URECHE[a], V. SIMON[a,*]

ABSTRACT. The sol-gel route is one of the most important way to obtain bioactive glasses at room temperature. The quick alkali-mediated process diminishes the gelation time at few minutes. The SiO_2-CaO system was prepared via quick alkali-mediated sol-gel route and stabilised with thermal treatment at 600ºC and ethanol immersion process respectively. Thermal, structural and surface analyses were performed on the sample by means of differential thermal analysis (DTA/TGA), X-ray diffraction (XRD), Fourier transform infrared spectroscopy (FTIR), and scanning electron microscopy (SEM). These results support the new method of stabilization by alcohol immersion these samples having the same properties of the calcined xerogel with an increased specific surface area and pore volume.

Keywords: *sol-gel stabilization; calcination; volatile solvent repeated immersion.*

INTRODUCTION

Bioactive glasses have been studied since 1970 by Hench and co-workers who investigated Si-Ca-based materials [1-3]. The sol-gel technology, as synthesis method, is a low temperature preparation technique that provides a convenient way to obtain bioactive glasses [2, 4]. The traditional sol-gel process is wholly long because the synthesis involves six steps [4, 5]. *(i)* The first step presumes the mixing of precursors which forms the sol. *(ii)* The network formation starts by gelation of the sol. *(iii)* The next step consists in the aging of the gel, when the liquid phase is collected in the pores of the three dimensional gel network. *(iv)* It follows the gel drying when the pore liquid and the physically adsorbed water are eliminated from the pores. *(v)* The complete drying is provided by heating at temperatures higher than 100 ºC [4].

[a] Faculty of Physics & Institute for Interdisciplinary Research on Bio-Nano-Sciences, Babes-Bolyai University, M. Kogalniceanu 1, 400084, Cluj-Napoca, Romania
* Corresponding author: viorica.simon@phys.ubbcluj.ro

(vi) The last step is the stabilization of the resulted xerogel in order to confer bioactivity to the obtained matrix [4]. The studies on the effect of stabilizing temperature on the sample bioactivity pointed out a better bioactivity for the samples stabilized at lower temperatures [6, 7] and for this reason the stabilizing temperature for bioactive glasses is usually selected in the range 500-900ºC [4]. Recently it was proposed as alternative stabilization method to obtaine xerogel the replacing of the water with ethanol as the pore fluid by repeated immersions of the obtained gel powders in ethanol; hence this fluid exerts a low drying stress and gives higher specific surface area after drying [5].

In this study for the preparation of xerogels the quick alkali-mediated sol-gel method was chosen, method that presumes ammonia addition in the sol, to reduce the gelation time from several days to several minutes [8, 9]. For stabilization of the obtained xerogels were used two stabilisation methods, calcinations at 600 ºC and the alternative ethanol immersion method. The objectives of this research work are to synthesize and compare the effects of the two xerogel stabilization techniques on the $75SiO_2$ 25CaO (mol%) sol-gel derived bioglasses.

MATHERIALS AND METHODS

Sample synthesis

The sample with the composition $75SiO_2 \cdot 25CaO$ (mol %) was prepared via quick alkali mediated sol-gel route. The sol-gel was obtained by hydrolysis and condensation reactions using tetraethoxysilan $SiC_8H_{20}O_4$ (TEOS) as precursor for SiO_2 and calcium nitrate tetrahydrate $Ca(NO_3)_2 \cdot 4(H_2O)$ as precursor for CaO. Initially was performed the hydrolysis of TEOS in distilled water, in a weight ratio of 1:1, and this solution was stirred with a magnetic stirrer for 30 minutes at room temperature. The pH of the solution was adjusted at ~1.5 with nitric acid (as a hydrolysis catalyst). The precursor of CaO was dissolved in distilled water on a magnetic stirrer for 20 minutes at room temperature. The two solutions were mixed under continuous stirring for 20 minutes and then it was added 0.5 ml ammonia for instant gelation. The gel was matured for 2 days at room temperature, and thereafter dried at 110ºC for 24 hours to eliminate the excess of water derived from the hydrolysis. Half of the obtained white powder was calcinated at 600 ºC (noted SiCa-tt600) and the other half was repeatedly immersed in ethanol and then dried again at 110 ºC (noted SiCa-EtOH).

Experimental techniques

Differential thermal analysis and termogravimetric analyses were performed with a Shimadzu differential thermal analyser DTG-60H to investigate the thermal evolution of the sample, which simultaneous recording of TG and DTA curves, in air,

using alumina crucibles, with heating rate of 10ºC/minute, from room temperature to 1000ºC.

The structure of the samples was investigated with a Shimadzu XRD-6000 diffractometer, using Cu Ka radiation (λ =1.5418 Å), with Ni-filter, with a speed of 2 degrees/minute, between 10 and 80^{o} (2 theta), and with JASCO FT/IR 6200 spectrometer in absorption mode in 4000 to 400 cm^{-1}spectral range with a spectral resolution of 4 cm^{-1} using KBr pellet technique.

Specific surface areas of the samples were determined by measuring nitrogen adsorption/desorption at 77 K with Qsurf Series M1 surface area analyzer, on the basis of Brunauer, Emmett and Teller (BET) method. For all samples the measurements were performed under similar conditions using one point BET method with 30% N_2, 70% He gas mixture.

Scanning electron microscopy (SEM) images were obtained with a FEI Quanta 3D FEG dual beam microscope.

RESULTS AND DISCUSSION

The DTA and TG thermograms (Fig. 1) show the thermal evolution of the as prepared, the thermally treated and EtOH washed samples.

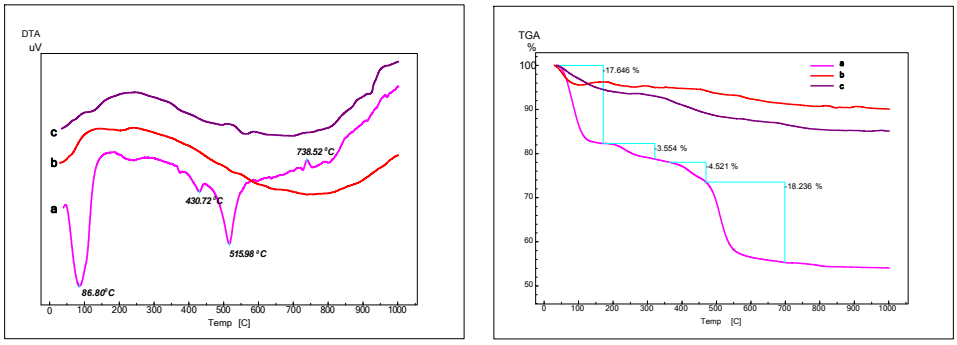

Fig. 1. DTA and TGA thermograms for SiCa (a), SiCa-EtOH (b), SiCa-tt600 (c) samples.

The DTA curve of the as prepared xerogel (SiCa) presents a first endothermic peak located around 88ºC associated with a weight loss in the TG curve due to water elimination from the surface of the sample. The next endothermic peak at 430ºC most likely arises from the organic and nitrate groups decomposition. The weight loss of ~18% around 515ºC can be attributed to the dehydroxylation event. The exothermic event at 738ºC is due to partial crystallization and transformation of the glass into glass-ceramic. The results obtained for the sample calcinated at

600 ^{o}C confirm that the residues were eliminated up to 600 ºC and prove that SiCa-tt600 sample is well stabilized and shows no thermal events. The SiCa-EtOH sample presents very similar thermogram as the calcined xerogel.

The X-ray diffraction analysis (Fig. 2) indicate that both stabilization routes preserve the amorphous character of the samples and no diffraction peaks assigned to crystalline phase development occur beside the broad line recorded between 15º and 38º (2θ).

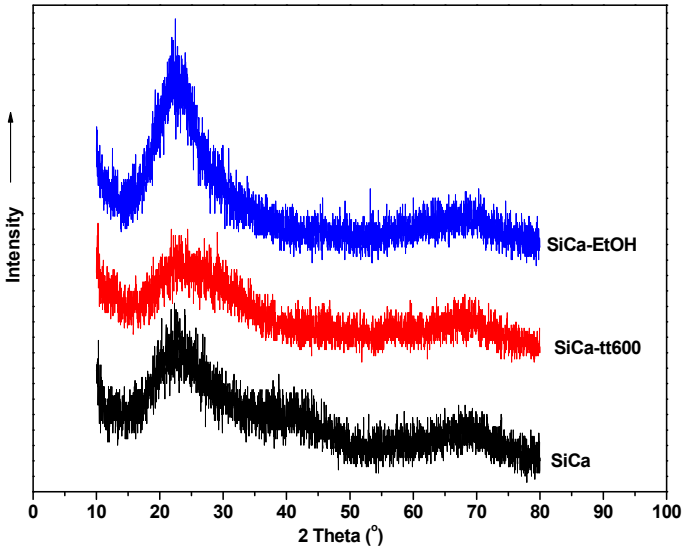

Fig. 2. XRD patterns for the investigated samples.

FTIR spectra (Fig. 3) of all three samples contain vibration bands characteristic for silicate samples. In case of the as prepared sample can be noticed absorption peaks at 1097 cm^{-1} and 461 cm^{-1} corresponding to Si-O-Si stretching and bending vibrations and at 820 cm^{-1} corresponding to O-Si-O stretching vibration. The shoulder located around 1227 cm^{-1} can be attributed to Si-O-Si stretching vibration [10]. The calcium presence as modifier in the Si-O-Si network is confirmed by the absorption band located around 978 cm^{-1}, associated with the nonbonding oxygen atoms [11]. Characteristic peaks for residually nitrate groups and adsorbed water are also present. The absorption band located around 1380 cm^{-1} is attributed to NO_3^- stretching vibrations and the band from 3445 cm^{-1} corresponds to OH bonds. The molecular water is highlighted by the sharp peak from 1634 cm^{-1} [5]. The samples stability is confirmed by the fact that the spectra of SiCa-tt600 and SiCa-EtOH, present just the absorption bands characteristic to silicate glasses. It can be observed the decrease of the vibration bands given by nitrate groups in both thermally treated and alcohol repeatedly immersed samples.

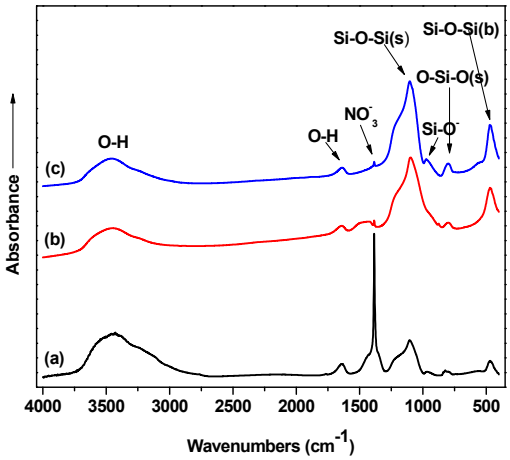

Fig. 3. FTIR spectra for as prepared SiCa (a), thermally treated SiCa-tt600 (b) and alcohol immersed SiCa-EtOH(c) samples.

As revealed by SEM images (Fig. 4), the morphology of dried, calcinated and alcohol repeatedly immersed particles is slightly different. Particles of SiCa have a more flake like appearance, while SiCa-tt600 seems to have a dense texture covered by flakes of smaller particles, and SiCa-EtOH appears to be the most uniform, this powder being formed by agglomerated small spherical particles.

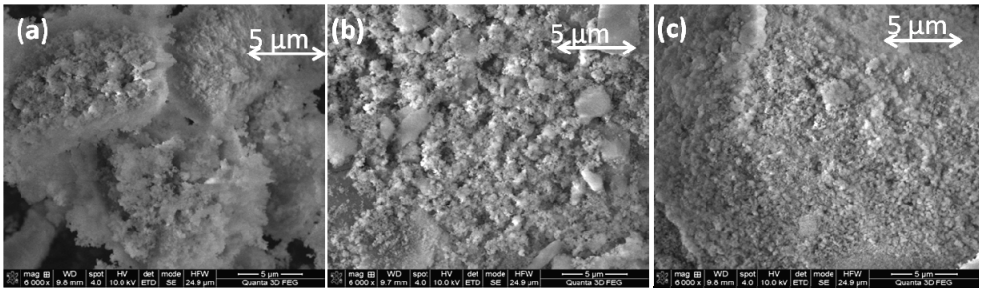

Fig. 4. SEM micrographs for as prepared SiCa (a), thermal treated SiCa-tt600 (b) and alcohol immersed SiCa-EtOH (c) samples.

Specific surface area and total pore volume of the three samples were measured and the values are summarized in Table 1. Samples were degassed at 100°C for a period of 30 min. The as prepared sample presents the lowest surface area because of the residual pore liquor. The specific surface area of the as prepared sample is almost doubled after calcination but is still small if is compared with the specific surface area of the ethanol stabilized sample, fact that may be due to the pore collapse occurred during the calcination process. The ethanol stabilized sample

presents a higher specific surface area because the surface tension of ethanol is lower than the one of the water.

Table 1. BET results on surface area and pore volume

Sample	Surface area (m^2/g)	Pore volume (ml/g)
SiCa-dried	49.5000	0.2655
SiCa-tt600ºC	82.6923	0.5394
SiCa-EtOH	206.9767	0.8381

CONCLUSIONS

SiO_2-CaO samples were prepared via alkali mediated sol-gel technique. According to the thermal behaviour of the samples evaluated from thermal analysis, the sample heat treated at 600ºC for one hour can be compared with the sample stabilized by alcohol repeated immersion because there were no significant differences regarding their structural properties. The samples remain amorphous both after stabilization by 600ºC calcination and after stabilization by repeated immersion in ethanol. The SEM and BET results indicate that the alcohol stabilization method leads to more uniform particles and higher specific surface area than that achieved after stabilization by the conventional calcination method.

REFERENCES

[1] L.L. Hench, R.J. Splinter, W.C. Allen, T.K. Greenlee, *J. Biomed. Mater. Res.,* 2, 117 (1971).

[2] W. Xia, J. Chang, *Mater. Lett.*, 61, 3251 (2007).

[3] P. Sepulveda, J.R. Jones, L.L. Hench, *J. Biomed. Mater. Res*., 61, 301 (2002).

[4] M.I. El-Gohary, K.M. Tohamy, M.M. El-Okr, A.F. Ali, I.E. Soliman, *Nat. Sci.*, 11, 26 (2013)

[5] L.M. Mukundan, R. Nirmal, D. Vaikkath, P.D. Nair, *Biomatter,* 3, e24288; April/May/June (2013)

[6] I.D. Xynos, A.J. Edgard, L.D.K. Buttery, L.L. Hench, J.M. Polak, *J. Biomed. Mater. Res.,* 55, 151 (2001).

[7] I.D. Xynos, A.J. Edgard, L.D.K. Buttery, L.L. Hench, J.M. Polak, *Biochem. Biophys. Res. Commun*., 276, 461 (2000).

[8] W.M. Jones, D.B. Fischbach, *J. Non-Cryst. Solids*, 101, 123 (1988).

[9] C. Wu, J. Chang, J. Wang, S. Ni, W. Zhai, *Biomaterials,* 26, 2925 (2005).

[10] H.S. Costa, M.F. Rocha , G.I. Andrade, E.F. Barbosa-Stancioli, M.M. Pereira, R.L. Orefice, W.L. Vasconcelos, H.S. Mansur, *J. Mater. Sci.*, 43, 494 (2008).

[11] A. Meiszterics, K. Sinko, *Colloid Surfac A,* 319, 143 (2008).

STUDIA UBB PHYSICA, Vol. 58 (LVIII), 1, 2013, pp. 33-39
(RECOMMENDED CITATION)

SYNTHESIS AND CHARACTERIZATION OF A NOVEL COPPER DOPED SiO_2–P_2O_5–B_2O_3-CaO–Na_2O GLASS CERAMIC

V. SIMON[a,*], D. TRANDAFIR[a], G. GOLLER[b]

ABSTRACT. Novel SiO_2–P_2O_5–B_2O_3- CaO–Na_2O glass ceramics doped with copper were obtained by melting method by room temperature cooling with different cooling rates. The samples contain hydroxyapatite and wollastonite crystalline phases desirable for bioactive ceramics. They were characterised by X-ray diffraction, scanning electron microscopy, infrared and electron paramagnetic resonance spectroscopies.

Keywords*: bioceramics; copper doping; cooling rate.*

INTRODUCTION

In the orthopedic surgery bone defects frequently require filler materials to repair bone loss. Autologous bone is currently regarded as the optimal material for such defects. However, autografts are limited available, and therefore frozen or freeze-dried allogenic bones are alternative bone substitutes, but they also associate problems. Due to the problems reported with respect to xenografts, their use is increasingly giving up. In these conditions, man-made materials with osteoconductive properties attracted increasing interest and ceramics are promising candidates as novel orthopedic materials to promote bone regeneration [1]. A large number of bioactive glass ceramics were prepared and tested as bone graft substitutes.

CaO-SiO_2-P_2O_5-B_2O_3 glass ceramics show no adverse toxic effects [2], directly bond to bone and have potential use as a bone substitute material [3].

Such ceramics were also considered for surface coating of metallic implants because they improve the bone bonding strength of the implant [4]. On the other hand, the applications of these materials are limited due to the relatively high processing temperatures needed for glass-melting and/or devitrification.

[a] Babes-Bolyai University, Faculty of Physics & Institute of Interdisciplinary Research in Bio-Nano-Sciences, 400084 Cluj-Napoca, Romania

[b] Istanbul Technical University, Department of Metallurgical and Materials Engineering, 34469 Istanbul, Turkey

* Corresponding author: viorica.simon@phys.ubbcluj.ro

The properties of these glass ceramics depend on both their chemical compositions and sintering temperatures [3] and the crystalline phases formed during heat treatment depend on the structural units of the parent glass.

Angiogenesis represents an important process during the formation and repair of new tissue. Inorganic angiogenic factors, such as copper ions, are therefore of interest in the field of regenerative medicine and tissue engineering [5].

The present study aimed to develop and characterise the morphology, surface composition and local structure of a SiO2–P2O5–B2O3- CaO–Na2O glass ceramic obtained from melt derived samples subjected to different cooling rates.

EXPERIMENTAL

High purity SiO_2, H_3BO_3, $(NH_4)_2PO_4$,$CaCO_3$, Na_2CO_3 and CuO reagents were used as precursors for melt derived $44SiO_2 \cdot 5P_2O_5 \cdot 20B_2O_3 \cdot 20CaO \cdot 10Na_2O \cdot 1CuO$ (mol %) glass ceramics. The mixtures of precursors introduced in amounts corresponding to this composition were melted at 1350 ^oC, for 30 minutes, and cooled to room temperature in about 3 minutes (sample *a*) and 30 minutes (sample *b*).

The structure of the resulting samples were analysed by X-ray diffraction with a Shimadzu XRD – 6000 diffractometer using Cu Kα (λ= 1.5405 Å) radiation. The morphology and elemental composition on the surface of the samples were analysed by scanning electron microscopy (SEM) and electron dispersive spectroscopy (EDS) using a JEOL JSM 7000F Scanning Electron Microscope.

The FTIR spectra were recorded with a resolution of 2 cm^{-1} on a Bruker spectrophotometer at room temperature using the KBr disk technique. Electron paramagnetic resonance spectra were recorded on powder samples at room temperature in X band, with 4 G modulation amplitude, on an ADANI spectrometer.

RESULTS AND DISCUSSION

The X-ray diffraction patterns over the range 2 theta 5–80^o (Fig. 1) show the influence of the cooling rate on the partial crystallisation of the samples. Beside the vitreous phase are identified hydroxyapatite, $Ca_5(PO_4)_3(OH)$, and beta-wollastonite, β-$CaSiO_3$, type crystalline phases [6, 7], and wollastonite is developed to a higher extend in the sample cooled down slowlier (sample *b*).

The presence of both hydroxyapatite and wollsatonite is desirable for bioactive materials considered for scaffolds for bone tissue engineering [3].

For glasses of somehow apropriate compositions in Na_2O-K_2O-MgO-CaO-B_2O_3-P_2O_5-SiO_2 system it was reported that the tendency to devitrification is important for their bioactivity [8].

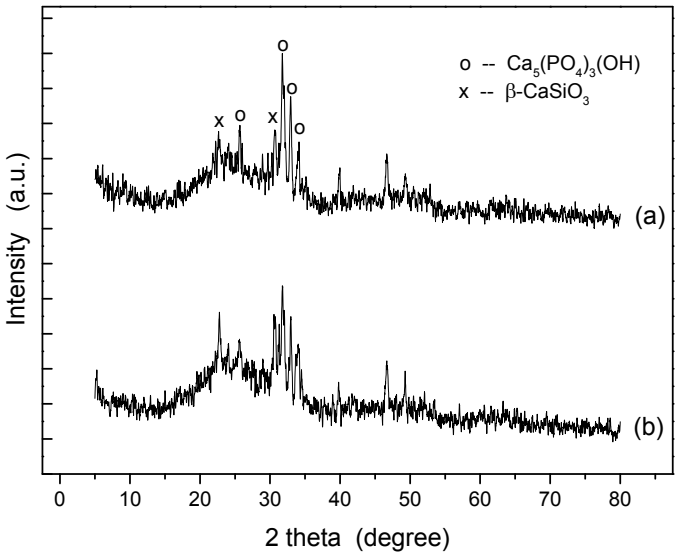

Fig. 1. XRD patterns of melt derived samples cooled to room temperature in 3 min (a) and in 30 min (b).

SEM images recorded from the differently cooled samples (Fig. 2) indicate for longer cooling time an extension of the separated phases. The elemental composition (Table 1) mainly differ with respect to calcium content that could be related to enhanced development of wollastonite for longer cooling time, as evidenced also by XRD results.

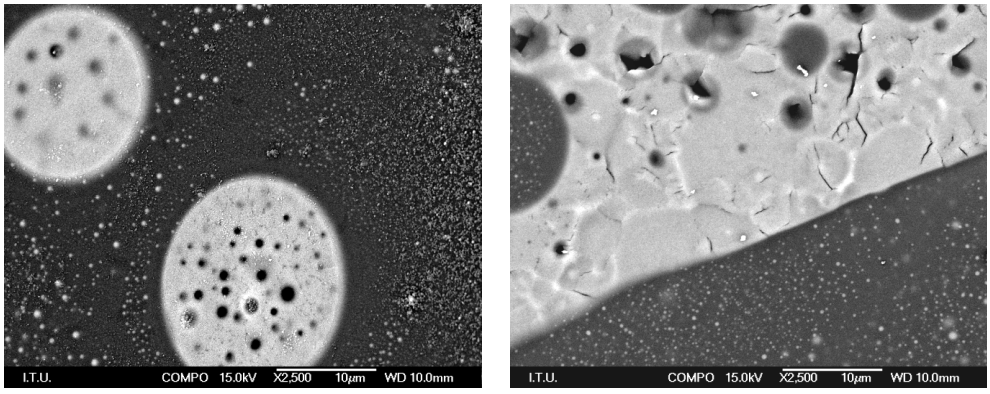

(a) **(b)**

Fig. 2. Back-scattered electrons SEM images of melt derived samples cooled to room temperature in 3 min (a) and in 30 min (b).

Table 1. Elemental composition (at %) determined by electron dispersive spectroscopy

Elements→ Sample↓	B	O	Na	Si	P	Ca	Cu
(a)	11.48	65.19	3.98	12.81	2.52	3.79	0.23
(b)	10.77	62.42	2.75	11.23	2.64	9.83	0.36

The FTIR spectra consist of absorption bands centered at 467, 565, 603, 695, 777, 1050 and 1414 cm^{-1} (Fig. 3). In the spectral range of interest, usualy investigated up to 1500 cm^{-1}, these infrared bands can be assigned to structural units related to the three glass network formes, i.e. SiO_2, B_2O_3 and P_2O_5 (Table 2).

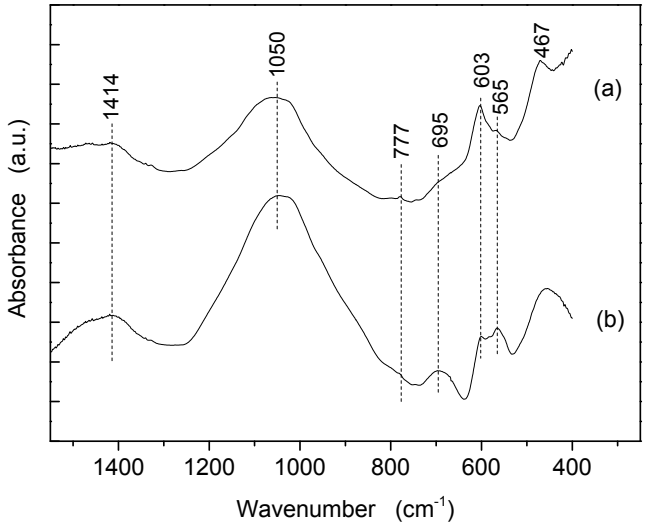

Fig. 3. FTIR spectra of melt derived samples cooled to room temperature in 3 min (a) and in 30 min (b).

Table 2. Assignment of infrared absorption bands [9-14].

Glass network	Vibrational mode	Wavenumber (cm^{-1})
Silicates	Asymmetric stretch vibrations of $Si–O^-$ bonds in Q^3 tetrahedral units	1075
	Asymmetric stretch vibrations of $Si–O^-$ bonds in Q^2 tetrahedral units	950
	Asymmetric stretch vibrations of $Si–O^-$ bonds in Q^1 tetrahedral units	900

Glass network	Vibrational mode	Wavenumber (cm^{-1})
	Rocking motion of Si–O–Si bridges	400–550
	Bending vibrations of Si–O–Si bridges	780
Phosphates	Vibrations of the Q^2, Q^1 and Q^0 phosphate units	1400–400
Borates	B–O stretching of BO_3 units	1200–1450
	B– Ø stretching of $BØ_4$ units	850–1200
	B–Ø–B linkages of the borate network	700

The doublet at 565 and 603 cm^{-1} is typical for hydroxyapatite [15]. Infrared vibration bands, predominantly Q^2 and Q^3 silicate tetrahedral units, can be related to wollastonite crystalline phase. developed in the glass matrix, but also to combeite ($Na_2CaSi_2O_6$) that could nucleate in these samples [16]. The peaks at 695 and 775 cm^{-1} could be assigned to symmetric stretching of PØP Q^3, Q^2 and Q^1 units (650-800 cm^{-1}) [17].

The disposal of copper ions in these materials was investigated by electron paramagneric resonance of Cu^{2+} ions. The EPR signals delivered by Cu^{2+} ions (Fig. 4) denote similar vecinities of copper dopped in SiO2 P2O5 B2O3 CaO Na2O matrix. The difference in signal intensity is due to a higher number of Cu2+ ions in the sample cooled with lower cooling rate.

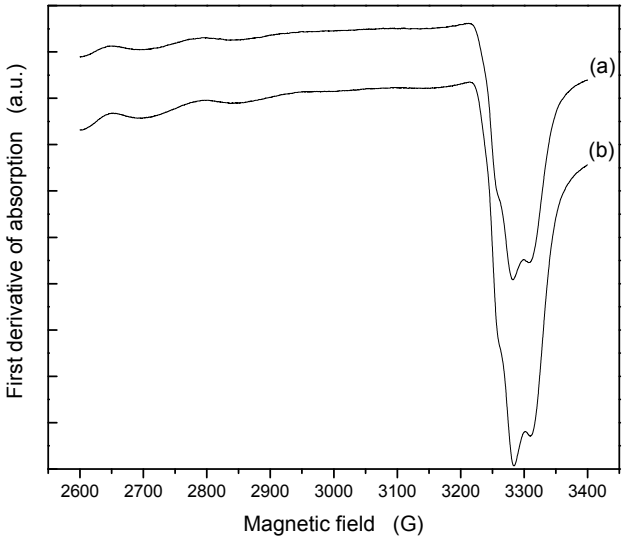

Fig. 4. X-band first derivative curves of the EPR absorption of melt derived samples cooled to room temperature in 3 min (a) and in 30 min (b).

The spectrum shows hyperfine structure due to the interaction of Cu^{2+} unpaired electron spin with the nuclear spin. The hyperfine structure is resolved in both parallel and perpendicular bands. Cu^{2+} resonant centers are disposed in an elongated octahedron vicinity, with rhombic symmetry [18] and experience an orthorhombic crystalline field.

CONCLUSIONS

New melt derived SiO_2–P_2O_5–B_2O_3-CaO–Na_2O glass ceramics doped with copper were obtained by fast and slow cooling to room temperature. Beside the vitreous phase, crystalline phases of hydroxyapatite and β-wollastonite type resulted in boths samples. Wollastonite is developed to a higher extend in the sample cooled down slowlier, and in this sample could also growth combeite. All these crystalline phases are expected to enhance the bioactivity of the compounds. The vecinity of copper ions introduced as angiogenic factors has an elongated-octahedral geometry and copper ions experience an orthorhombic crystalline field.

ACKNOWLEDGEMENTS

This research was accomplished in framework of PNII PCCE-248/2008 project granted by Romanian National University Research Council.

REFERENCES

1. H. Liu, T.J. Webster, Ceramic/polymer nanocomposites with tunable drug delivery capability at specific disease sites, *J. Biomed. Mater. Res*. (2010) 93A, 1180–1192.
2. J.H. Lee, H.S. Ryu, J.H. Seo, B.S. Chang, C.K. Lee, A 90-day intravenous administration toxicity study of CaO-SiO_2-P_2O_5-B_2O_3 glass-ceramics (BGS-7) in rat, *Drug Chem. Toxicol*. (2010) 33, 38-47.
3. X. Yang, L. Zhang, X. Chen, X. Sun, G. Yang, X. Guo, H. Yang, C. Gao, Z. Gou, Incorporation of B_2O_3 in CaO-SiO_2-P_2O_5 bioactive glass system for improving strength of low-temperature co-fired porous glass ceramics, *J. Non-Cryst. Solids* (2012) 358, 1171–1179.
4. J.H. Lee, K. S. Hong, H.-R. Baek, J.-H. Seo, K.M. Lee, H.-S. Ryu, H.-K. Lee In vivo evaluation of CaO-SiO_2-P_2O_5-B_2O_3 glass-ceramics coating on Steinman pins, *Artif. Organs* DOI: 10.1111/aor.12040.
5. M.M. Erol, V. Mourino, P. Newby, X. Chatzistavrou, J.A. Roether, L. Hupa, Aldo R. Boccaccini, Copper-releasing, boron-containing bioactive glass-based scaffolds coated with alginate for bone tissue engineering, *Acta Biomater*. (2012) 8, 792–801.

6. D.U. Tulyaganov, S. Agathopoulos, J.M. Ventura, M.A. Karakassides, O. Fabrichnaya, J.M.F. Ferreira, Synthesis of glass–ceramics in the CaO–MgO–SiO_2 system with B_2O_3, P_2O_5, Na_2O and CaF_2 additives, *J. Eur. Ceram. Soc.* (2006) 26, 1463–1471.

7. L.-C. Gerhardt, A.R. Boccaccini, Bioactive glass and glass-ceramic scaffolds for bone tissue engineering, *Materials* (2010) *3*, 3867-3910.

8. H. Arstila, E. Vedel, L. Hupa, M. Hupa, Predicting physical and chemical properties of bioactive glasses from chemical composition. Part 2: Devitrification characteristics, *Glass Technol.: Eur. J. Glass Sci. Technol. Part A* (2008) 49, 260-265.

9. F. Domine, B. Piriou, Study of sodium-silicate melt and glass by infrared reflectance spectroscopy, *J. Non-Cryst. Solids* (1983) 55, 125–130.

10. G. Lucovsky, C.K. Wong, W.B. Pollard, Vibrational properties of glasses intermediate range order, *J. Non-Cryst. Solids* (1983) 59, 839–846.

11. R.K. Brow, D.R. Tallant, S.T. Myers, C.C. Phifer, The short-range structure of zinc polyphosphate glass, *J. Non-Cryst. Solids* (1995) 191, 45–55.

12. H.S. Liu, T.S. Chin, S.W. Yung, FTIR and XPS studies of low-melting PbO–ZnO–P2O5 glasses, *Mater. Chem. Phys*. (1997) 50, 1–10.

13. J.J. Hudgens, S.W. Martin, Glass-transition and infrared-spectra of low-alkali, anhydrous lithium phosphate-glasses, *J. Am. Ceram. Soc*. (1993) 76, 1691–1696.

14. E.I. Kamitsos, M.A. Karakassides, G.D. Chryssikos, A vibrational study of lithium borate glasses with high Li_2O content, *Phys. Chem. Glass*. (1987) 28, 203–209.

15. S. Agathopoulos, D.U. Tulyaganov, J.M.G. Ventura, S. Kannan, M.A. Karakassidesc, J.M.F. Ferreira, Formation of hydroxyapatite onto glasses of the CaO–MgO–SiO_2 system with B_2O_3, Na_2O, CaF_2 and P_2O_5 additives, *Biomaterials* (2006) 27, 1832–1840.

16. G.E. Stan, A.C. Popescu, I.N. Mihailescu, D.A. Marcov, R.C. Mustata, L.E. Sima, S.M. Petrescu, A. Ianculescu, R. Trusca, C.O. Morosanu, On the bioactivity of adherent bioglass thin films synthesized by magnetron sputtering techniques, *Thin Solid Films* (2010) 518, 5955–5964.

17. G. Socrates, Infrared and Raman Characteristic Group Frequencies - Tables and Charts, John Wiley & Sons LTD, 2004.

18. I. Ardelean, M. Peteanu, V. Simon, O. Cozar, F. Ciorcas, S. Lupsor, Structural and magnetic properties of CuO-TeO_2-B_2O_3-SrO glasses, *J. Magn. Magn. Mater*. (1999) 196, 253-254.

STUDIA UBB PHYSICA, Vol. 58 (LVIII), 1, 2013, pp. 41-48
(RECOMMENDED CITATION)

UV-VIS AND RAMAN OBSERVATION OF EFFECT OF GAMMA RADIATION ON THE PAA-TiO_2 MEMBRANES

T. STEFAN[a], C. LEORDEAN[a], L. DARABAN[a], M. TODICA[a,*]

ABSTRACT. The effect of gamma radiation on the physical properties of PAA-TiO_2 membranes was investigated by UV-VIS and Raman methods. Before irradiation the UV absorbance of samples increases with the concentration of TiO_2. Important modifications of this property appear after γ irradiation. Some modifications of the Raman spectra can be observed after irradiation.

Keywords: *PVA, TiO_2, gamma irradiation*.

INTRODUCTION

The Poly (acrylic acid) (PAA) is one of the polymers with possible applications in the pharmaceutical industry to the fabrication of the products designed for the skin treatment. These applications are dues to the high stability of this polymer, its compatibility with the biological tissues and its capability to include in its physical network pharmaceutical drugs, [1, 2]. During the therapy such products are exposed often voluntary or accidentally to UV irradiation, which can have undesired effects on the health of the patient. Providing a high protection against such radiation, especially in the domain 290 nm, is frequently requested to these products. In pure state PAA offers only a weak protection in this domain, but the addition TiO_2 enhances significantly this property. TiO_2 is an inorganic compound with high chemical stability in contact with the biological liquids, high refractive index, UV resistance, and antibacterial properties. The exposure to high dosed of gamma radiation is frequently used for sterilization, and sometime as method of therapy for skin diseases. Such high energy radiation can induce degradation of the polymeric matrix by ionization of the atoms, breaking of the molecular bonds or chain scission, followed by the modifications

[a] Babeş-Bolyai University, Faculty of Physics, 1 Kogălniceanu Str., 400084 Cluj-Napoca, Romania
* Corresponding author: mihai.todica@phys.ubbcluj.ro

of some physical properties like the UV-VIS transparence or cristallinity. Our interest was the observation of the possible modifications induced on microscopic scale by gamma radiations. These observations were done by UV-VIS and Raman spectroscopy on samples with different concentrations of TiO_2, before and after irradiation.

EXPERIMENTAL

The polymeric membranes were obtained from the aqueous gel of PAA. In solid state, before polymerization, PAA is a soluble polymer from which it is possible to obtain gels by dissolving the product in pure water. The gels were obtained by mixing 4 hours the polymer with distilled water at constant temperature 55^0 C until a homogeneous dispersion of the polymer is obtained. Then the TiO_2 was added in different weight concentrations 5%, 15%, 30%, and the components were mixed 3 hours at room temperature. Then the composition was displayed on a glass plates and kept 24 hours in dark, at room temperature, until the water evaporates. The gamma exposure was realized with ^{60}Co source with the flux 5.6 Gy/h, during different time intervals until the 1500 Gy dose was accumulated [3]. For all the samples the UV VIS investigation was done with Jasco V-670 system with scan speed 200 nm/min, UV VIS bandwidth 2 nm, and NIR bandwidth 8 nm. The Raman spectra were recorded with Witec CRM 200 confocal Raman microscope, at the room temperature. All Raman spectra were excited with 100 mW light produced by a He-Ne laser, 633 nm, and the spectra were recorded in backscattering geometry. A digital acquisition data is performed by the PC computer of the system.

RESULTS AND DISCUSSION

Before polymerization, the PAA is a white solid powder, which became transparent in gel state, before water evaporation. After evaporation of the water from the gel, the PAA membranes, in pure state, became almost white, keeping a good transparency for the visible light. For pure membranes the absorbance has very low value and remains almost constant in the wavelength range 800-300 nm, but increases in the domain 300-200 nm, with a maximum at 207 nm, (Fig. 1). The absolute value of absorbance is 0.1 a.u. at 800 nm and 0.21 a.u. at 300 nm, and 1.75 at 207 nm. Generally the polymers with single chemical bonds, like PAA or PVA (poly vinyl alcohol) absorb mainly the radiation in the far UV region (120-200 nm). The presence of the peak at 207 nm is most probable due to strong absorption of the polymer and to the existence of remaining water molecules trapped in the polymeric matrix after drying process of the membranes, [4-6]. Knowing the behavior of water in the UV domain, we can explain the increase of the absorption in the domain 350-200 nm by the existence of some amount of water in the PVA membranes.

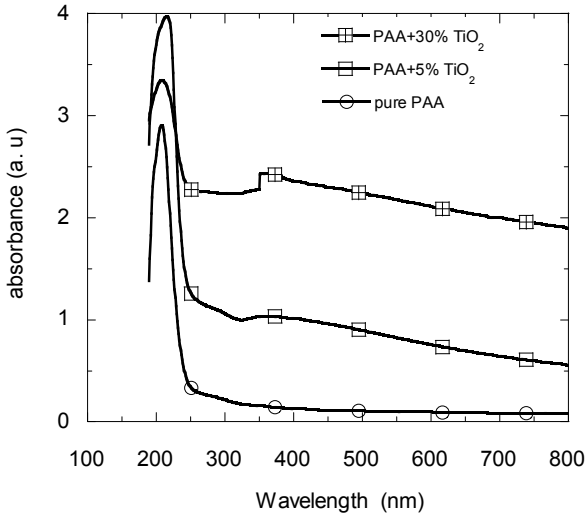

Fig. 1. The UV-VIS absorption spectra for the pure PAA membrane and membranes with 5% and 30% TiO_2 before irradiation.

The absorption in UV-VIS domain is enhanced by addition of TiO_2. The UV-VIS spectra of the composite membranes have the same shape as the pure PAA membranes, without supplementary absorption peaks, but the absorbance increases continuously with the amount of TiO_2 in the whole domain UV-VIS (Fig 1). If the absorbance of pure membrane remains almost constant in the domain 800-300 nm, for the membranes with TiO_2 the absorbance increases slowly but continuously in this domain. For instance, at 5% TiO_2 concentration, the absorbance is 0.56 a.u. at 800 nm and 1.07 a.u. at 300 nm. For 30% TiO_2 concentration the absorbance is 1.9 a.u. at 800 nm and 2.25 a.u. at 300 nm. These values demonstrate the predominant role of the TiO_2 in the absorption in this domain. The peak at 207 nm can be seen again in the spectra of doped samples, but its amplitude relatively to the absorbance in the domain 800-300 nm decreases. For instance, in the case of pure membrane the amplitude of the peak is 2.92 a.u. compared with the average absorbance 0.12 a.u. in the domain 800-300 nm. At 30% TiO_2 concentration the amplitude of the peak is 3.36 a.u. compared with the average absorbance 0.86 a.u. in the domain 800-300 nm. From these data we can suppose that the total absorption of the samples is the result of addition of absorptions properties of the polymer and the TiO_2. The contribution of the TiO_2 is characterized by slow and monotonically increases in the whole domain 200-800 nm, whereas the absorption around the 207 nm is determined mainly by the polymer. So we can explain the relatively decrease of the amplitude of the peak at 207 nm compared to the absorption in the domain 600-300 nm when the concentration of TiO_2 increases. Similar effect was observed previously in the other systems, i.e. PVA - TiO_2, [7].

The absorption was measured for the pure PAA membrane and for the membranes with different concentrations of TiO_2 after gamma irradiation. For the pure PAA membrane, the UV absorbance decreases very slowly in the domain 300-800 nm (compared with the sample before irradiation), with more pronounced decrease of the amplitude of the peak at 207 nm, (Fig. 2). The possible explication is the breaking of hydrogen bonds between the neighboring chains and scission of the polymeric chains. Similar effect appears in PVA, which is a polymer with a chemical structure close to those of PAA [8]. For the membranes with TiO_2 the modification of the absorbance can be observed in the whole domain 200-800 nm. The absorption curves, before and after irradiation have the same shape, containing the absorption peak at 207 nm. The difference between the absorbance before and after irradiation increases with the increase of concentration of TiO_2. An illustrative example is shown in figure 2 for the sample with 30% TiO_2. A possible explanation is that TiO_2 weakness the polymeric network. It is included in the polymeric holes without chemical bonds with the polymer. In this way the hydrogen bonds between the polymeric chains are weakened and the gamma radiation can more easily produces scission of the chains. As shown before the scission of the chains is accompanied by the modification of the UV absorbance.

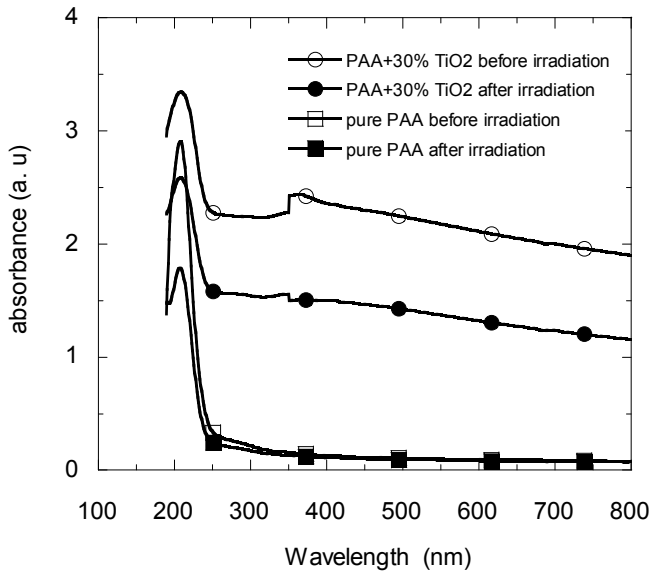

Fig. 2. The UV-VIS absorption spectra of pure PAA membrane and membranes content of 30% TiO_2, before and after irradiation.

The UV-VIS measurements suggest no chemical interaction between the polymer and TiO_2. In order to verify this supposition the samples were investigated by Raman spectroscopy. Every component, in pure state, is characterized by a well defined spectrum, which contains the characteristic vibration bands of the chemical bonds. When new chemical links appear between the components then some vibration bands of the individual component may change and new supplementary bands can occur [9]. If such modifications don't appear in the composite material, it means that no new chemical bonds appeared. In order to verfy these suppositions the Raman spectra were recorded before and after doping process. The Raman spectrum of pure PAA before irradiation is shown in figure 3. The most intense vibration bands of the polymer are assigned as follows, [10]: 500 cm^{-1} - CCO deformation; 822 cm^{-l} - CH_2 twisting; 1096 cm^{-1} - CH_2 in-plane rocking; 1461 cm^{-1} - CH_2 deformation; 1690 cm^{-1} - C=O stretching. These bands appear also in the membranes with TiO_2 without shift, but with lower intensity. In addition these spectra contain three supplementary bands at 399 cm^{-1}, 513 cm^{-1} and 639 cm^{-1}. The intensity of these bands increases progressively with the concentration of TiO_2, (Fig. 3). In accord with the data reported in literature in the domain 200-800 cm^{-1} TiO_2 exhibits three vibration bands at 400, 514 and 638 cm^{-1}, that correspond to the three phases of TiO_2, rutil, anatase and brooklite, [11]. These bands appear in ours spectra at the right wave number. The apparition of vibration bands of PAA and TiO_2 in the composite material at the same wave number as for the pure components suggests no apparition of chemical bonds between the polymer and the TiO_2. The chemical structure of both components remains unchanged in the composite material. After irradiation the spectrum of pure PAA membrane don't changes significantly. The characteristic bands of the polymer appear at the same wave number as before irradiation, theirs amplitudes increase slowly, but the general shape change. It behaves like the sample should contain some amount of water (Fig. 4). It is known that polymeric membranes obtained from aqueous gels contain water trapped in the holes of the polymeric matrix, which remains even after the draying process. Under gamma irradiation the polymeric matrix is perturbed allowing to the water to aggregate in domains with larger size than before irradiation. The changes of the shape of the Raman spectrum can be attributed to the contribution of water [6]. Similar behavior was observed on samples with TiO_2. The spectra contain the bands of polymer, at the same wave number as before irradiation and the three bands of the TiO_2. No shift was observed for these bands, but theirs amplitude increases after irradiation (Fig. 5). Also the shape of the spectrum change as for the pure membrane. That fact suggests again the possibility of modification of the polymeric matrix under irradiation. However the molecular structure of the polymer and of the TiO_2 are not affected, fact that results from the apparition of the vibration bands at the

same wave number before and after irradiation. At this dose of radiation the chemical structure of both the components of the samples are not affected, only the arrangements of polymeric chains in the network matrix is perturbed.

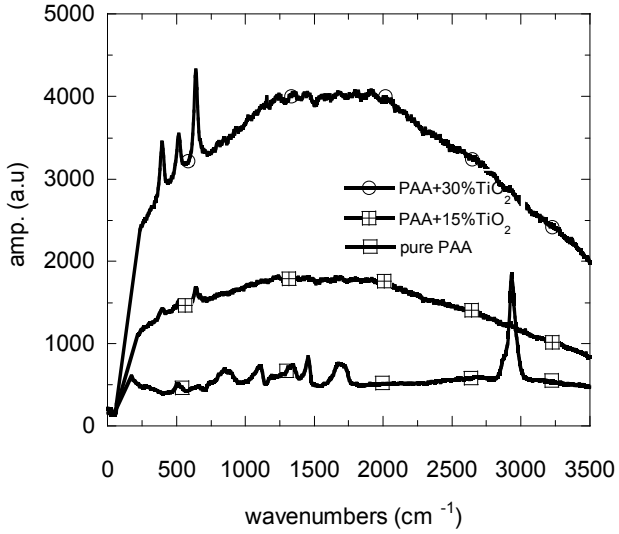

Fig. 3. The Raman spectra of pure PAA membrane and membranes with 15% and 30% TiO_2 before irradiation.

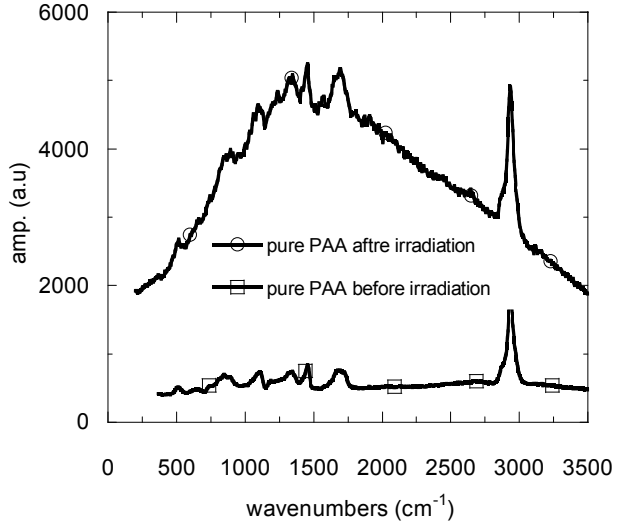

Fig. 4. The Raman spectra of pure PAA membrane before and after irradiation.

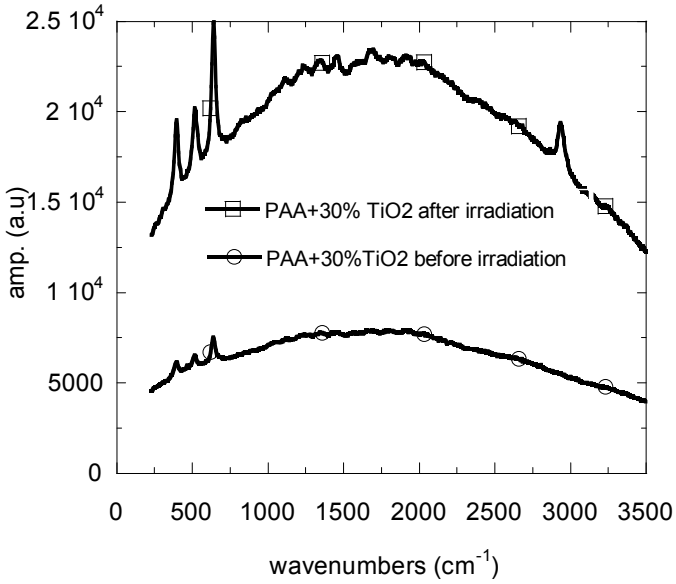

Fig. 5. The Raman spectra of PAA membranes with 30% TiO_2 before and after irradiation.

CONCLUSIONS

The UV-VIS absorbance of PAA-TiO_2 membranes, before irradiation, increases continuously with the concentration of TiO_2. This behavior is determined by the absorption property of the TiO_2 in the whole domain 200-800 nm. Modification of the absorbance of pure PAA membranes appears after gamma irradiation. This behavior is determined by the scission of the polymeric chain and modification of the polymeric network. More important modifications of the absorbance after gamma irradiation were observed for the PAA - TiO_2 membranes. The presence of TiO_2 in the polymeric matrix weakness the hydrogen bonds between the polymeric chains, fact that facilitates the scission of the chains under the gamma irradiation. The modifications induced by irradiations were confirmed by Raman spectroscopy.

ACKNOWLEDGMENTS

This work was developed on the framework: POSDRU/107/1.5/S/76841– Babes-Bolyai University, Cluj-Napoca, Romania, Ph.D. scholarship granted to Traian Stefan and CNCSIS-UEFISCU; project number PNII-IDEI ID_1157/2008

REFERENCES

1. Hoffman, A.S., *Adv. Drug Del. Rev.*, 2002*,* 43, 3
2. Sriamornsak, P. and Kennedy, R.A., *Int. J. Pharm.,* 2006, 323, 78
3. C. Ivascu, A. Gabor, O. Cozar, L. Daraban, I. Ardelean, *J. Mol. Struct*., 2011, 993, 1-3, 249
4. K.A.M. Abd El-Kader, S.F. Abdel Hamied, *J. Appl. Polym. Sci*., 2002, 86, 1219
5. R. Jayasekara, I. Harding, I. Bowater, G.B.Y. Christie, G.T. Lonergan, *Polym. Test.*, 2004, 23, 17
6. W.H. Eisa, Y.K. Abdel-Moneam, Y. Shaaban, A.A. Abdel-Fattah, A.M. Abou Zeid, *Mater. Chem. Phys.,* 2011, 128, 109
7. M. Todica, L. Udrescu, *Cent. Eur. J. Phys*., 2011, 9, 6
8. N.V. Bhat, M.M. Nate, M.B. Kurup, V.A. Bambole, S. Sabharwal, *Nucl. Instrum. Meth. B,* 2005, 237, 585
9. Barbara Stuart, "Polymer Analysis", 2003, John Wiley & Sons, Chichester
10. K. Itoh, M. Yaita, T. Hasegawa, S. Fujii and Y. Misono, *Journal of Electron Spectroscopy and Related Phenomena*, 1990, 54155, 9, 23-932
11. H.C. Choi, Y.M. Jung, S.B. Kim, *Vibrational Spectroscopy*, 2005, *37*, 33

STUDIA UBB PHYSICA, Vol. 58 (LVIII), 1, 2013, pp. 49-58
(RECOMMENDED CITATION)

STUDY OF MOBILITY HEMOGLOBIN SIDE CHAINS BY SPIN LABELED EPR SPECTROSCOPY

I.M. TAKÁCS[a], A. MOT[b], R. SILAGHI-DUMITRESCU[b] AND G. DAMIAN[a,*]

ABSTRACT. Site directed spin labeling studies of proteins have emerged over the recent years, in combination with EPR spectroscopy the technique allows the sample to be studies in its natural like environment. The article presents the results of the spin labeled Bos Taurus hemoglobin investigation under different environmental setups. The protein study was carried out to see the motional behavior and the dynamic conformational fluctuations in different viscous solvents, and a molecular crowding investigation was also carries out on the sample in order to obtain a full spectrum of the environmental impact on the spin labeled hemoglobin.

Keywords: *hemoglobin, EPR, site directed spin labeling, protein dynamics.*

INTRODUCTION

A specific property of proteins is that they adopt a large number of structural conformations in order to perform their role in the biological environment. The dynamical changes on proteins happens in the timeframe of mili and pico seconds. To be able to investigate these changes on this fast timescale the method of electron paramagnetic resonance (EPR) in combination with site directed spin labeling (SDSL) [1, 2, 3] is an appropriate way to investigate this conformational flexibility.

The technique of EPR in combination with site directed spin labeling allows the biomolecules to be studied in their native environment and offers the possibility to study proteins and nucleic acids without the limitations to the systems size or complexity [3, 4, 5, 6].

[a] "Babes-Bolyai" University, Faculty of Physics, 1 Kogălniceanu Str., 400084 Cluj-Napoca, Romania
[b] "Babes-Bolyai" University, Faculty of Chemistry and Chemical Engineering, 11 Arany János Str., 400028 Cluj-Napoca, Romania
* Corresponding author: grigore.damian@phys.ubbcluj.ro

Most of the proteins do not contain any free electron to be able to study with EPR spectroscopy, and this is where the site directed spin labeling comes in the picture. With this biological method through site directed mutagenesis an attachment point is created at a certain point in the proteins amino acid sequence, and a cysteine is inserted. Or if the amino acid sequence contains unwanted native cysteines they are to be replaced with an alanine or serine residue. With the attachment point created in the amino acid sequence, the cysteines thiol group is able to react, creating a covalent bond, with the functional group of the nitroxide spin label, containing the free electron for the EPR spectroscopy study. The nitroxide spin labels can be of a great variations, with different functional groups (methanethiosulfonate, maleimide and iodoacetamide). They contain a nitroxyl radical (N-O) incorporated in a heterocyclic ring with an unpaired electron on this bond. After they are covalently attached to the thiol group from the cysteine, they become attached to the protein and their motion is dominated by the motion of the molecule and the surrounding environmental changes, backbone fluctuations and rotary diffusion of the protein [7], with every change reflected in the EPR spectra [8, 9, 10].

In this study one of the most commonly used nitroxide spin label, 1-oxyl-2,2,5,5-tetramethylpyroline-3methyl or methanethiosulfonate spin label (MTSSL) [11], was used. Due to its relative small size 5-8Å and flexibility does not influence the protein backbone fluctuations, does not disturb the proteins overall folding, structure and functional properties [12].

With continuous wave EPR spectroscopy of the spin labeled protein we obtain information about the side chain mobility, environment polarity or even distance between a second paramagnetic center [8]. The free electron found on the N-O bond of the nitroxide spin label has a dipolar interaction with the nitrogen nucleus, I=1, the signal will be formed by three lines each resulting from the three quantum states of the nitrogen nucleus. The sensibility of the electron to the anisotropic environment will make the spin label sensible to the motion and this is reflected in the shape of the spectra by the increase or decrease in the intensity of the peaks and by the changes in the line width [4, 13]. The mobility of the side chain describes motional rate, anisotropy and reorientational motion of the nitroxide label [14]. The room temperature EPR spectra has a particular sensitivity to reorientational motion of the side chain due to the motional averaging of the anisotropic components of the g an hyperfine tensors [12, 15, 16].

This work presents the behavior of the spin labeled *Bos Taurus* (Bovine) hemoglobin (Hb) in different environment. This version of the oxygen carrier protein has a 2α2β tetrameric conformation, with two native cysteine per protein found in the beta subunit at the 92nd position slightly buried facing the core of the protein. Because of the native cysteine the protein can be spin labeled without performing any modification on its sequence. Typically linked to a cysteine residue in the hemoglobin through a disulphide bond is represented in Fig 1.

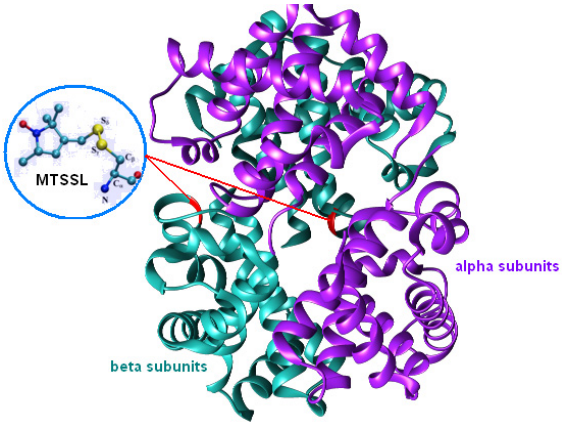

Fig. 1. Bos Taurus hemoglobin structure with cysteine positions marked with red.

EXPERIMENTAL DETAILES

The EPR measurements were carried out on a Bruker EMX EPR spectrometer with continuous wave at X-band (9 GHz), equipped with a Bruker liquid nitrogen temperature controller. The spectra were recorded at room temperature with a microwave frequency of 9.45 GHz, microwave power of 4 mW, modulation frequency of 100 kHz, modulation amplitude of 1 G and microwave attenuation of 17 dB. The samples were measured in quartz capillary tubes containing 15 µL of sample.

The MTS spin label was inquired from Enzo Life Sciences and was dissolved in DMSO (100 mM, stock solution).

Simulation of the EPR spectra of labeled proteins, was performed by Multi-Component EPR Fitting v2 version 495 program, a LabVIEW software, developed by Dr. Christian Altenbach (University of California, Los Angeles, California, https://sites.google.com/site/altenbach/labview-programs/epr-programs/multi-component) [17].

The *Bos Taurus* hemoglobin was suspended in PBS buffer and a final concentration of 10mM dithiothreitol (DTT) was added to the solution and incubated at 4^{o}C for 2 hours. The DTT was washed out from the sample using 10kDa Millipore filter in a Beckman J21B centrifuge, by centrifugation for 6 times at 4^{o}C, 5000 rpm for 30 minute. After removal of the dithiothreitol the MTS spin label was added in a 10 times excess to each cysteine and the sample was incubated for overnight. The removal of the excess unbound spin label was performed also with 10kDa Millipore filters at 5000rpm, 4^{o}C for 30 minutes 5 times. The obtained sample was checked for the spin labeling efficiency obtaining a result of 97%.

RESULTS AND DISCUSSIONS

The spin labeled hemoglobin will be abbreviated as Hb92R1, where the 92 part represents the position of the MTS spin label found at the 92nd position in the beta subunit and the R1 is the specific abbreviation for the MTS spin label after attached to the protein [18]. The protein recorded EPR spectra represented on the Fig. 2, was simulated with the previously mentioned software with a two component simulation, from the obtained simulated spectrum (Fig. 2) the EPR values were determined for the components separately for the room temperature and PBS buffered sample and represented in the Table 1. The values represented in the Table 1 represent the behavior and structure of the protein. The two components have a relatively slow rotational correlation time, larger than 3 ns, due to the bulky and tightly packed conformation of the protein. This mobility represented by these values are consistent with reality, they represent typical values for larger and compact proteins of the size of over 50kDa.

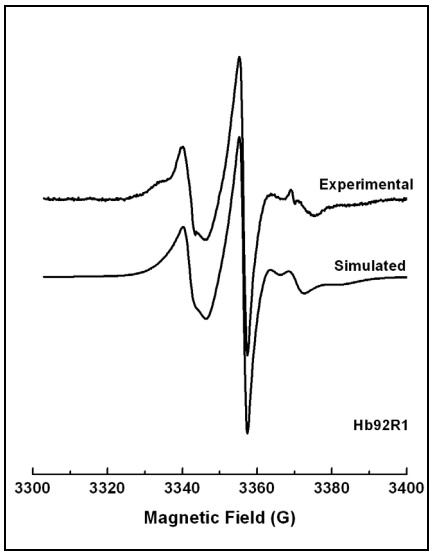

Fig. 2. Experimental and simulated EPR spectra of the spin labeled hemoglobin.

Table 1. EPR values obtained by simulation for the spin labeled hemoglobin.

	Comp. fraction (%)	Rotational correlation time, τ_c (ns)	Hyperfine tensor A values			g- tensor values		
			A_{xx}	A_{yy}	A_{zz}	g_{xx}	g_{yy}	g_{zz}
Comp. 1	21.21	3	9.83	10.13	33.68	2.00704	2.00504	2.00393
Comp. 2	78.79	4.73	5.9	6.2	34.76	2.00802	2.00602	2.00229

It is known that in an amount of biological sample the biomolecules interact with each other sometimes collide, take additional conformational states than they normally would. While also in the process of handling biological samples they undergo through a certain degradation when centrifuging, or pipeting. This is clearly sustained by the fact that the EPR spectra needed a minimum of two component for simulation to obtain a good fit. These components separately represent a conformational state in which the spin labeled hemoglobin is found in our sample.

The majority of the sample is represented by a slow component, 78.79% with a rotational correlation time of 4.73 ns, is the representative conformational state in the protein. This state stands for the whole assembly of the protein, with the spin label present facing to the core of the protein slightly buried in the helices.

The slightly faster component representing the 21.21% of the sample with a faster rotational correlation time of 3 ns, is overall more mobile than the majority of the sample. This conformational state would be the representation of the incomplete structures or the partially unfolded structure of the hemoglobin sample. These incomplete conformational structures contain at least one spin labeled beta globin subunit, since the spin label is found in this part we could not detect individual alpha globins in the sample.

A motional behavior study was effected on the spin labeled hemoglobin sample by introducing the protein in various environmental conditions varied with viscosity agents like glycerol and PEG-4000.

The PEG-4000 stands for polyethylene glycol, a polyether with the size of 4000 Da. The advantage of using this polyether in comparison with glycerol is that although glycerol has viscosity properties the PEG-4000 has a relative large size which can be compared with other biomolecules normally found in the native like environment of our sample. Also this way the result would somewhat mimic the collision and interactions between macromolecules undergoing in a everyday protein environment.

The experimental EPR spectra represented on the Fig. 3 for the glycerol experiment where the glycerol was varied in 0-85% w/w, obtaining an environmental viscosity range of 1.005-109 cPas shows the ideal environment of a protein where the motion is influenced by viscosity but no interactions are present between other molecules besides the protein. The motional restriction evolution can be seen on the spectra, the slow conformational state is adapting an even slower state and shifts to the left of the spectra while the faster conformational states intensity decreases and also experiences a shift to the left of the spectra.

The experiment with the polyether, PEG-4000, shows similar but different results in this case the molecular collisions of the spin labeled hemoglobin is present with the PEG-4000 molecules. The experimental EPR spectra, Fig. 4, also has visible motional evolution over the range of the 0-40% w/w concentration with a viscosity range of 1.005-29.412 cPas.

After performing the simulation of the experimental spectra of the spin labeled hemoglobin a graphical representation of the correlation time variation and the component fractions variations was done for the two type of solutions, glycerol and PEG-4000 and represented on the following graphs. Where Fig. 5 stands for the outcome of the experiment with glycerol and Fig. 6 stands for the experiment with the polyether.

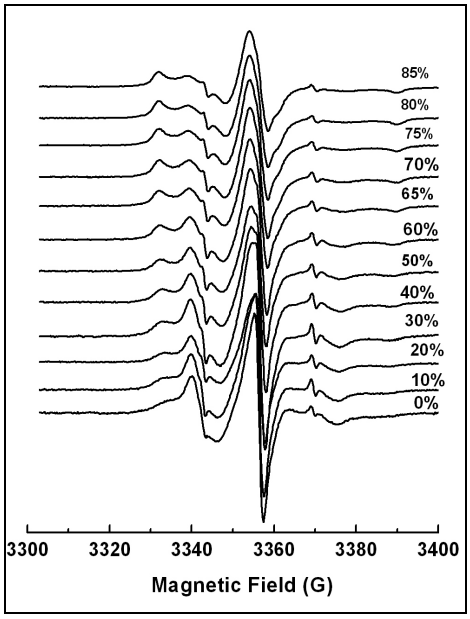

Fig. 3. EPR spectra of the spin labeled hemoglobin in glycerol solutions

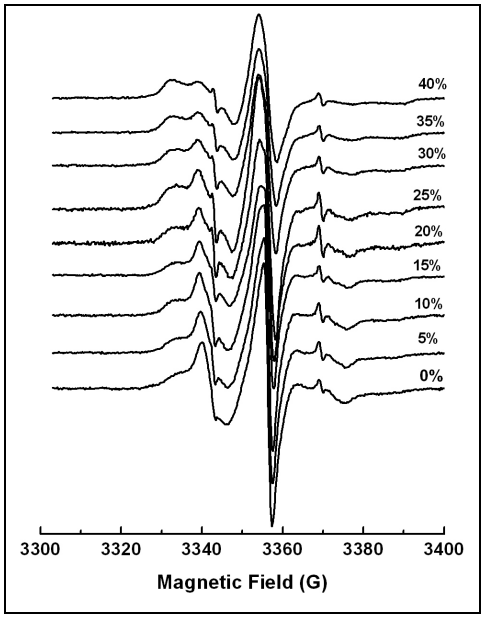

Fig. 4. EPR spectra of spin labeled hemoglobin in PEG-4000 solutions.

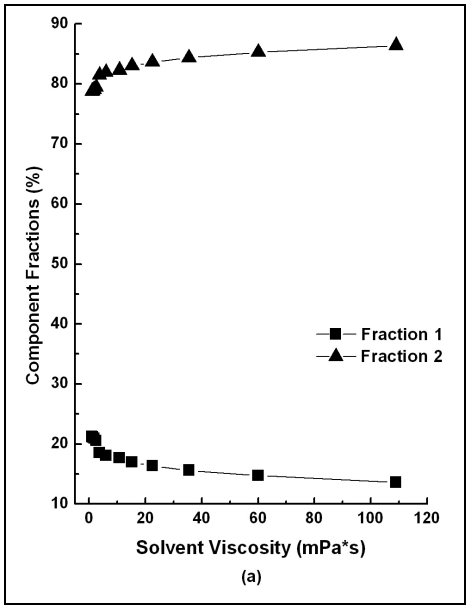

Fig. 5.a. Component fraction variation **b.** Correlation time variation in glycerol of the spin labeled hemoglobin.

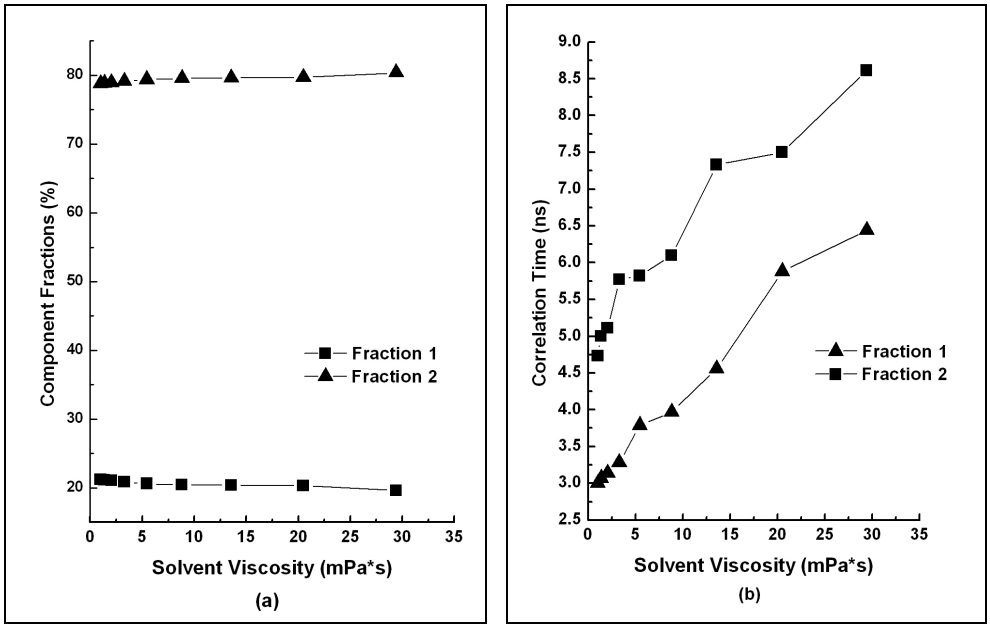

Fig. 6.a. Component fraction variation **b.** Correlation time variation of the spin labeled hemoglobin in PEG-4000.

The results for glycerol showed a variation of the faster conformational state fraction from 21.21% to 13.59% at a maximal viscosity of 109 mPas, while the rotational correlation time of this component changed from 3 ns to 6.15 ns.

The slower and tighter conformational state of the hemoglobin in glycerol solution showed a 78.79% to 86.41% rise with a rotational correlation time slow down from 4.73 ns to 9.45 ns.

While the small molecular sized glycerol showed the changes mentioned before the PEG-4000 due to its relative large size, nearly one fourth of a hemoglobin subunit, due to collisions and noticeable interactions with the spin labeled molecule induced only a 21.21% to 19.63% drop and a 3 ns to 6.44 ns slow down in the slightly faster conformational state.

Meanwhile the slower conformational state experienced a change in the component fraction from 78.79% to 80.37%, and an immobilization of this component happened from 4.73 ns to 8.61 ns of the rotational correlation time. The experienced change in the dynamics of the protein when the polyether is present is less than in case of glycerol, which is expected because, the relative large size of the PEG-4000 prevents the molecule to gain access to the site of the spin label inside the molecule and also the hemoglobin is tight and compact reduces the access of the viscous agent inside the molecule.

Although these agents are good candidates for a protein motional change study they don't cover the effect of the molecular crowding [19]. For this set of experiment additional non spin labeled BSA, bovine serum albumin, was introduced in the proteins environment in different amounts varying from 0-200 mg/ml. Although the experimental EPR spectra showed almost no visible changes when the albumin was present after the simulation process and the data analysis we found some variations in the proteins motional behavior.

A specific property of the serum albumin is the ability to stick to other proteins surface. We know that the rotational correlation time is also influenced by a proteins molecular size, with the size increasing when additional proteins attach to it the motion of the spin labeled hemoglobin is expected to decrease and slightly become immobilized, especially since the BSA has a size, 66.5 kDa, almost the same as the hemoglobin, 62,3 kDa. This expected theory is confirmed by the outcome and the results of this experiment. The graph representation of the component fractions variation, Fig. 7.a, and the representation of the correlation times, Fig. 7.b, shows a 78.79% to 81.91% increase of slow conformational state and a 4.73 ns to 5.34 ns change in this components rotational correlation time when the maximum amount of serum albumin was present, 200 mg/ml. While the faster conformation of the spin labeled sample experienced a change in the component fraction from 21.21% to 18.09% and an immobilization from 3 ns to 3.56 ns in its rotational correlation time.

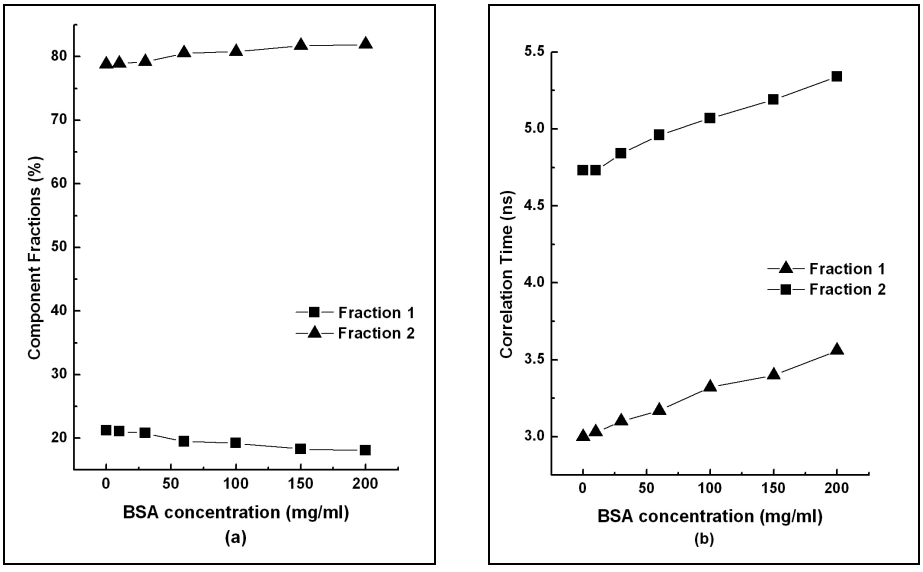

Fig. 7.a. Component fraction variation **b.** Correlation time variation in presence of BSA in the spin labeled hemoglobin sample.

CONCLUSIONS

This review on the mobility of the spin labeled hemoglobin in various viscous media and molecularly crowded environment provides excellent information about the behavior and characteristics of the attached spin label to the site of the protein. Not only the mobility is reflected but also conformational fluctuations are revealed also the sensitivity of the protein and the spin label to any environmental changes is revealed.

ACKNOWLEDGMENTS

I.M. Takács acknowledges the financial support of the Sectorial Operational Programme for Human Resources Development 2007-2013, co-financed by the European Social Fund, under the project number POSDRU/107/1.5/S/76841 with the title „*Modern Doctoral Studies: Internationalization and Interdisciplinarity*".

REFERENCES

1. C. Altenbach, S.L. Flitsch, H.G. Khorana, W.L. Hubbell, Structural studies on transmembrane proteins. 2. Spin labelling Bacteriorhodopsin mutants at unique cysteines, *Biochemistry*, 28, 7806-7812 (1989).
2. C. Altenbach, T. Marti, H.G. Khorana, W.L. Hubbell, Transmembrane protein structure: spin labelling of Bacteriorhodopsin mutants, *Science*, 248, 1088-1092 (1990).
3. E. Bordignon, H-J.Steinhoff, Membrane protein structure and dynamics studied by site-directed spin labelling ESR. In: M.A. Hemminga, L.J. Berliner (eds) ESR spectroscopy in membrane biophysics, Springer Science and Business Media, New York, 2007, pp 129-164.
4. W.L. Hubbell, H.S. Mchaourab, C. Altenbach, M.A. Lietzow, Watching proteins move using site-directed spin labelling, *Structure*, 4, 779-783 (1996)
5. W.L. Hubbell, A. Gross, R. Langen, M.A. Lietzow, Recent advances in site-directed spin labelling of proteins, *Curr. Opin. Struct. Biol.*, 8, 649-656 (1998).
6. C.S. Klug, J.B. Feix, Methods and applications of site-directed spin labelling EPR spectroscopy, In: J.J. Correia, H.W. Detrich (eds), Methods in cell biology. Biophysical tools for biologists, Volume one: in vitro techniques, Academic Press, New York, 2008, pp 617-658.
7. L. Columbus, W.L. Hubbell, A new spin on protein dynamics, *Trends Biochem. Sci.*, 27, 2856-2866 (2002).

8. G.F. White, L. Ottingnon, T. Georgiu, C. Kleanthous, G.R. Moore, A.J. Thomson, V.S. Oganesyan, Analysis of nitroxide spin label in protein-protein complex using multiple frequency EPR spectroscopy, *Journal of magnetic Resonance*, 185, 191-203 (2007).

9. S. Cavalu, G. Damian, Rotational correlation times of 3-carbamoyl-2,2,5,5-tetramethyl-3-pyrrolin-1-yloxy spin label with respect to heme and nonheme proteins, *Biomacromolecules*, 4(6),1630-1635 (2003).

10. S. Cavalu, G. Damian, M. Dansoreanu, EPR study of non-covalent spin labeled serum albumin and hemoglobin, *Biophysical Chemistry*, 99(2), 181-188 (2002).

11. L.J. Berliner, J. Grunwald, H.O. Hankovszky, K. Hideg, A novel reversible thiol-specific spin label: papain active site labelling and inhibition, *Anal. Biochem.*, 119, 450-455 (1982).

12. J.P. Klare, H-J. Steinhoff, Spin labelling EPR, *Photosynth. Res.*, 102 (2-3), 377-390 (2009).

13. H.S. Mchaourab, M.A. Lietzow, K. Hideg, W.L. Hubbell, Motion of spin-labeled side chains in T4 lysozyme. Correlation with proteins structure and dynamics, *Biochemestry*, 35, 7692-7704 (1996).

14. L.J. Berliner, Spin labeling: theory and applications, Academic Press, New York, 1976.

15. L.J. Berliner, Spin labeling II: theory and applications, Academic Press, New York, 1979.

16. L.J. Berliner, J. Reuben, Spin labeling theory and applications, Plenum Press, New York, 1989.

17. Multi-Component EPR Fitting v2 version 495 , LabVIEW software, developer Dr. Christian Altenbach, University of California, Los Angeles, California, https://sites.google.com/site/altenbach/labview-programs/epr-programs/multicomponent.

18. A. Czogalla, A. Pieciul, A. Jezierski, A.F. Sikorski, Attaching a spin to a protein – site directed spin labelling in structural biology, *Acta Biochemica Polonica*, 54 (2), 235-244 (2007).

19. R.J. Ellis, Macromolecular crowding: an important but neglected aspect of the intracellular environment, *Current Opinion in Structural Biology*, 11, 114-119 (2001).

STUDIA UBB PHYSICA, Vol. 58 (LVIII), 1, 2013, pp. 59-66
(RECOMMENDED CITATION)

MAGNETIC AND STRUCTURAL PROPERTIES OF SmCo PREPARED BY DC MAGNETRON SPUTTERING

A.F. TAKACS[a,*], C. PRAHOVEANU[a], ZS. SANDOR[a], M. ALBRECHT[b] AND V. POP[a]

ABSTRACT. The influence of thickness upon the magnetic and structural properties of Sm-Co films was studied. The films were deposited at room temperature by dc magnetron sputtering and annealed to achieve the SmCo phase formation. The highest value of the coercivity was 0.4 kOe, obtained for the 20 nm sputtered Sm-Co thin film sputtered from a $SmCo_5$ target after post-deposition annealing. Thickness growth of the sputtered Sm-Co layers did not have beneficial influence upon the coercive field of the samples. However the saturation magnetization of the samples increased with the thickness of the Sm-Co as well as with the annealing.

Keywords: *Thin films, Sputtering, Microstructure, Sm-Co, Underlayer*

I. INTRODUCTION

Nano-composite magnetic materials, amongst which thin films, play an important role in todays research as well as future applications due to their outstanding magnetic properties. Sm-Co thin film materials have been investigated for several years now for applications as permanent magnets, i.e. realization of micro-electromechanical systems (MEMS) [1, 2]. Their excellent intrinsic magnetic properties like moderate saturation magnetization, large magnetic anisotropy, and high Curie temperature make these materials a good candidate for based permanent magnetic thin films [3-6]. To obtain peculiar hard magnetic properties in these materials, a certain nano-structure must be obtained, hence aspects like size and shape of the crystalline grains as well as crystal orientation and their intergrain coupling must be well understood. High anisotropy field is one prerequisite for developing high coercivity. An approach that results in the largest perpendicular anisotropy is based on the growth of rare-

[a] "Babes-Bolyai" University, Faculty of Physics, 1 Kogălniceanu Str., 400084 Cluj-Napoca, Romania
[b] Chemnitz University of Technology, Institute of Physics, D-09107 Chemnitz, Germany
* Corresponding author: albert.takacs@phys.ubbcluj.ro

earth containing intermetallic films. If these are grown epitaxially, the combination of highest magnetocrystalline anisotropy with an optimum texture leads to the strongest magnetic anisotropy [7-9]. Depending on the composition and preparation conditions, various Sm-Co phases showing different anisotropy fields can be formed. J.J. Romero et al. and of E. Pinaa et al. [10, 11] reported that the SmCo samples deposited at room temperature (RT) on a Cr and Si substrate presented amorphous characteristics. In these studies the samples deposited at RT showed soft magnetic properties, with coercivity lower than 0.5 kOe, while the samples grown at 450 °C present a hard magnetic character with an in plane coercivity. A major requirement for obtaining these properties is to successfully deposit permanent magnetic films with controlled structural and microstructural properties. The characteristics of the magnetization reversal process of a hard magnetic film and the magnitude of its coercivity depend on both the intrinsic and extrinsic properties of the sample, thus in this paper we report the microstructure and magnetic properties of a series of Sm-Co thin films deposited by dc magnetron sputtering from a $SmCo_5$ target at room temperature (RT). Magnetocrystalline anisotropy, saturation magnetization and exchange correlation length are considered requisites for the development of the magnetic hardness. However, the actual coercive value is ruled by extrinsic features, starting with morphology and ending with the distribution of sites where the local values of the intrinsic properties depart from their bulk values. Therefore the influence of post-annealing on the coercivity (H_c) and magnetization (M) is studied in some detail.

II. EXPERIMENTAL

The Sm-Co thin films where prepared by sputter deposition from an $SmCo_5$ target. SmCo were deposited on a SiO_2(100 nm) / Si(*100*) coated with 20 nm thick Cu layer by means of dc magnetron sputtering at room temperature. The Cu seed layer gives excellent lattice-matching with the hexagonal Sm-Co, which orients the *c*-axis of the Sm-Co in the direction perpendicular to the film [12, 13]. Three different thicknesses for the Sm-Co film where deposited: 20, 40 and 60 nm in a base pressure of 3×10^{-7} mbar while the Ar pressure during sputtering was 1×10^{-3} mbar. The rates for deposition were 1.9 Å/s for Cu and 0.5 Å/s for Sm-Co layers and they were calibrated by means of reflectometry measurements. For each SmCo thin film obtained, a 5 nm cap layer was deposited from a pure solid Cu target (99.9 % purity) in order to protect the film from oxidation. Heat treatment (HT) was carried out for 5 minutes at 500 ºC for each sample in 10^{-5} mbar vacuum in order to induce crystallization and a hardening of their magnetic properties. The study of the structural properties was made by X-ray diffraction (XRD) on a Bruker D8 advance diffractometer using a Cr K_α radiation and the magnetic properties were investigated by using a SQUID magnetometer in magnetic field up to 70 kOe at RT.

III. RESULTS AND DISCUSSION

In Figure 1 are presented the XRD measurements for the as-deposited and heat treated 20 nm SmCo thin films. The diffraction lines from the Cu underlayer and SiO substrate were observed in each diffractograms (not highlighted here). Two distinct peaks belonging to the formation of Sm_2Co_{17} (*200*) can be observed on the first diffiractogram (Fig. 1 (a)), at 65,8 and 56,3 degrees *2 theta* values but no evidence of texture was found. After exposing the as deposited sample to a heat treatment at 500 °C for a period of 5 minutes the formation of the Sm_2Co_{17} (*200*) is enhanced, leading to the increase of its characteristic diffractogram peaks and the presence of a texture. Thus if in a crystallized sample [14] the peak ratio between 66.55, 65.97 and 55.27 peaks are 100/45 and 100/30 respectively, in the Sm-Co 20 nm the above peak ratios are 52/20 respectively 52/193 (Fig. 1 (b)). In samples with thicknesses of 40 nm and 60 nm we observe no crystalline formation in the as-deposited Sm-Co films while for the annealed counterparts we identify a slight formation of Sm_2Co_{17} as a main crystalline phase, thus it is more difficult to recover the crystallinity for Sm-Co 40 and 60 nm films by post-annealing processes (see Figure 2). The peaks corresponding to the Sm_2Co_{17} phase are not so clear evidenced like in the case of the Sm-Co 20 nm. We measured the in-plane and out-of-plane hysteresis loops of Sm-Co 20, 40 and 60 nm thicknesses. A field up to 70 kOe was used in order to saturate the magnetization of the Sm-Co thin films (Figure 3). After HT of the samples we observe that there is no important change in the in- and out-of-plane coercivity of 60 nm Sm-Co thin films. However for the sample with 20 nm Sm-Co thickness the in-plane coercivity increases with the annealed temperature, thus a better crystallinity is accompanied by an increase of Hc (Figure 4). For the HT 20 nm Sm-Co thickness out-of-plane hysteresis loop one can observe that the coercivity value is larger (0.4 kOe) than the in-plane coercivity thus indicating a perpendicular anisotropy (see Figure 4). The same tendency in the increase of the coercive field is observed for the 40 nm Sm-Co thin film where the measured out-of-plane coercivity for the HT case is 0.13 kOe (Figure 5). For the in-plane measurements we observed a peculiar dependence of the coercivity in the Sm-Co deposited films, (see Figure 4 and 5) the values ranging from 0.04 kOe up to 0.14 kOe indicating a slight increase, but nevertheless a poor coercivity with the increase of hard magnetic film thickness. The evolution of the in-plane coercivity filed in Sm-Co thin films both, as-deposited and HT, versus their thickness is given in Table 1. The increase up to 0.17 kOe for the 20nm Sm-Co film can be attributed to the formation of Sm_2Co_{17} phase, result that is in agreement with the XRD measurements. Contrary, for the samples with 40 respectively 60 nm the coercivity decreases with the annealing temperature. For the as-deposited Sm-Co films with 20 and 40 nm thicknesses we

have obtained the same coercive value (≈0.04 kOe), followed by an increase of the coercivity for the 60 nm Sm-Co thin film. After HT, the coercive in-plane values diminish for the thicker samples (40 and 60 nm films). Opposite to this, the coercivity of the in-plane annealed 20 nm sample increased more than four times from 0.04 kOe to 0.17 kOe. The coercivity evolution versus films thickness and annealing conditions is controlled by two parameters: the crystallinity and the internal stress in the thin films. Unlike for the case of Sm-Co 20 nm thin film where the Sm_2Co_{17} is formed, for the 40 and 60 nm thin films we observe a weak crystallization or phase formation after annealing. The in-plane saturation magnetization presents a continuous increase versus film thickness (see Figure 6). This behavior is given by the progressive increase of magnetic phase volume for thicker films. This ascendant trend of the magnetization is conserved with the HT for all the investigated samples. For the samples with 40 and 60 nm thicknesses the spontaneous magnetization increases by 50% after HT while for the 20 nm the increase is of 55 %. This higher increase in magnetization for the 20 nm sample could be explained by the better crystallization of this sample after annealing.

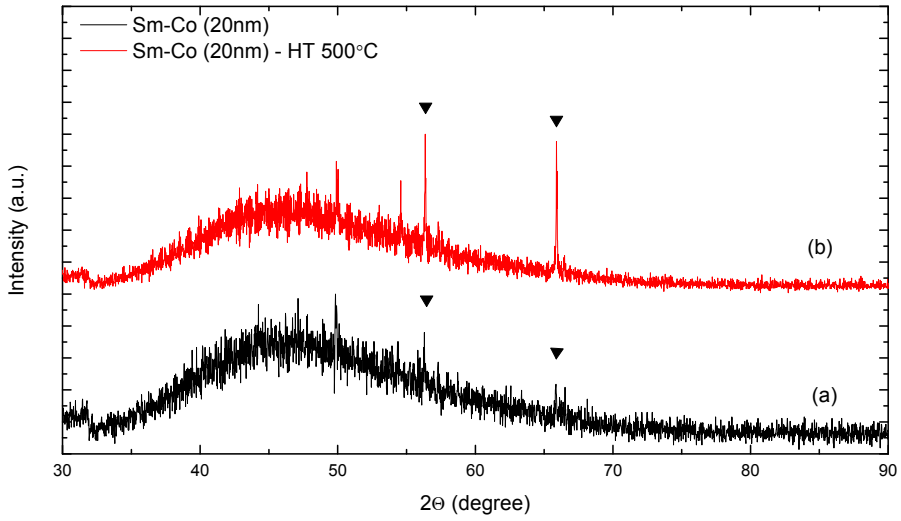

Fig. 1. Difractograms corresponding to the as-deposited (a) and heat treated (b), Sm-Co 20 nm thickness film

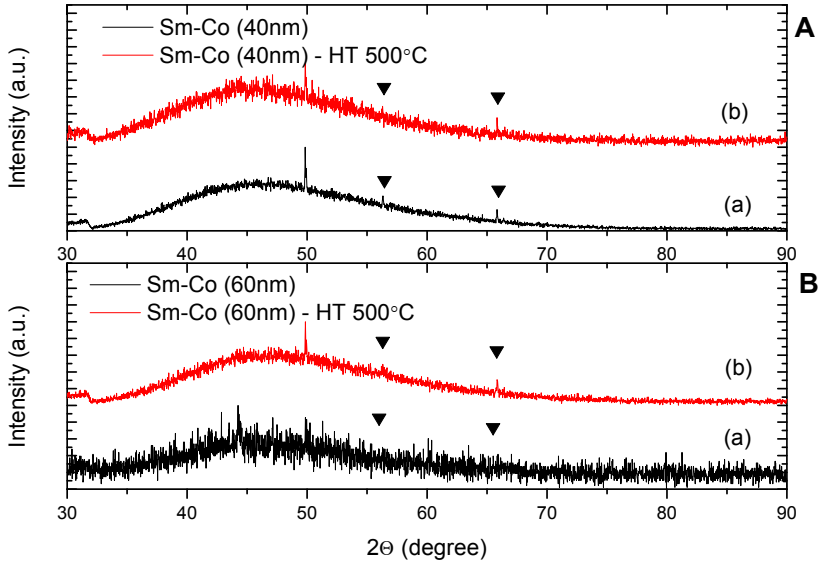

Fig. 2. Difractograms corresponding to the Sm-Co 40 nm thickness films **(A)** as –deposited and heat treated sample and Sm-Co 60 nm thickness films **(B)** as-deposited and heat treated sample

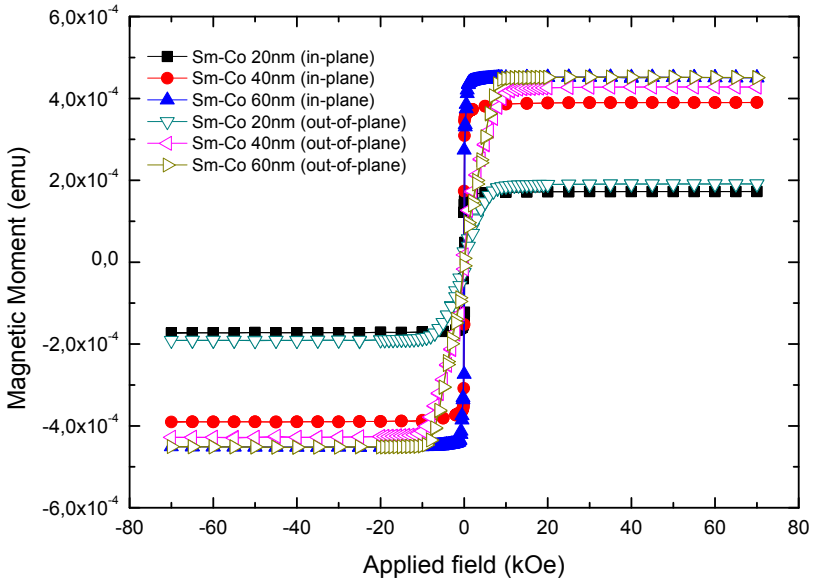

Fig. 3. RT in-plane and out-of-plane hysteresis loops recorded for the as-deposited 20, 40 and 60 nm Sm-Co films

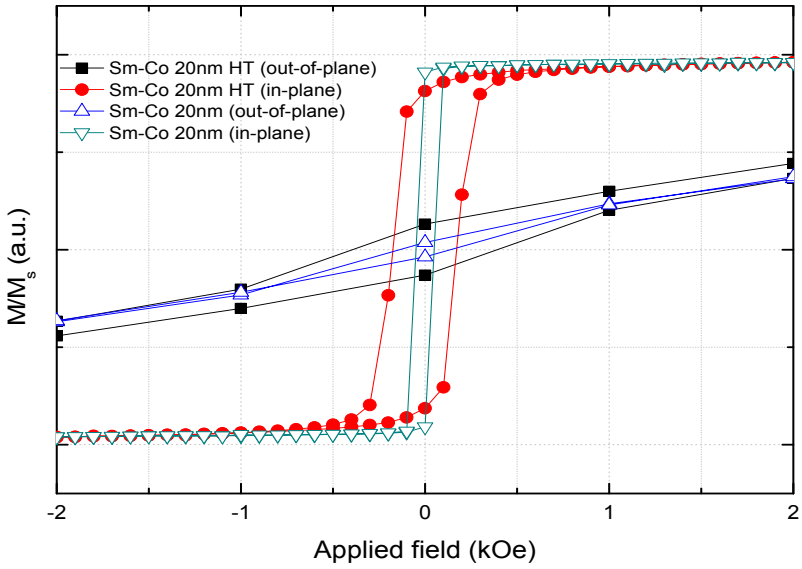

Fig. 4. RT in-plane and out-of-plane hysteresis loops recorded for the as-deposited and heat treated 20 nm Sm-Co films

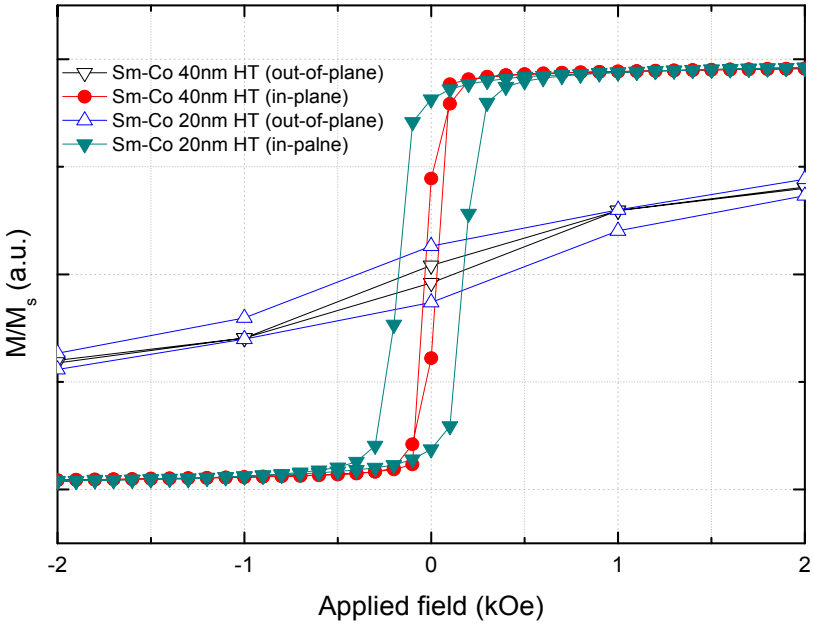

Fig. 5. RT in-plane and out-of-plane hysteresis loops recorded for the heat-treated 20 and 40 nm Sm-Co films

Table 1. H_c vs. Sm-Co thickness

Sm-Co thickness	$H_c \parallel / \perp$ (as-deposited)	$H_c \parallel / \perp$ (HT)
20 nm	0.04 / 0.13 kOe	0.17 / 0.40 kOe
40 nm	0.04 / 0.12 kOe	0.03 / 0.13 kOe
60 nm	0.14 / 0.12 kOe	0.11 / 0.09 kOe

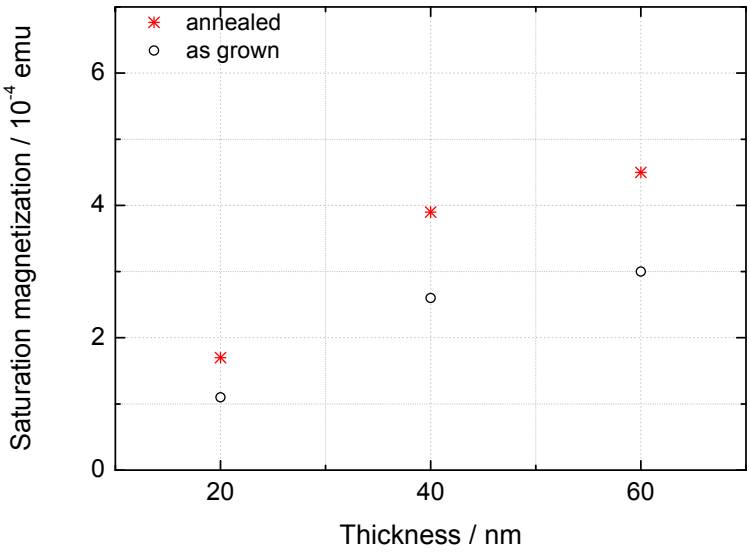

Fig. 6. Dependence of the in-plane saturation magnetization on the Sm-Co thicknesses

IV. CONCLUSIONS

This paper evidences the structural and magnetic behavior in function of the different thicknesses of Sm-Co thin films. In response to the structural transition, in films starting from 20 nm to 60 nm of Sm-Co, the saturation magnetization increases with the amount of Sm-Co, independent on the heat treatment conditions. The variation of coercivity depends also on the thickness on thin deposited films as well as on the heat treatment conditions. We have evidenced that for lower thicknesses of Sm-Co (20 nm) the coercivity is about three times larger for the heat treated sample than for the as-deposited ones, while for the higher thicknesses of Sm-Co (60 nm) there is no evident change in the coercivity depending on the heat treatment conditions.

ACKNOWLEDGEMENTS

This work was supported by a grant of the Romanian National Authority for Scientific Research, CNCS UEFISCDI, project number PN-II-RU-TE-2011-3-0048

REFERENCES

[1] D. Niarchos, *Sensors and Actuators A,* 109 166 173 (2003)

[2] P.A. Gilles, J. Delamare and O. Cugat, *J. Magn. Magn. Mater.*, 1186 242- 245 (2002)

[3] S. Takei, A. Morisako, M. Matsumoto, *J. Appl. Phys.,* 87 6968 (2000)

[4] V. Neu, S.A. Shaheen*, J. Appl. Phys*., 48 7006 (1999)

[5] H. Kromulle, D. Goll, *Scripta Materialia*, 48 833 (2003)

[6] A. Yan, A. Bollero, K.H. Muller, O. Gutfleisch, *J. Appl. Phys.,* 91 8825 (2000)

[7] M. Seifert, V. Neu, L. Schultz, *Appl. Phys. Lett*., 84, 022501 (2009)

[8] M. Weisheit, L. Schultz, S. Fahler*, J. Apply. Phys*., 95, 7489, (2004)

[9] T. Shima, K. Takanashi, Y.K. Takahasi, K. Hono, *Appl. Phys. Lett*., 85, 2571 (2004)

[10] J.J. Romero, F.J. Palomares, F. Pigazo, R. Cuado, F. Cebollada, A. Hernando, J.M. Gonzales*, J. Non-Cryst. Sol*., 353, 786-789, (8-10), (2007)

[11] E. Pinaa, F.J. Palomaresb, M.A. Garcia, F. Cebolladac, A. de Hoyosa*, J. Magn. Magn. Mater.,* 290-291 1234-1236 (2005)

[12] J. Sayama, T. Asahi, K. Mizutani, T. Osaka*, J. Phys. Appl. Phys*., 37 (2004) L1.

[13] S. Takei, A. Morisako, M. Matsumoto, *J. Magn. Magn.Mater*., 272-276 1703 (2004)

[14] Khan, *Acta Crystallorg. B,* 29 2502 (1973) .

STUDIA UBB PHYSICA, Vol. 58 (LVIII), 1, 2013, pp. 67-76
(RECOMMENDED CITATION)

PRELIMINARY STUDY REGARDING THE BIOCOMPATIBILITY OF SOME NEW BIOMATERIALS DESIGNED FOR SYNERGIC HYPERTHERMIA/RADIOTHERAPY APPLICATIONS

E. VANEA[a], C. GRUIAN[a], L. PĂTCAȘ[a], C.V. MORARU[a], V. SIMON[a,*]

ABSTRACT. Sol–gel derived $50SiO_2 \bullet 30CaO \bullet 10Fe_2O_3 \bullet 10Dy_2O_3$ and $50SiO_2 \bullet 28CaO \bullet 10Fe_2O_3 \bullet 10Dy_2O_3 \bullet 2ZnO$ (mol %) glass-ceramic samples were investigated with respect to bovine serum albumin (BSA) attachment for possible applications in internal radiotherapy and hyperthermia. The protein adsorption was evaluated on vitro-ceramic samples obtained by heat treatment at 800 ºC and 1200 ºC of sol-gel derived glass samples. After immersion in spin labeled BSA solutions, the Electron Paramagnetic Resonance (EPR) analysis shows a decrease in the amount of attached protein with the addition of ZnO and following the heat treatment at high temperature.

Keywords: *biomaterials; protein attachment; EPR.*

INTRODUCTION

Hyperthermia has gained a lot of interest recently as a method for cancer treatment especially in combination with procedures such as radiotherapy and chemotherapy. Simultaneous application of hyperthermia and radiation therapy improves the therapeutic effects of both cancer treatment procedures [1]. Bioactive glass ceramics containing iron and dysprosium are expected to be potential candidates for synergic hyperthermia and radiotherapy treatment of bone cancer. Hyperthermia is performed by generating the temperatures up to 43-45 °C by the magnetic particles introduced at the site of the cancerous tissue, when placed in an alternating magnetic field of high frequency [2]. Tumour cells die usually around 43-45 °C as a result of the underdeveloped blood circulation comparing the normal cells that resist up to 42 °C. On the other hand, systems containing radioactivable isotopes

[a] Babes-Bolyai University, Faculty of Physics & Institute of Interdisciplinary Research in Bio-Nano-Sciences, Cluj-Napoca, Romania
* Corresponding author: viorica.simon@phys.ubbcluj.ro

like yttrium and dysprosium [3-7] attracted interest for in situ radiotherapy since larger doses of radiation can be safety delivered to the target site and the exposure of the healthy tissue is considerably diminished.

Much work has been done on Fe_3O_4 containing glass ceramics due to their potential applications in hyperthermia treatment of cancer [6, 8-10]. The present work deals with bioactive glass ceramics containing a ferrimagnetic phase and radioactivable dysprosium for the purpose of potential cancer treatment by both hyperthermia and internal radiotherapy.

The interaction between the bioactive glass surface and the biological environment is a key factor in determining the biocompatibility of a biomaterial. Albumin represents the predominant plasma protein and the relevant biomolecule that adsorbed on the surface biomaterials that come in contact with blood. Albumin is considered to greatly reduce the acute inflammatory response to the biomaterial [11, 12]. The affinity to adsorb albumin appears to be an indicator of materials biocompatibility. The butterfly-shaped structure of the BSA dimer (Fig. 1) displays a remarkable stability, as consequence of the 17 disulfide bridges existing within the protein core [13, 14].

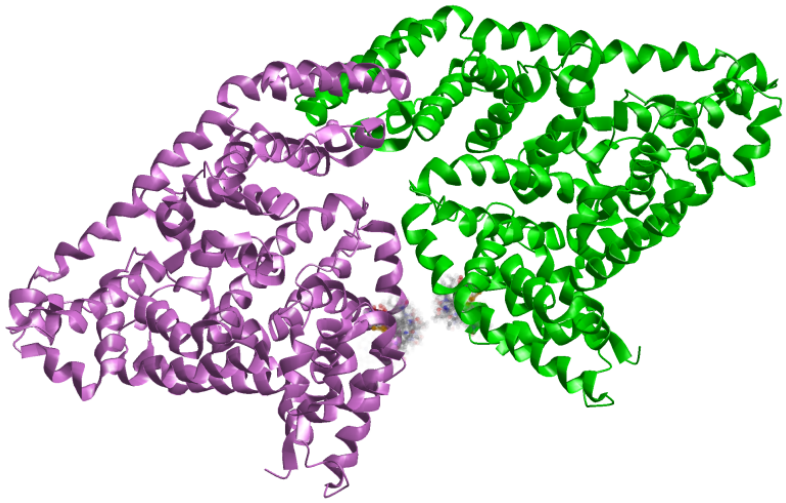

Fig. 1. The crystal structure of bovine serum albumin obtained by X-ray crystallography (pdb 4F5S). The two monomers are coloured in green and purple, respectively. For each native cysteine from position 34 are shown all the IA possible rotamers at 298 K.

In our experiments (4-(2-Iodoacetamido)-2,2,6,6-tetramethyl-1-piperidinyloxy) iodoacetamide (IA) spin label (Fig. 2) was used to label the cysteine residue located in position 34, which contains the unique free thiol group that is not involved in a disulfide bridge.

Fig. 2. Reaction of a protein with iodoacetamide spin label.

Having this paramagnetic centre attached on BSA molecule, we were able to explore protein adsorption onto investigated systems by means of electron paramagnetic resonance. The combination of spin labeling with electron paramagnetic resonance was previously reported as suitable for studying protein adsorption onto solid powder samples, in physiological environment [15-17].

The aim of this study was to develop biocompatible silica calcium systems containing dysprosium, iron and zinc embedded into albumin with possible application in both hyperthermia and radiotherapy. The in vitro protein adsorption was investigated by means of Electron Paramagnetic Resonance Spectroscopy.

1. Materials and methods

The compounds $50SiO_2•30CaO•10Fe_2O_3•10Dy_2O_3$ and $50SiO_2•28CaO•10Fe_2O_3•10Dy_2O_3•2ZnO$ (mol%), noted SiCaFeDy and SiCaFeDyZn, were synthesized by sol–gel method using as starting materials tetraethyl ortosilicate (TEOS, $Si(C_2H_5O)_4$, Sigma Aldrich), calcium nitrate ($Ca(NO_3)_2.4H_2O$), iron nitrate ($Fe(NO_3)_3·9H_2O$), dysprosium nitrate ($Dy(NO_3)_3·H_2O$) and respectively zinc nitrate hexahydrate ($Zn(NO_3)_2·6H_2O$) with high grade of purity (99.9%). The sol was prepared by stirring TEOS with water and alcohol in a 1:2:1 weight ratio catalysed by HNO_3 and heated to 80 ºC for about 30 min in a closed recipient in order to achieve a complete hydrolysis. Sol–gel method, via hydrolysis and condensation of molecular precursors, was considered due to this is a high-purity process that leads to excellent homogeneity. After the gel formation, the samples were dried in an electric oven at 110 °C for 24 h and then heat-treated at 800 °C and at 1200 °C for 3 h respectively, according to DTA measurements. The aim of the thermal treatment was to facilitate the growth of magnetic iron oxide crystalline phases.

Simultaneously differential thermal analysis and termogravimetric analysis (DTA/TG) were conducted on Shimadzu type derivatograph DTG-60H at a heating rate of 10 °C/min from room temperature to 1250 °C. Alumina open crucibles and α-alumina powder as reference material were used, and the measurement was made in a dynamic nitrogen and air atmosphere at a flow rate of 70 ml/min.

The specific surface area and pore volume were determined by measuring nitrogen adsorption/desorption at 77 K with Qsurf Series M1 surface area analyser, on the basis of Brunauer, Emmet and Teller (BET) method. The specific surface area

measurement was performed using three points BET method with corresponding N_2 and He gas mixtures.

For spin labeling procedure the bovine serum albumin solution (100 µM) was prepared from lyophilized protein (BSA from Sigma Aldrich, molar mass 69 kDa) in phosphate buffer (0.01M, pH 7.4). The protein solutions were incubated for 48 hours at 37°C with 6-fold molar excess of (4-(2-Iodoacetamido)-2,2,6,6-tetramethyl-1-piperidinyloxy) spin label. Unbound IA was removed by repeated dilution steps with sodium phosphate buffer, pH 7.4, using centrifugal filter units with 30 kDa molecular weight cut-off (Amicon/ Millipore, Carringtwohill, Co. Cork, Ireland). Labeling efficiency (spin label per cys-34) was determined to be 100%.

For protein adsorption experiment, powder samples (150 mg) were incubated for 4 hours at 37°C in 500 µl BSA solution (100 µM) in phosphate buffer (0.01M, pH 7.4). The BSA solutions withdrawn from the investigated samples were collected and after that the samples were washed three times with buffer solution, to remove the unattached protein molecules.

X band cw-EPR experiments were performed using an EPR spectrometer ADANI 6400, operating in X band (~ 9.5 GHz) at room temperature. The spectrometer settings were as follows: the microwave power was set to 1.0 mW; the B-field modulation amplitude was 0.15 mT. Glass capillaries of 1 mm inner diameter (i.d.) were filled with 20 µl sample, considering that the EPR active volume of the sample tube is 15 µl.

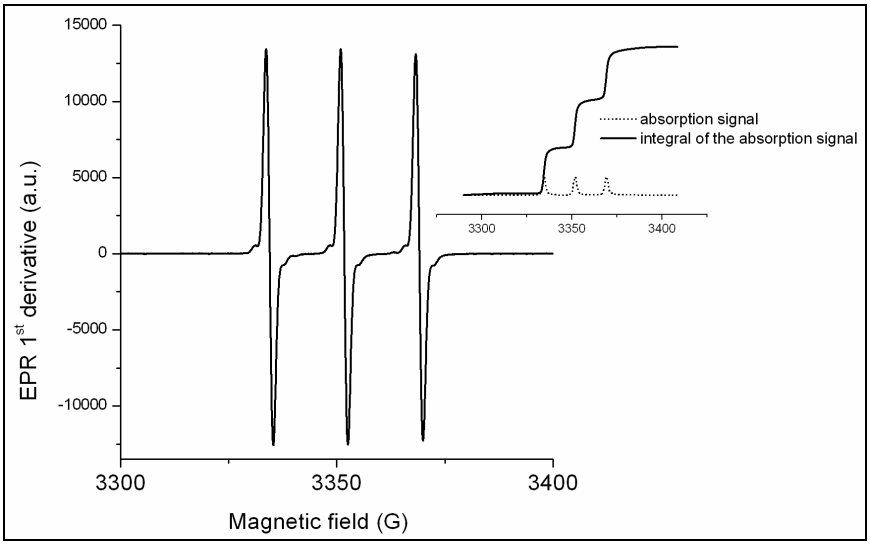

Fig. 3. Room temperature cw-EPR spectrum of the TEMPO standard solution (c = 100µM) used for concentration determination. Upper right: the absorption signal (dotted line) and its integration (black line).

The integrated EPR absorption signal is directly proportional to the spin concentration in the sample and was used to calculate the amount of the protein attached on the investigated systems. As reference spin probe, 2,2,6,6-Tetramethyl-1-piperidinyloxy (TEMPO) of 100 µM concentration was used (Fig. 3).

2. Results and discussion

The profile of the DTA curves (Figs 4 and 5) presents first a very intense endothermic peak around 100 °C corresponding to the removal of physically adsorbed water and alcohol remained in the sample after the hydrolysis and polycondensation of the inorganic components in the sol-gel process.

The significant mass loss in the range of 200-600°C corresponds together to the nitrates decomposition, organic decomposition and residues removal. The event is visualized by a broad endothermic peak around 400 °C for the both systems [5].

The exothermic peak around 1200 °C can be attributed to a crystallization process being associated with the formation of ferrite phases (magnetite, hematite or zinc ferrite) necessary for local heating by hysteresis.

According to DTA/TG measurements the thermal treatments of the two systems were established at 800 °C and 1200 °C primarily in order to remove the residual components and secondly to develop the necessary magnetic phases.

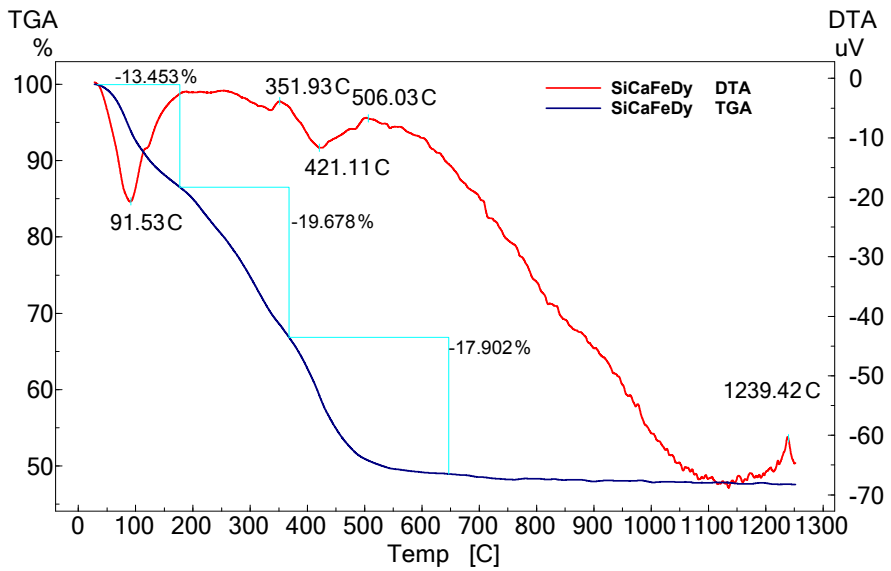

Fig. 4. DTA/TG curves of the SiCaFeDy system.

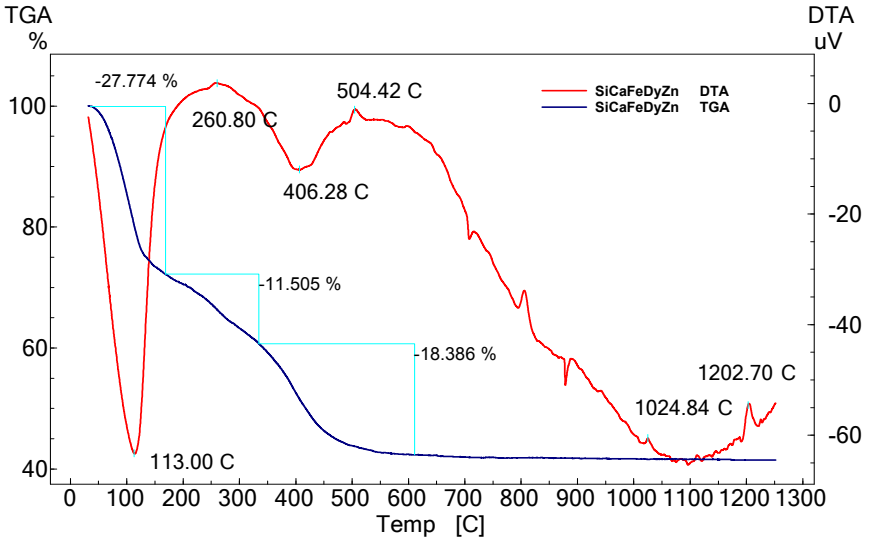

Fig. 5. DTA/TG curves of the SiCaFeDyZn system.

Three points BET surface area and the mean pore volume was also determined in order to evaluate the material porosity features that will define further the protein adsorption behaviour for biocompatibility appreciation. The BET specific surface area and pore volumes corresponding to the four investigated systems are listed in Table 1. The nitrogen adsorption/desorption studies for the 800 °C and 1200 °C heat treated samples show that the specific surface area and the mean pore volume are smaller for the zinc containing sample, thermal treated at 800 °C, while for the 1200 °C thermal treated samples the values were under the detection limit in both cases. These small values will impact the protein attachment profile.

Table 1. BET specific surface area and mean pore volume of the SiCaFeDy and SiCaFeDyZn samples

Sample	BET surface area (m^2g^{-1})	Pore volume (ml/g)
SiCaFeDy tt 800 °C	52	0.17
SiCaFeDy tt 1200 °C	< 1	-
SiCaFeDyZn tt 800 °C	32	0.11
SiCaFeDyZn tt 1200 °C	< 1	-

The EPR spectrum of BSA is characterized by the sum of two spectral components, representing two populations of spin labels with different mobility states: the relatively mobile component (*M*) is characterized by narrow linewidths of the central line and small apparent hyperfine splitting, while the strongly immobilized one, denoted *I*, has increased hyperfine splitting and line widths (see Fig. 6).

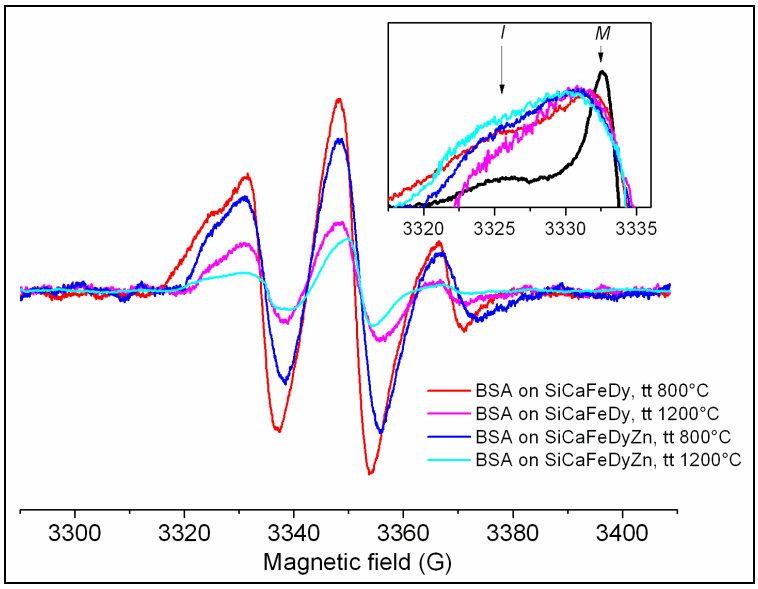

Fig. 6. Room temperature cw-EPR spectra of spin labeled BSA after adsorption on the investigated samples. Upper right inset: the low field spectral line of the normalized cw-EPR spectra recorded for spin labeled BSA before (black) and after adsorption onto the investigated samples.

Earlier EPR studies on BSA spin labeled in position cys34 also revealed a two-state model for the spin label side-chain, indicating that the nitroxide moiety is either free in the solvent or restricted as result of Cys34 location in a hydrophobic crevice of 9.5–10 Å depth (Fig. 1) [18-20].

Upon adsorption on the samples surface, the cw-EPR spectrum of BSA shows significant changes compared with the spectrum recorded in solution: the immobile component increases on the account of the mobile component (see inset of Fig. 6). This equilibrium shift is a clear indication of protein attachment and suggests the occurrence of local conformational changes in the vicinity of cysteine 34, as

consequence of the adsorption process. Moreover, the linewidth increase observed for the lower field spectral line represents a clear proof that the movement of the entire protein molecule is restricted after interaction with the samples substrate [15, 16].

The amount of the protein bound to the samples surface was estimated from the value of the spin concentration in the samples with BSA attached. For further verification, the EPR spectra of the withdrawn solutions obtained upon samples filtration were quantitatively analyzed (Fig. 7).

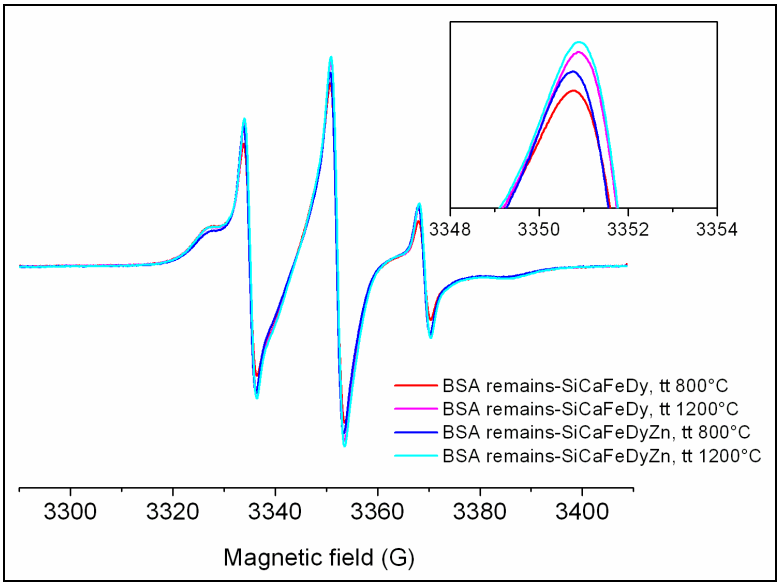

Fig. 7. Room temperature cw-EPR spectra of the withdrawn solutions obtained upon samples filtration. Upper right inset: top of the middle field spectral line, as appraisement of BSA amount remained in solution after adsorption process.

The obtained values are presented in Table 2 and indicate that the protein preferentially attaches onto the systems which are thermally treated at 800°C. Likewise, the systems without Zn content seem to be friendlier for protein adsorption. These results are in agreement with the values obtained for specific surface area, since both Zn and high temperature reduce the specific surface area, resulting less available surface for protein attachment.

Table 2. Molar concentration (in µM) of BSA before (black) and after adsorbed (red) onto the four investigated systems. The blue columns represent the amount of BSA remained in solutions after samples filtration. Errors are estimated to ±5%, due to experimental settings and uncertainties in baseline subtraction

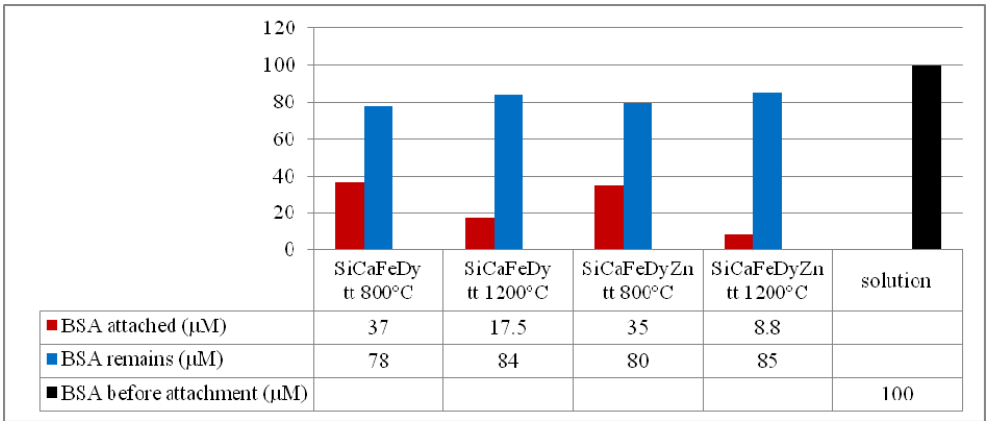

	SiCaFeDy tt 800°C	SiCaFeDy tt 1200°C	SiCaFeDyZn tt 800°C	SiCaFeDyZn tt 1200°C	solution
BSA attached (µM)	37	17.5	35	8.8	
BSA remains (µM)	78	84	80	85	
BSA before attachment (µM)					100

CONCLUSIONS

Calcium-silicate bioceramics containing iron, dysprosium and zinc, with potential applications in simultaneous radiotherapy and hyperthermia, were investigated with respect to their response regarding the BSA adsorption. The results show that the protein preferentially attaches onto the zinc free sample heat treated at lower temperature, as consequence of highly available specific surface area. The addition of ZnO decreases the surface activity in terms of protein attachment.

REFERENCES

[1] M. Kawashita, H. Takaoka, T. Kokubo, T. Yao, S. Hamada, T. Shinjo, *J. Ceram. Soc. Jpn.* (2001) 109, 39-44.

[2] S.K. Alpard, R.A. Vertress, W. Tao, D.J. Deyo, R.L. Brunston, J.B. Zwischenberger, *Perfusion* (1996) 11, 425-435.

[3] J.E. White, D.E. Day, *Key Eng. Mater.* (1994) 94–95, 181–208.

[4] V. Simon, D. Eniu, A. Takacs, K. Magyari, M. Neuman, S. Simon, *J. Non-Cryst. Solids* (2005) 351, 2365–2372.

[5] M. Tamasan, T. Radu, S. Simon, I. Barbur, H. Mocuta, V. Simon, *J. Optoelectron. Adv. Mater*. (2008) 10, 948-950.

[6] E. Vanea, M. Tămăşan, C. Albon, V. Simon, *J. Non-Cryst. Solids* (2011) 357, 3791-3796.

[7] T. Radu, M.T. Chiriac, O. Popescu, V. Simon, S. Simon, *J. Biomed. Mater. Res. A* (2013) 101, 472-477.

[8] Y. Ebisawa, T. Kokubo, K. Ohura, T. Yamamuro, *J. Mater. Sci. Mater. Med.* (1993) 4, 225-232.

[9] Y. Ebisawa, F. Miyaji, T. Kokubo, K. Ohura, T. Nakamura, *Biomaterials* (1997) 18, 1277-1284.

[10] D. Eniu, D. Cacaina, M. Coldea, M. Valeanu, S. Simon, *J. Magn. Magn. Mater*. (2005) 293, 310–313.

[11] L. Tang, A.H. Lucas, J.W. Eaton*, J. Lab. Clin. Med*. (1993) 122, 292-300.

[12] L. Tang, J.W. Eaton, *Am*. *J. Clin. Pathol*. (1995) 103, 466-471.

[13] D.C. Carter, B. Chang, J.X. Ho, K. Keeling, Z. Krishnasami, *Eur. J. Biochem*. (1994) 226, 1049–1052.

[14] T. Peters Jr., All about albumins: biochemistry, genetics, and medical applications. San Diego, Academic Press, 1996.

[15] C. Gruian, A. Vulpoi, H.-J. Steinhoff, S. Simon*, J. Mol. Struct.* (2012) 1015, 20-26.

[16] A. Vulpoi, C. Gruian, E. Vanea, L. Baia, S. Simon, H.-J. Steinhoff, G. Goller, V. Simon*, J. Biomed. Mater. Res*. *A* (2012) 100, 1179-86.

[17] K. Jacobsen, W. L. Hubbell, O. P. Ernst and T. Risse, *Angew. Chem. Int. Ed*. (2006) 45, 3874-3877.

[18] A. Alonso, W. Pereira dos Santos, S. Jacintho Leonor, J. Goncalves dos Santos, M. Tabak, *Biophys. J.* (2001) 81, 3566–3576.

[19] J.L. Vieira Anjos, P.S. Santiago, M. Tabak, A. Alonso, *Colloid Surface B* (2011) 88, 463-470.

[20] M. Oblak, A. Prezelj, S. Pecar, T. Solmajer, *Z. Naturforsch. C* (2004) 59, 880-886.

STUDIA UBB PHYSICA, Vol. 58 (LVIII), 1, 2013, pp. 77-85
(RECOMMENDED CITATION)

STRUCTURAL INVESTIGATION OF n-B_2O_3 MOLECULES (n=2-5) BY DFT CALCULATIONS

E. VINŢELER[a*]

ABSTRACT. The borate B_2O_3 glass system contains n-rings with n boron and n oxygen atoms. The structure of n-B_2O_3 molecules with n=2-5 with inequivalent topologies was constructed in a systematic way. The stability of molecules was studied by Density Functional Theory. We obtained 15 stable molecules and investigated their B-B distances. Four unstable molecules were studied and was shown that they do not retain their topological structure after minimization of energy.

Keywords: *glass, quantum-chemical simulation, regular graph*

INTRODUCTION

Boron glass network has been investigated and the main structural units illustrated by different techniques, one of the most important being the infrared spectroscopy. Usually the borate network is built from trigonal [BO_3] units, where every boron atom is situated at the centre of a triangle of oxygen atoms, with the oxygen atoms acting as bridges between pairs of boron atoms and boroxol $(B_3O_3Ø_3)^0$ rings, which are six-membered planar and regular rings, connected by three bridging oxygens Ø [1]. The borate glasses also contain n-rings $(B_nO_nØ_n)^0$ with *n* boron and *n* oxygen atoms, connected by *n* bridging oxygens Ø. Liakos and Simandiras [2] simulated a cluster of $20B_2O_3$ molecules and observed the existence of boroxol rings and the creation of n-rings with *n* between 3 and 12.

The growth of small clusters of boron compounds B_nO_m have been investigated by Drummond et al. [3] for *n=1-7* and *m=1-3,* by Tai et al. [4] for *n=5-10* and *m=1-2* and by Shivachev et al. [5] for *n=1-6* and *m=1-16.* Bigger clusters of boron oxide were studied due to their possible applications. Clusters with cage-like shape could be useful

[a] Babeş-Bolyai University, Faculty of Physics, 1 Kogalniceanu Str., 400084 Cluj-Napoca, Romania
[*] Corresponding author: emil.vinteler@phys.ubbcluj.ro

as nanocapsules for gas storage as was shown by Dabbagh et al. [6]. Charkin et al. [7] studied a cluster of $10B_2O_3$ molecules with dodecahedron symmetry build from 12 adjacent 5-rings.

Yuan and Xue [8] analyzed the crystal structure of 841 borate minerals and classified the fundamental building blocks (FBBs) (first introduced by Burns et al. [9][10]) into 6 types in terms of their topological structures: single trigonal [BO_3] or tetragonal [BO_4] borates; branched borates; normal-ring borates; bridge-ring (two-adjacent rings) borates; '8'-shaped-ring borates and combined-ring borates.

In our article we consider a simpler task: to generate clusters of n-B_2O_3 molecules with inequivalent topologies, build from n-rings with trigonal [BO_3] units only. We study their stability and their geometrical properties by using Density Functional Theory (DFT) calculations.

GENERATION OF n-B_2O_3 MOLECULES WITH INEQUIVALENT TOPOLOGIES

It is proposed a simple way for generating n-B_2O_3 molecules with inequivalent topologies. For this purpose molecules are interpreted as networks with nodes and links, where the boron atoms are nodes and B-O-B bonds are links, respectively. Exactly three links converge in a single node, because there are only trigonal [BO_3] units. Two nodes are connected with exactly one link (we don't consider molecules containing B_2O_2 rings). Inside the network we have different n-rings containing n nodes (only boron atoms are counted) and n links.

It is important to know the number of different n-rings in a given molecule. For $2B_2O_3$ molecule is used notation $2B_2O_3$-3333 to indicate that $2B_2O_3$ molecule is a network with tetrahedron shape (only boron atoms are considered) composed from four 3-rings (boroxol $(B_3O_3Ø_3)^0$ rings). For $3B_2O_3$ molecule is used notation $3B_2O_3$-33444 to indicate that $3B_2O_3$ molecule has the shape of triangular prisme with two 3-rings and three 4-rings. For $4B_2O_3$ molecule we have three possible networks with different topologies: $4B_2O_3$-444444 molecule with cube shape, $4B_2O_3$-334455 molecule with two 3-rings, two 4-rings and two 5-rings and $4B_2O_3$-333366 molecule with four 3-ring and two 6-ring (see Fig.1). For $5B_2O_3$ molecule we have nine networks with different topologies: $5B_2O_3$-4444455 with pentagonal prism shape, $5B_2O_3$-3444555, $5B_2O_3$-3344466, $5B_2O_3$-3344556, $5B_2O_3$-3334467, $5B_2O_3$-3335556, $5B_2O_3$-33335555, $5B_2O_3$-33334444 and $5B_2O_3$-3333477 (see Fig.1). In addition we consider $6B_2O_3$-33336666 molecule with truncated tetrahedron structure formed from four triangles and four hexagons and $10B_2O_3$ molecule with dodecahedron shape formed entirely from 5-rings.

We apply the following four modalities to generate (n+1)-B_2O_3 molecule from n-B_2O_3 molecule by adding two new nodes and three new links:

1. we add 2 nodes on existing different links and connect them with a new link. Example: We add a new link (represented with a thick line) in $3B_2O_3$-33444 molecule to generate $4B_2O_3$-444444 molecule (see Fig.1).

2. we add 2 nodes on the same link; we delete an old link; we add 2 new links to connect the new nodes with the old ones. Example: We add two new links (represented by thick lines) and delete an old link in $3B_2O_3$-33444 molecule to generate $4B_2O_3$-333366 molecule (see Fig.1).

3. we add 2 nodes outside the existing links and connect them with a new link; we delete two old links; we add 4 new links to connect the new nodes with the old ones. Example: We add five new links (represented by thick lines) and delete two old links in $3B_2O_3$-33444 molecule to generate $4B_2O_3$-334455 molecule (see Fig.1).

4. we add 2 nodes outside the existing links and connect them with a new link; we delete three old links; we add 6 new links to connect the new nodes with the old ones. Example: We add six new links represented by thick lines) and delete three old links in $4B_2O_3$-334455 molecule to generate $5B_2O_3$-3344556 molecule (see Fig.1).

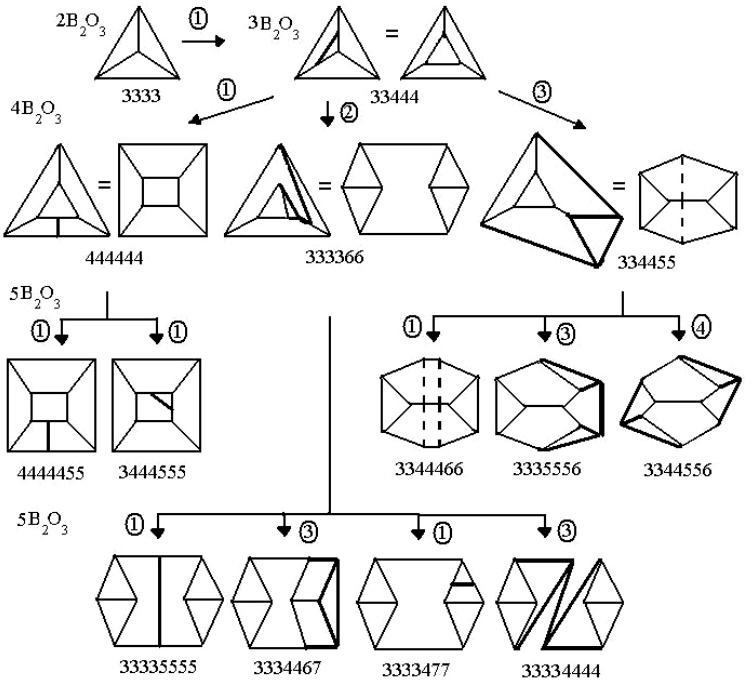

Fig. 1. Generation of n-B_2O_3 molecules with different topologies using the four methods mentioned in text (the numbers in circles). The boron atoms are represented by nodes and B-O-B bonds by links, respectively. The thick lines represent the new links added. The equality sign indicates the topological equivalence of the models.

Not all generated molecules can exist, because they must satisfy several geometrical contraints: link length (B-B distance) is smaller than two times B-O bond length; links do not cross or more precisely the distance between links is bigger than O-O bond length and so on. The molecules that survive this topological and geometrical selection have not necessary the most stable structure. We must check their stability by using DFT computations.

STABILITY OF n-B_2O_3 MOLECULES

For each proposed model we performed direct optimization of the geometry with the help of B3LYP/6-31G(d) method and using Gaussian 09 program [11]. Frequency analysis followed all optimizations in order to establish the nature of the stationary points found, so that all the reported structures in this study are genuine minima on the potential energy surface, without any imaginary frequencies.

In combinatorial mathematics all connected 3-valence graphs (named also cubic graphs) up to 24 nodes were determined by Brinkmann [12] and the numbers of such graphs with different topologies and with 2n-nodes, for n=2, 3… are 1, 2, 5, 19, 85, 509. But only some of the graphs are planar and correspond to a planar or cage-like structure of a stable molecule. The number of planar cubic graphs with 2n-nodes, for n=2, 3… are 1, 1, 3, 9, 32, 133. We can summarize in Table 1 below the number of n-B_2O_3 molecules:

Table 1. The number of total, stable and unstable n-B_2O_3 molecules

n	4	6	8	10
Total number	1	2	5	19
Number of stable molecules	1	1	3	9
Number of unstable molecules	0	1	2	10

Due to this information we are enabled to affirm that we obtained all stable n-B_2O_3 models with inequivalent topologies up to n=5 and their structure is represented in Fig. 2.

The stability of n-B_2O_3 molecules can be determined using the energy per B_2O_3 group: $E=E_{HF}(n\text{-}B_2O_3)/n\text{-}2E(B)\text{-}3E(O)$, where E_{HF} (n-B_2O_3) is Hartree-Fock energy of n-B_2O_3 molecule, E(B) - energy of boron atom and E(O) – energy of oxygen atom, respectively. The stability increases with the increase of energy E. Looking at the energy E in Table 2 can be observed that the stability of models increases with the increase of number of B_2O_3 molecules.

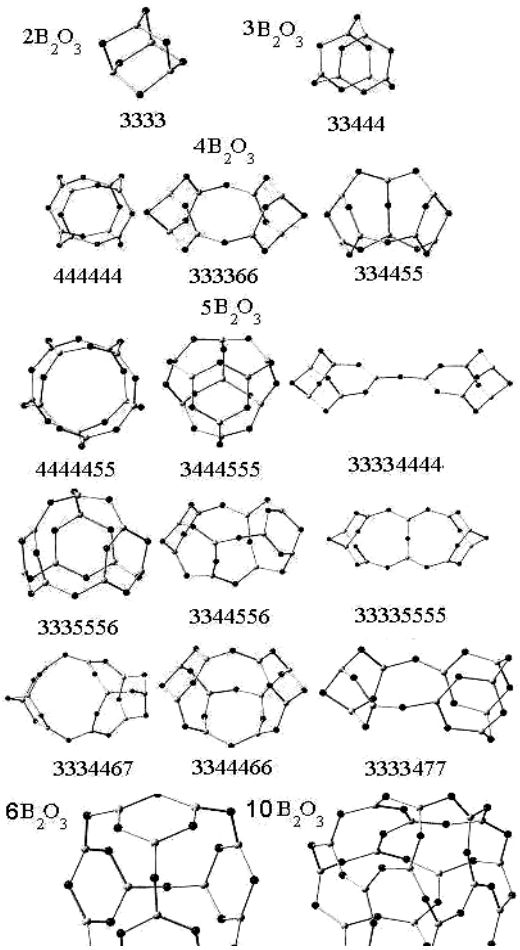

Fig. 2. Structure of stable n-B_2O_3 molecules with inequivalent topologies (white circles - boron atoms, black circles - oxygen atoms). The numbers below indicate the types of faces contained in the molecule.

Table 2. Symmetry, structure, energy per group E and the difference of energy ΔE between the lowest lying model and the specified nB_2O_3 (n=2-10) model for a given n, as was inferred from DFT calculations

n	Model	Symmetry	Energy E (eV)	Energy ΔE(eV)
2	3333	Td	34.98	0.00
3	33444	D3h	36.84	0.00
4	334455	C2v	37.54	0.00

n	Model	Symmetry	Energy E (eV)	Energy ΔE(eV)
4	444444	Th	37.37	0.17
4	333366	C2v	37.14	0.40
5	3335556	C3	37.97	0.00
5	3344466	C2v	37.85	0.12
5	3344556	C2	37.85	0.12
5	3444555	C3v	37.76	0.21
5	4444455	D5h	37.71	0.26
5	3333477	C2	37.62	0.35
5	3334467	Cs	37.55	0.42
5	33335555	D2h	37.44	0.53
5	33334444	C2v	36.90	1.07
6	33336666	S6	38.27	0.00
10	$10B_2O_3$	Ih	38.46	0.00

The number of geometrical properties of models in Fig.2 is huge. We restrict our attention only to B-B distance in n-rings with *n=3* and *n=4*, that form triangles and rectangles. The 3-rings adjacent to three n-rings with the same *n* form equilateral triangles with equal 3n-edges. 3-rings adjacent to two n-rings with the same *n* and one 3-ring form isoscel triangle with two 3n-edges and one 33-edge. 4-rings adjacent to two opposite 4-rings and two opposite n-rings with the same *n* form rectangles with two 44-edges and two 4n-edges.

These geometrical properties are summarized in Table 3. We observe that B-B distance for 33-edge is 2.16 Å and for 44-edge is 2.43 Å. B-B distance for 34-edge is 2.35 Å, a value between the previous ones. This shows that the electrons are redistributed between the adjacent 3-ring and 4-ring and the chemical bond on 34-edge choses an intermediate value in order to harmonize the double constraint on being on two different n-rings.

We observe that with the increase of n, the electrons become more delocalized due to the aromatic property of n-rings and the length of bonds in equilateral 3-rings increases. In isoscel 3-rings the electrons from the 3n-edges migrate to 33-edges and the length of 33-edges decrease and that of 3n-edges increase with the increase of *n*. In 4-rings the length of 44-edge and that of 4n-edge increase with the increase of *n*.

The values contained in Table 3 are useful if we want to generate for a given *n* all molecules with inequivalent topologies. First we obtain from topological considerations the n-rings contained in molecule and which are adjacent to another. After this we can impose the geometrical constraints for B-B distances derived from Table 3 knowing the length for nm-edges.

Table 3. B-B distance for *nm* edges for adjacent *n*- and *m*-rings of borate nB_2O_3 models (n=2-10) inferred from DFT calculations

	Adjacent faces with n-rings					
	n		3	4	5	6
B-B distance (Å)	Equilateral triangle	3n-edge	2.06	2.25	2.35	2.37
	Isoscel triangle	33-edge	2.06	2.00	1.99	1.98
		3n-edge	2.06	2.18	2.25	2.28
	Rectangle	44-edge	2.18	2.34	2.51	2.56
		4n-edge	2.25	2.34	2.37	2.43

After description of stable molecules with planar graphs, we consider the unstable molecules. Their graphs are non-planar and we must connect the boron atoms situated on opposite sides of the molecule with a bridge that crosses the interior of the molecule (see Fig.3).

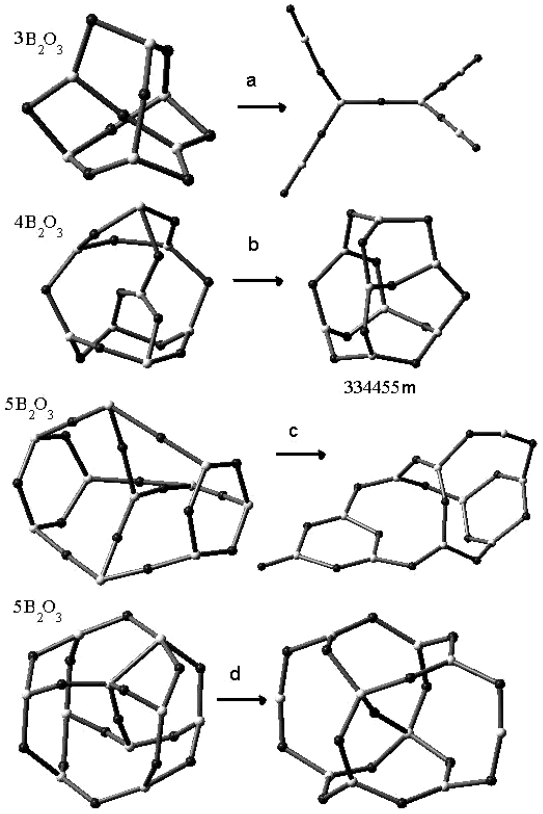

Fig. 3. Structure of unstable n-B_2O_3 molecules (white circles - boron atoms, black circles - oxygen atoms).

From Table 1 follows that for n=3 exist a single unstable molecule, represented in Fig.3a. Minimization of energy by DFT calculations breaks some B-O links in the n-rings and we obtain a chain-like structure with terminal oxygen atoms connected by double bonds.

For n=4 exist two unstable structures. First structure is a cube with twisted edges that is topologically distinct from the cube. Physically it is impossible due to the crossing of its links. The second structure (see Fig.3b) is permited by geometrical constraints, but is modified during minimization of energy in a structure topologically equivalent, but geometrically distinct from the structure of $4B_2O_3$-334455 molecule. It has a lower energy per atom by 0.50 eV meaning that it is more unstable than $4B_2O_3$-334455 molecule and we denote it by $4B_2O_3$-334455m.

For n=9 exist 10 unstable structures, but 8 are geometrically rejected due to the crossing of their links. The remaining structures are permited by gometrical constraints. The first structure (see Fig.3c) is modified during minimization of energy in $5B_2O_3$-3355566 structure, that has in addition a terminal B-O^- link and a O-B^+-O link on 55-edge. The second structure (see Fig.3d) is a cube with two additionally atoms on the opposite sides linked by a bridge crossing the cube. It is modified in a new structure containing two tetrahedral [BO_4] units and two O-B^+-O links.

After completion of this work we have received the article by Li and Cheng [13] that overlaps partially with ours. They investigated the electronic structure of n-B_2O_3 molecules for n=1-6, but considered not only simple B-O bonds, but also double bonds and obtained several chain-like structures. For n=4 they omitted $4B_2O_3$-333366 structure. For n=5 they omited eight structures apart $4B_2O_3$-3335556 chiral cap.

CONCLUSIONS

It is proposed a way to obtain molecules with inequivalent topologies, by generating (n+1)-B_2O_3 molecules from n-B_2O_3 molecules beginning from $4B_2O_3$ molecule with tetrahedron shape. Not all obtained molecules are physically possible. It was shown that, up to n=5, the molecules retain their topological structure if the corresponding graph is planar. For molecules with non-planar graph, geometrical constraints (for example the crossing of links) can eliminate many physically impossible structures.

For molecules with planar graphs, the lengths of nm-edges were obtained by DFT calculations. Their values can be useful in imposing geometrical constraints and in selecting physically possible molecules. For molecules with planar graphs was investigated their stability and calculated the energy per atom by DFT calculations.

It was shown for molecules with corresponding non-planar graphs and *n* up to 5 that they do not retain their topological structure during the minimization of their energy.

REFERENCES

1. D.L. Griscom, „Borate glasses: Structure, Properties, Applications", Materials Science Research, vol. 12, L.D. Pye, V. D. Frechette, N. J. Kreidl, Eds., Plenum Press, New York, 1978, 11.
2. D.G. Liakos, E.D. Simandiras, *J. Phys. Chem. A*, 112 (34), 7881, (2008).
3. M.L. Drummond, V. Meunier, B.G. Sumpter, *J. Phys. Chem. A*, 111, 6539, (2007).
4. T.B. Tai, M.T. Nguyen, D.A. Dixon, *J. Phys. Chem.*, 114(8), 2893, (2010).
5. B. Shivachev, E. Kashchieva, Y. Dimitriev, *Physics and Chemistry of Glasses - European Journal of Glass Science and Technology Part B*, 2005, 46 (2), 253
6. H.A. Dabbagh, M. Zamani, H. Farrokhpour, *Chem. Phys.,* 393, 86, (2012).
7. O.P. Charkin, N.M. Klimenko, D.O. Charkin, *Russ. J. of Inorg. Chem.*, 53, 568, (2008).
8. G. Yuan, D.Xue, *Acta Crystall.* B, 63, 353, (2007).
9. P.C. Burns, J.D. Grice, F.C. Hawthornes, *Canad. Mineral.*, 33, 1131, (1995).
10. J.D. Grice, P.C. Burns, F.C. Hawthornes, *Canad. Mineral.*, 37, 731, (1999).
11. M.J. Frisch, G.W. Trucks, H.B. Schlegel, G.E. Scuseria, M.A. Robb, J.R. Cheeseman, G. Scalmani, V. Barone, B. Mennucci, G.A. Petersson, H. Nakatsuji, M. Caricato, X. Li, H.P. Hratchian, A.F. Izmaylov, J. Bloino, G. Zheng, J.L. Sonnenberg, M. Hada, M. Ehara, K. Toyota, R. Fukuda, J. Hasegawa, M. Ishida, T. Nakajima, Y. Honda, O. Kitao, H. Nakai, T. Vreven, J. A. Montgomery, Jr., J.E. Peralta, F. Ogliaro, M. Bearpark, J.J. Heyd, E. Brothers, K.N. Kudin, V.N. Staroverov, R. Kobayashi, J. Normand, K. Raghavachari, A. Rendell, J.C. Burant, S.S. Iyengar, J. Tomasi, M. Cossi, N. Rega, J.M. Millam, M. Klene, J.E. Knox, J.B. Cross, V. Bakken, C. Adamo, J. Jaramillo, R. Gomperts, R.E. Stratmann, O. Yazyev, A.J. Austin, R. Cammi, C. Pomelli, J.W. Ochterski, R.L. Martin, K. Morokuma, V.G. Zakrzewski, G.A. Voth, P. Salvador, J.J. Dannenberg, S. Dapprich, A.D. Daniels, Ö. Farkas, J.B. Foresman, J.V. Ortiz, J. Cioslowski, and D.J. Fox, Gaussian 09, Revision A.1, Gaussian, Inc., Wallingford CT, 2009.
12. G. Brinkmann, *J. Graph Theory,* 23, 139, (1996).
13. L. Li, L.Cheng, *J. Chem. Phys.*, 138, 094312, (2013).

STUDIA UBB PHYSICA, Vol. 58 (LVIII), 1, 2013, pp. 87-94
(RECOMMENDED CITATION)

EQUIVALENT ELECTRIC CIRCUIT FOR A HARMONICALLY PERTURBED ACCRETION DISK AROUND SUPERMASSIVE BLACK HOLES

N. VERBA[a], G. MOCANU[a,b,*]

ABSTRACT. Studying the behaviour of matter around exotic objects, such as supermassive black holes, has proven to be very difficult. Both theoretical and observational tools are incomplete. We propose that advances in this issue can be attained if one looks at an accretion disk and views it as an electronic black box and tries to find a correlation between the parameter space of this black box and the physics of the disk.

Keywords: *supermassive black holes, magnetohydrodynamics, equivalent electric circuit.*

INTRODUCTION

Almost ubiquitous in BL Lacertae objects [1] and present in other Active Galactic Nuclei (AGN) flavors, Intra Day Variability (IDV, variability in the luminosity output on timescales of less than one day) in the optical regime is still an issue of debate. The physics of the underlying process is not well known but there is overwhelming evidence that the magnetic field plays an important role in the generation of the observed light curves [2]-[7].

Because of this feature, any analysis of an accretion disk has to take into account the effects of a magnetic field permeating the disk. In this context, the possibility to characterize the behavior of the accretion disk by just a handful of parameters is paramount. The parameter space we wish to investigate in this work is based on the following line of thought: the disk can be viewed as a black box; when an input information signal is passed through this black box, the output is a convolution of the characteristics of the black box with the input signal. So by

[a] Automation Department, Technical University, Baritiu Street, 26-28, 400027, Cluj-Napoca, Romania
[b] Faculty of Physics, Babes-Bolyai University, Kogalniceanu Street, 1, 400084, Cluj-Napoca, Romania
[*] Corresponding author: gabriela.mocanu@ubbcluj.ro

feeding the disk a known perturbation and analyzing what the output is, we can find information about the black box itself. As a particular feature, we characterize the black box in terms of electronic circuit components. Then, as seen in this work, we can say that the parameter space for the disk consists of two diodes, one inductance and one resistance of given numerical values, etc.

This paper has the following structure. The first section will discuss the MHD equations and numerical simulations to produce the light curve of a perturbed accretion disk. In the second part we present and discuss the equivalent electric circuit which produces a similar output when fed with the same disturbance as the accretion disk. The last section consists of a discussion to find the relationships between the physical characteristics of the disk and the electrical circuit and conclusions.

MHD EQUATIONS

The MagnetoHydrodynamical equations that describe a magnetized rotating disk are the continuity equation

$$\frac{\partial \rho}{\partial t} + \nabla \rho \cdot \mathbf{v} = 0 \quad (1),$$

the Navier-Stokes equation

$$\rho \frac{\partial \mathbf{v}}{\partial t} + (\rho \mathbf{v} \cdot \nabla)\mathbf{v} = -\rho \nabla \phi_g - \nabla p + \frac{1}{\mu_0}(\nabla \times \mathbf{B}) \times \mathbf{B} \quad (2),$$

the induction equation, taking into account non-ideal magnetic diffusivity effects

$$\frac{\partial \mathbf{B}}{\partial t} = \nabla \times (\mathbf{v} \times \mathbf{B} - \eta_B \nabla \times \mathbf{B}) \quad (3),$$

and the solenoidal constraint

$$\nabla \cdot \boldsymbol{B} = 0 \quad (4),$$

where ρ is the density of the disk, $\boldsymbol{v}$ is the velocity of a plasma element, $\boldsymbol{B}$ is the magnetic field in the disk, μ_0 is the magnetic permeability of free space, p is the pressure in the disk, ϕ_g is the gravitational potential due to the supermassive object and η_B is the magnetic diffusivity of the plasma in the disk.

The equilibrium disk is well described by a time steady cylindrical symmetry, such that $\frac{\partial}{\partial t} = \frac{\partial}{\partial \phi} = 0$. The disk structure may be characterized by a central temperature depending only on *r* and the dependence on the *z* coordinate may be neglected [8]. As a feature of the standard thin disk assumption, the variation of physical parameters with height can be ignored, $\frac{\partial}{\partial z} = 0$. The gravitational

potential outside the event horizon of the super massive black hole is described by the Newtonian potential $\phi_{\mathrm{g}}(\mathrm{r}) = -\frac{\mathrm{GM}}{\mathrm{r}}$, where G is the gravitational constant and M is the mass of the black hole. A test plasma volume in a Keplerian disk experiences a velocity equal to the Kepler velocity $\mathbf{v}_0(r) = (0, \mathrm{u_k}(r), 0)$; $\mathrm{u_k(r)} = \sqrt{\frac{\mathrm{GM}}{\mathrm{r}}}$ and an angular velocity equal to the Kepler angular velocity $\boldsymbol{\Omega}_0(r) = (0,0, \Omega_{\mathrm{k}}(\mathrm{r}))$; $\Omega_{\mathrm{k}}(\mathrm{r}) = \sqrt{\frac{\mathrm{GM}}{\mathrm{r}^3}}$.

The equilibrium state is perturbed by a temporal variation in the density at the outer boundary. When the perturbation is applied, the new physical parameters f that satisfy the MHD equations consist of a sum of two parts $f = f_0 + f_1$, the equilibrium part (denoted by subscript 0) and the perturbed part (denoted by subscript 1). The density perturbation, which causes all other fluctuations, is in the most general case written as $\rho_1(r,t) = \mathrm{A_\rho}\rho_{\mathrm{r}}(\mathrm{r})\rho_{\mathrm{t}}(\mathrm{t})$, where $\mathrm{A_\rho}$ is the amplitude of the perturbation in density and $\rho_{\mathrm{r}}(r)$ and $\rho_{\mathrm{t}}(t)$ are the functional forms of its space dependency and time dependency respectively.

Angular momentum is transported outwards by a sum of Reynolds and Maxwell stresses [2], [9] and we assume that the perturbations in this mechanism are responsible for the variability, i.e. this produces the output signal. The component of the stress tensor responsible for the luminosity is defined as

$$\mathbf{m_{r\phi}}(\boldsymbol{r},\boldsymbol{t}) = \boldsymbol{\mu_0\rho_0\upsilon_r\upsilon_\phi} - \mathbf{B_r B_\phi} \tag{5}$$

The luminosity emitted from a patch of the disk due to the perturbation, between radii r_1 and r_2 is [9]

$$\mathbf{L_{12}}(\boldsymbol{t}) = \int_{\mathbf{r_1}}^{\mathbf{r_2}} \mathbf{m_{r\phi}}(\boldsymbol{r},\boldsymbol{t})\boldsymbol{dr}. \tag{6}$$

The disk is perturbed by depositing mass in the outer strip found at radius $\mathrm{r_0}$. The functional form of the perturbing density is $\rho_{\mathrm{r}}(\mathrm{r}) = 1$ for the radial dependence. The quantity of mass is distributed on a ring of width d and of area $2\pi \mathrm{r_0 d}$, as it is logical to think that mass input to the AGN accretion disk comes from many sources surrounding the disk [10]

$$\mathbf{A_p} = \frac{\mathbf{M_{added}}}{\mathbf{2\pi r_0 d}}\frac{\mathbf{1}}{\mathbf{year}} \tag{7}$$

Because the perturbed quantities entering in Eq.(6) through Eq. (5), i.e. $v_r, v_\phi, B_r, B_\phi,$ depend linearly on the perturbation amplitude, $\mathrm{A_\rho}$, we expect that the luminosity will depend on the perturbation amplitude as $O(A_\rho^2)$. The temporal evolution of the perturbation in density is given by the harmonic function $\rho_{\mathrm{t}}(t) = \cos(t \cdot t_f)$ which assures periodic perturbation of the feeding rate with period $2\pi/\mathrm{t_f}$, where $\mathrm{t_f}$ is the frequency (Fig. 1). The perturbation in the disk

density is modeled as a cosine in time, with a given frequency. The value of the frequency is chosen so as to realistically approach the observed short time scale variability of this object, with the underlying assumption that fast variability can be produced by fast perturbations.

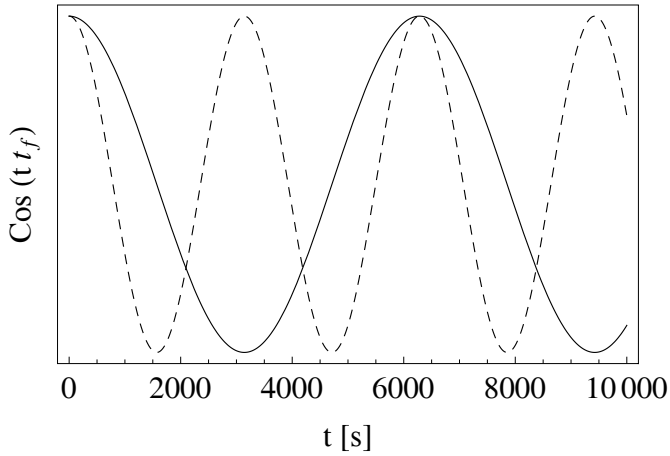

Fig. 1. Temporal evolution of the perturbation in density, for $\mathrm{t_f} = 0.001$ (full line) and $\mathrm{t_f} = 0.002$ (dashed line).

Although this analytical shape of the perturbing function is not realistic, it is useful in characterizing the black box, by calculating its cosine response. The luminosity output was numerically computed in Mathematica for the following parameters, all given in SI units: for the physical constants $\tilde{\mu} = 1.27, \mathrm{c} = 3 \times 10^8$, $\mathrm{M_\odot} = 2 \times 10^{30}$, $\mathrm{G} = 6.6 \times 10^{-11}$, $k_B = 1.3 \times 10^{-23}, \mu_0 = 4\pi 10^{-7}, m_p = 1.6 \times 10^{-27}$ and the model assumptions $T(r) = \alpha r^{-\tau}$ [11], $\tau = -\frac{3}{4}$ and $\alpha = 10^{15}$, $\mathrm{M} = 10^8 \mathrm{M_\odot}$, $\mathrm{r_o} = 20\mathrm{r_g}, \mathrm{r_i} = 5\mathrm{r_g}, \mathrm{B_{Edd}} = 4$, $\rho_\mathrm{c} = \frac{1}{10}$ $\mathrm{B_{a\upsilon}} = 0.00004$, $\mathrm{B_{z0}} = 0.00003$, $\mathrm{B_{\phi 0}} = \sqrt{\mathrm{B_{a\upsilon}^2 - B_{z0}^2}}$, $\mathrm{B_{zi}} = \frac{\mathrm{B_{a\upsilon}}}{100}$, $\mathrm{B_{\phi i}} = \frac{\mathrm{B_{a\upsilon}}}{100}, \rho_0(r) = ar + b$, $\mathrm{a} = 1.469 \times 10^{-13}$, $b = 0.138$, $\eta_\mathrm{B} = 6, \mathrm{b_{r0}} = 10^{-11}$, $\upsilon_{\mathrm{r0}} = -\frac{\mathrm{b_{r0}}}{\sqrt{\mu_0 \rho_{\mathrm{r0}}}} = -2.8 \times 10^{-8}$, $M_{added} = 0.01\ \mathrm{M_\odot}$, where α is fixed such that the temperature in the disk is of $\mathrm{O}(10^6 \mathrm{K})$ [11].

The simulation was ran for the cases $\mathrm{t_f} = 0.001$ or $\mathrm{t_f} = 0.002$ and for an annulus between $\mathrm{r_0} = 20 r_g$ and $\mathrm{r_i} = 19 r_g$, producing the perturbation part of the output luminosity shown, in Fig. 2.

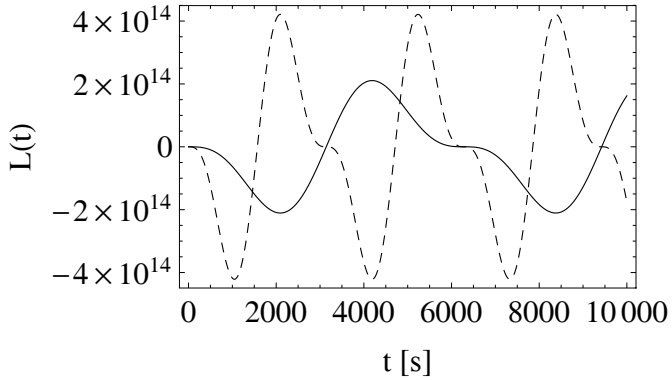

Fig. 2. Output luminosity, for $t_f = 0.001$ (full line) and $t_f = 0.002$ (dashed line). A very interesting feature, a "shoulder", can be seen in the output luminosity.

By running more simulations we noticed that the qualitative behavior of the shoulder in the output luminosity depends on the distance with respect to the central engine. For our purposes, the parameters that characterize the system in an AGN state-space are the mass of the object, the perturbation period t_f, the value of the magnetic field and the radius of emission.

EQUIVALENT CIRCUIT

The next task is to find an equivalent electrical circuit that distorts an input signal in a way similar to the disk. The proposed solution uses the following components: one sinusoidal AC current source, two diodes, one coil, a resistor and a ground. The topology of the electric circuit formed with these elements is shown if Fig. 3.

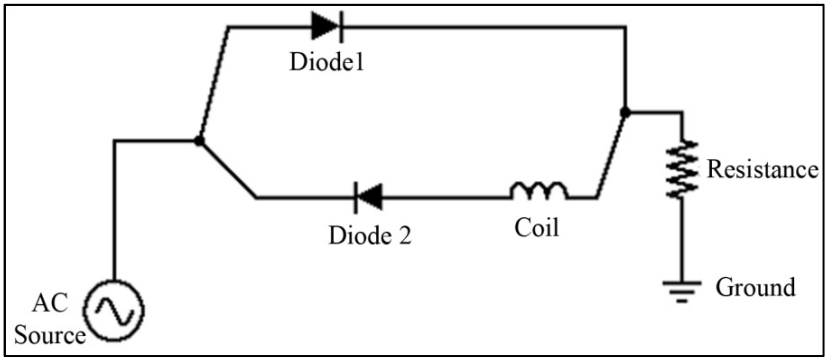

Fig 3. Topology of the equivalent electric circuit.

The AC Source from Fig. 3 is a sinusoidal input, similar to the one used in the numerical MHD simulations. The diodes are not ideal, they have a threshold voltage, allowing to obtain a feature similar to the shoulder in the output graph. If we would use only a set of two diodes without the coil we would get an output similar to Fig. 4.

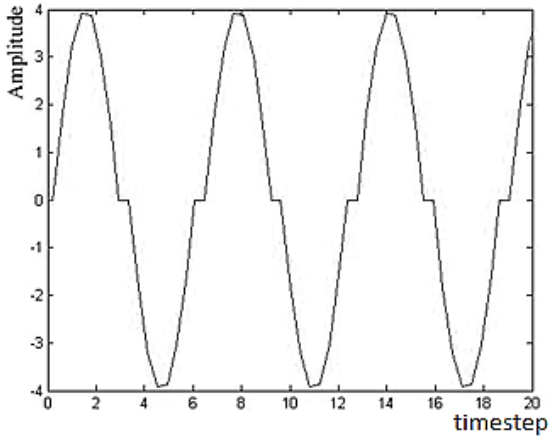

Fig. 4. Output of the equivalent circuit if the coil is on the lower branch in Fig. 3 would be missing.

The role of the coil is to create a phase shift in the wave in order to make the second shoulder (left hand side of the peak) obsolete, and create a wave pattern as the one shown in Fig. 5, very similar to what the numerical simulation produced for the disk. The role of the resistance and the ground is nearly that of a sink.

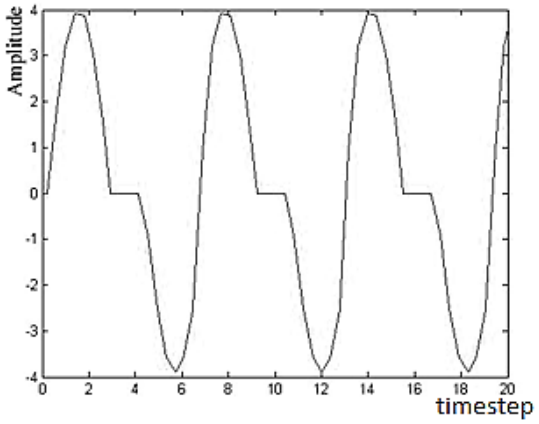

Fig. 5. Output of the equivalent electric circuit shown in Fig. 3.

To make this into a reusable versatile simulation we use Matlab/Simulink with the following blocks: a Sine Wave block for the AC current source, having the parameters of Amplitude set to 5 and the frequency set to 1; Dead Zone Block Diode to stand for the diodes. The diode on the upper branch has the parameters of "Start of Dead zone" set to –infinity and "end of Dead zone" set to 1, to mimic a threshold voltage of 1V; the diode on the lower branch is replaced by a Dead Zone Diode with the parameters of "Start of Dead zone " set to –1 and "end of Dead zone" set to infinity, modeling a diode inserted after it has been flipped by 180 degrees. The coil is modeled by a Transport Delay block having the Time delay parameter set to 1. The Resistance and the ground are merely replaced by Scope blocks (sinks of the signal) to be able to view the results. The outputs of the first Dead Zone Block and the second one are connected with a Sum Block to the Scope. The resulting Model is shown in Fig. 6.

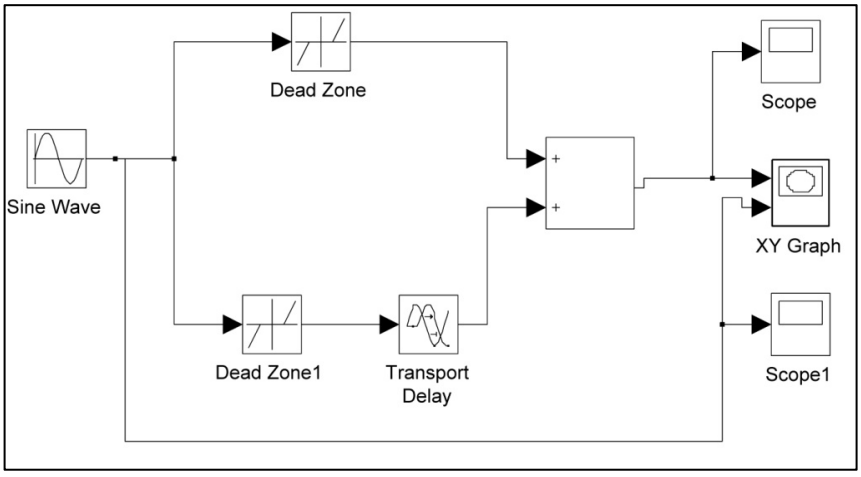

Fig. 6. Simulink model used to implement the equivalent electrical circuit in Fig. 3.

From the Simulink simulation two graphs were obtained. In Fig. 7 the input (dotted line) and output (continuous line) signals are shown simultaneously.

CONCLUSIONS

The physics of an accretion disk around a supermassive object was discussed by analytical and numerical analysis. Numerical simulations of the response of an accretion disk subjected to a harmonic density perturbation show an interesting feature, namely a „shoulder". With the focus to reproduce this feature, an equivalent

electrical model was proposed, discussed and simulated with Simulink. Future work will focus on defining a bijective function between the parameter space of the disk and the parameter space of the elements of the equivalent electric circuit.

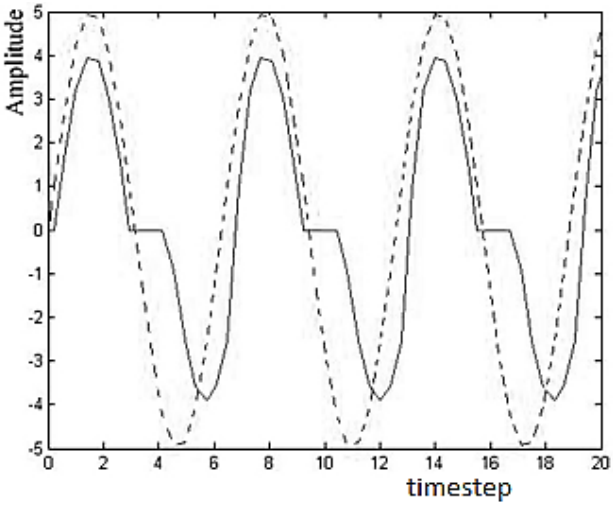

Fig. 7. Output signal (continuous line) vs. input signal (dotted line).

REFERENCES

1. W. Webb, M. Malkan, *ApJ*, 540, 652-67 (2000)
2. S.A. Balbus, J.F. Hawley, *RevModPhys*, 70, 1-53 (1998)
3. T.V. Cawthorne, J.F.C. Wardle, D.H. Roberts, L.F. Brown, *ApJ*, 416, 496 (1993)
4. C.A. Hummel, T.W.B. Muxlow, T.P. Krichbaum, A. Quirrenbach, C.J. Schalinski, A. Witzel, K.J. Johnston, *A&A*, 266, 93-100 (1992)
5. E. Quataert, A. Gruzinov, *ApJ*, 539, 809-814 (2000)
6. S.J. Qian, T.P. Krichbaum, A. WItzel, J.A. Zensus, X.Z. Zhang, *Chin. Astron. Astrophys.*, 6, 530-542 (2006)
7. K.I. Kellerman, I.I.K. Pauliny-TotH, *ApJ*, 155, 71-78 (1969)
8. N.I. Shakura, R.A. Sunyaev, *A&A,* 24, 337-355 (1973)
9. O.M. Blaes, *Euro Summer School - Natoadvaned study institute", eds. V. Beskin and G.Henri and F. Menard nd G. Pelleties and J. Dalibard*, 139 (2002)
10. C. Kunjaya, P. Mahasena, K. Vierdayanti, S. Herlie, *Ap&SS*, 336, 455-460 (2011)
11. A. Koratkar, O. Blaes, *PASP*, 111, 1-30 (1999)